Mathematical Modelling of Fuel Cells for Portable Devices

by

Shawn Edward Litster
B.Eng., University of Victoria, 2004

A Thesis Submitted in Partial Fulfillment of the Requirements for the Degree of

MASTER OF APPLIED SCIENCE

in the Department of Mechanical Engineering

University of Victoria

Supervisor: Dr. N. Djilali

Abstract

More tolerable costs, instant recharges, and increasing energy density demands make fuel cells ideal for supplanting batteries in portable electronic devices. Analytical and semi-analytical models are derived in this thesis to elucidate the transport of ions, heat and mass within two different ambient air-breathing fuel cell architectures. The first architecture is the conventional planar arrangement and the other is a microstructured non-planar architecture. An analytical model of the membrane electrode assembly accurately predicts fuel cell performance through detailed accounting of catalyst layer specifications and electrochemical parameters. A large-scale parametric study resolves the trends associated with a variety of design specifications and operating conditions. The study identifies the substantial effect of heat transfer on membrane dry-out and demonstrates a need to insulate humidity within the fuel cell to enhance performance. An analysis of the non-planar microstructured fuel cell reveals its increased power density and efficiency.

Table of Contents

List of Tables

List of Figures

Nomenclature

Symbol	Description	Units
A	Area	m^2
A_A	Active area	m^2
A_S	Planar surface area	m^2
a	Activity	-
Bi	Biot number	-
C_p	Specific heat of gas	$J\ kg^{-1}\ K^{-1}$
c	Specific heat of solid	$J\ kg^{-1}\ K^{-1}$
c	Concentration	$mol\ m^{-3}$
D	Diffusion coefficient	$m^2\ s^{-1}$
E	Potential	V
F	Faraday's constant	$96485\ C\ mol^{-1}$
ΔG^o	Gibbs energy of formation	$J\ mol^{-1}$
Δg	Specific Gibbs energy change	$J\ mol^{-1}$
g	Gravity	$m\ s^{-2}$
H	Height	m
h	Heat transfer coefficient	$W\ m^{-2}\ K^{-1}$
h_A	Mass transfer coefficient	$kg\ m^{-2}\ s^{-1}$
Δh	Specific enthalpy change	$J\ mol^{-1}$
i	Local current density	$A\ m^{-2}$
i_o^A	Anode exchange current density	$A\ m^{-2}$

$i_o^{Pt/N}$	Interfacial exchange current density	A m^{-2}
j_o	Volumetric exchange current density	A m^{-3}
j_T	Volumetric transfer current density	A m^{-3}
k	Thermal conductivity	W m^{-1} K^{-1}
l	Convection length scale	m
M	Molar mass	kg mol^{-1}
m	Specific mass loading	kg m^{-2}
$\dot{N}$	Mass flux	kg s^{-1}
Nu	Nusselt number	-
n	Number of electrons transferred	-
$\dot{n}$	Specific mass flux	kg m^{-2} s^{-1}
P	Pressure	Pa
q_p	Flux of heat produced	W m^{-2} K^{-1}
q_t	Flux of heat transferred	W m^{-2} K^{-1}
R	Universal gas constant	8.3145 J mol^{-1} K^{-1}
Ra	Rayleigh number	-
S	Source term	kg m^{-2} s^{-1}
S_{Pt}	Specific platinum surface area	m^2 kg^{-1}
Δs	Entropy change	J mol^{-1} K^{-1}
T	Temperature	K
V	Volume	m^3
W	Width	m
x	Horizontal position	m
x	Species mole fraction	-

y	Species mass fraction	-
y_N	Nafion content	-
y_{Pt}	Platinum/Carbon ratio	-
z	Vertical position	m

Greek symbols

α	Transfer coefficient	-
β	Symmetry factor	-
β	Thermal expansion coefficient	K^{-1}
δ	Heat transfer length scale	m
ε	Porosity	-
ε_r	Emissivity	-
γ	Concentration exponent	-
ϕ	Electrolyte phase potential	V
η	Overpotential	V
λ	Water content	$H_2O\ (SO_3^-)^{-1}$
μ	Viscosity	$kg\ m^{-1}\ s^{-1}$
ρ	Density	$kg\ m^{-3}$
σ	Conductivity	$S\ m^{-1}$
σ_r	Stefan-Boltzmann constant	$5.67\times10^{-8}\ W\ K^{-4}\ m^{-2}$
τ	Tortuosity factor	-
υ_{Pt}	Platinum utilization	-

Superscripts

A	Anode
Amb	Ambient
C	Cathode
CL	Catalyst layer
GDL / CL	GDL and catalyst layer interface
eff	Effective value
Pt / N	Platinum and Nafion interface
ref	Reference value

Subscripts

A	Anode
a	Anodic
air	Air
$Bulk$	Bulk quantity
C	Cathode
C	Carbon
CL	Catalyst lyaer
c	Cathodic
$cell$	Fuel cell
eff	Effective value
f	Fuel
GDL	Gas diffusion layer
$H2$	Hydrogen

H2O	Water
Mem	Membrane
N	Nafion
O2	Oxygen
OC	Open circuit
Pt	Platinum
r	Reversible
ref	Reference value
sat	Saturation
T	Transfer

Acknowledgments

First, I would like to thank my supervisor, Dr. Ned Djilali, who has provided me with insightful guidance and generous support over the past four years. I am grateful for his early recognition of my appetite for engineering research. I truly appreciate his confidence in my work; it inspires me to always try harder.

I would also like to thank Dr. Ged McLean and Angstrom Power Inc. The fuel cell technology they are developing provided the motivation for this work. The constructive feedback I received during my visits to Angstrom outlined my objectives for this thesis.

I am very appreciative of the help I received from my officemate, Dr. Jay Sui. I am also indebted to Susan Walton of IESVic for simply making everything work. In addition, I would like to thank the Computational Fuel Cell Engineering group at IESVic for creating a supportive environment in which to work.

I am forever grateful to my glorious fiancée, Kristin McLennan. Kris spent endless hours toiling over my fragmented grammar and was instrumental in ensuring that my life outside of the masters did not fall to pieces. I also need to thank my parents and my grandmother for their support while preparing this thesis.

Funding for this research was provided by the Natural Sciences and Engineering Research Council of Canada (NSERC) in the form of a Canada Graduate Scholarship. The Canadian Space Agency also supported this research with a NSERC supplement.

Chapter 1

Introduction

1.1 Background

Fuel cells are increasingly viewed as a future power source in many applications. Advantages include the potential to run continuously at high efficiencies and to operate pollution free. Proton-exchange-membrane (PEM) fuel cells are being developed for portable, residential, and mobile applications; they are predominantly being developed for cars and buses. Techno-economic analyses have shown, however, that portable consumer electronics present a more accessible market for fuel cells in the immediate future because of the higher cost per unit of energy acceptable at these smaller scales [1, 2]. For example, Dyer [1] stated that the cost tolerance for fuel cells in portable equipment is two orders of magnitude greater than that for automotive applications. Another key advantage of fuel cells for portable applications over batteries is longer continuous operation with almost instantaneous refueling.

An increasingly more prevalent driver of fuel cell development for portable devices is the continual development of consumer electronics with increasing energy density requirements. As recently discussed by Kariatsumari and Yomogita in a cover story for the February 2005 issue of *Nikkei Electronics Asia* [2], the development of mobile phones with digital broadcast reception will spur the integration of fuel cells into mobile phones. The authors report that even if the capacity of Li-ion batteries grows at 10% per year, they will still not be capable of powering future devices at their present volume. Thus, Kariatsumari and Yomogita predicted that the integration of fuel cells into next-generation mobile phones will be the next battery revolution. This forthcoming battery revolution will be similar in process to the previous one. In the last revolution of batteries, the development of power eating camcorders and notebook PCs spawned the wide-spread adoption of Li-ion batteries when Ni-Cd2 and NiMH batteries could no longer meet the energy density demands. In a similar fashion, fuel cells could supplant Li-ion batteries. Figure 1.1 illustrates the evolution of these battery revolutions as presented by Kariatsumari and Yomogita.

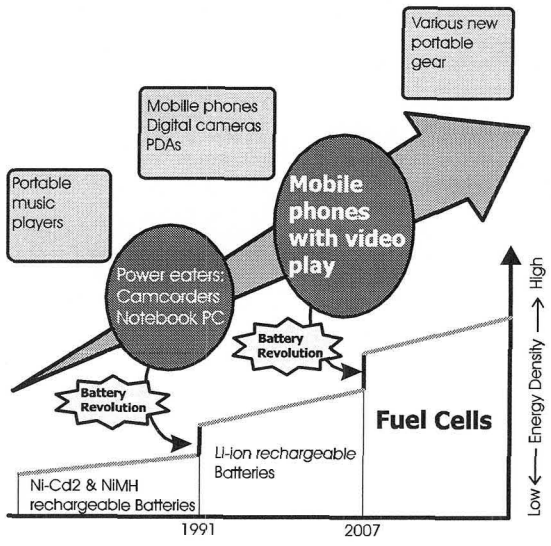

Figure 1.1: Evolution of the energy density demands of portable devices. Adapted from [2].

1.2 Device integrated fuel cells

1.2.1 Polymer electrolyte membrane fuel cells

Among the various forms of fuel cells, the polymer electrolyte membrane fuel cell (PEMFC) is a top candidate for the future power source of portable devices. A PEMFC is an electrochemical cell that is fed hydrogen, which is oxidized at the anode, and oxygen that is reduced at the cathode and reacts with the hydrogen to produce water. The overall reactions at the anode and cathode and the overall reaction for the fuel cell are:

$$\begin{aligned} &\text{Anode:} && H_2 \rightarrow 2H^+ + 2e^- \\ &\text{Cathode:} && \frac{1}{2}O_2 + 2H^+ + 2e^- \rightarrow H_2O \\ &\text{Overall:} && H_2 + \frac{1}{2}O_2 \rightarrow H_2O \end{aligned} \tag{1.1}$$

The protons released during the oxidation of hydrogen are conducted through the proton exchange membrane (PEM) to the cathode. Since the membrane is not electronically conductive, the electrons released from the hydrogen gas travel along the electrical detour provided and electrical current is generated. These pathways are shown schematically in Figure 1.2.

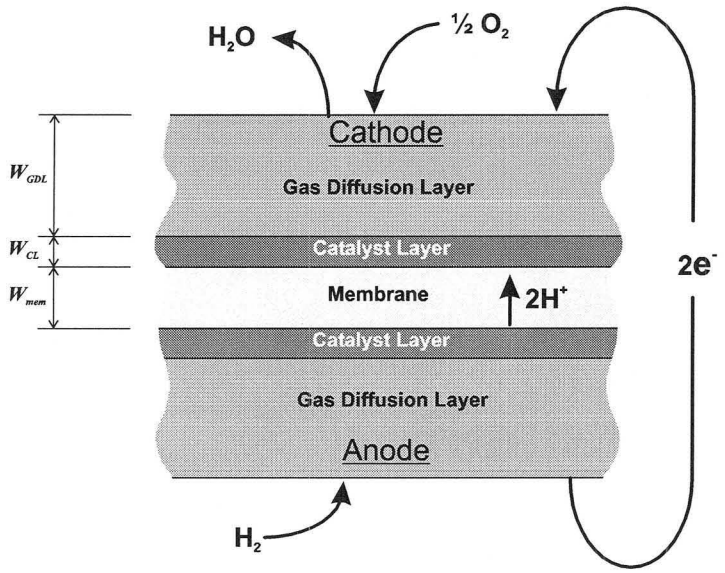

Figure 1.2: Schematic of the membrane electrode assembly for PEM fuel cells.

At the heart of the PEMFC is the membrane electrode assembly (MEA). As shown in Figure 1.2, the MEA consists of a proton exchange membrane, catalyst layers, and gas diffusion layers (GDL). The MEA is typically sandwiched by two flow field

plates that are mirrored to make bipolar plates for stacking cells in series to achieve greater voltages.

PEMFC electrodes feature two regions of porous media: the gas diffusion layer and the comparatively more dense catalyst layer. The thin catalyst layers are where the reaction occurs and the thicker gas diffusion layer acts as a conduit for electrical current that is also permeable to reactant and product fluids. The catalyst layer features significantly lower void space and smaller pores because of the small catalyst particles and the impregnation of proton conducting ionomer (typically Nafion). Presently, most catalyst layers are fabricated with the thin-film method, which consists of applying an ink containing Nafion and carbon-supported catalyst to either the membrane or the gas diffusion layer [3]. This approach yields a 10 to 20 μm thick porous layer that is ionically and electrically conductive.

1.2.2 Device integration

The envisaged implementation of PEM fuel cells for portable devices is in a device integrated form. This implementation entails the fuel cell being placed either on, or within portable electronics. For example, fuel cells could be placed on the exterior surfaces of mobile phones and notebook PCs. The fuel cell could also be fixed to a device's main circuit board. Figure 1.3 presents a schematic of the proposed integration of a fuel cell into a mobile phone. The cathode gas diffusion layer is open to the ambient air and the fuel is stored and distributed below the fuel cell. The advantage of having the cathode open to the air is that it eliminates the need for manifolding that supports the transport of reactant and product gases. In addition, the open surface aids in the removal of heat from the fuel cell.

Figure 1.3: Illustration of an ambient air-breathing fuel cell as a power source for a mobile phone with video playback.

As illustrated in Figure 1.3 and stated by Kariatsumari and Yomogita [2], the volume available to the fuel cell on next-generation mobile phones would be approximately 45 mm × 35 mm × 4 mm after considering the volume occupied by necessary ancillary devices and assuming an external fuel cartridge is used. This volume also accounts for the presence of film-type Li-ion batteries. This allowance was made because fuel cells will have difficulty responding to the large load fluctuations of these devices. Kariatsumari and Yomogita assumed the power requirement put on the fuel cell by these mobile phones to be roughly 1 W. Based on the predicted planar area available on the mobile phone, the power density requirement of the fuel cell is then 60 mW cm^{-2}

One of the foremost design objectives when designing components for portable electronics is the reduction of volume. This requires an increase in the power density of the cell through miniaturization. In addition, the size and number of ancillary

components required for operation must be reduced. The fuel cell designs presented in this study address a number of the fuel cell system components in order to reduce the total volume. The issues addressed include the supply of oxygen and hydrogen, heat management, and miniaturization of the fuel cell.

1.2.3 Oxygen supply

In the envisaged device integrated fuel cells, the ambient air above the surface of the fuel cell provides the oxygen required for the reaction at the cathode. The mode of oxygen transport is a combination of advection and diffusion. Oxygen is advected to regions near the cathode GDL by local air currents, including the natural convection currents induced by the elevated temperature of the fuel cell's exterior surfaces. Diffusion is the dominant mode of mass transport at short distances from the surface of the cathode GDL, where the oxygen diffuses through the viscous boundary layer and into the porous gas diffusion layer.

Although this is not the most common method of delivering oxygen to the cathode, it has been shown experimentally and theoretically that fuel cells can operate effectively in a passive air-breathing mode [4-14]. Nevertheless, passive air-breathing cells featuring planar architecture are limited to single-stack configurations because of the requirement of an unobstructed cathode surface. In some cases, a 'side-by-side' series connection of individual fuel cells has been adopted to achieve greater voltages [5, 15]. In addition, the literature suggests that passive air-breathing fuel cells become mass transfer limited at current densities between 0.15-0.35 mA cm^{-2} [5, 7, 13], well below the current densities found in full-scale PEMFC systems.

These studies suggest that this limitation is a result of the atmospheric pressure of the oxidant being 1 atm (instead of the 3-5 atm) and the reduction in convective capacity.

1.2.4 Hydrogen supply

The hydrogen delivery system can also be targeted to reduce the overall volume of a device integrated fuel cell system. One approach is the removal of the manifolding for recycling excess hydrogen. The recycling of unused hydrogen is typical of most fuel cell systems since they generally operate at a hydrogen stoichiometry greater than one in consideration of the mass transfer and water management issues found in large systems. The need for this manifolding can be eliminated in device integrated fuel cells by introducing a "dead-ended" hydrogen supply. The "dead-ended" arrangement for hydrogen supply is realizable by maintaining relatively constant hydrogen pressure at the anode's GDL interface. Constant hydrogen pressure can be achieved in an array of approaches. One method is to have a high-pressure hydrogen supply which is introduced to the fuel cell via a pressure-regulating valve, or a displacement approach in which the storage volume is reduced as the fuel is consumed in order to maintain constant gas pressure.

Another way to reduce the volume requirements of the hydrogen supply is to eliminate components that condition the hydrogen prior to entering fuel cell stacks. Generally, conditioning is a combination of heating and humidification. Conditioning raises the temperature of the gas stream slightly above the fuel cell's operating temperature and saturates the hydrogen with water vapor. This conditioning improves performance by maintaining the humidification of the membrane on the anode side of the MEA. However, the system required for conditioning is likely to be eliminated for

device integrated fuel cells to save volume and the hydrogen supply will likely be dry (zero humidity).

1.2.5 Heat management

Heat management (the attempt to maintain an optimum temperature in the fuel cell) in most full-size PEM fuel cells is actively conducted by pumping a liquid coolant through dedicated channels within the fuel cell stack. For device integrated fuel cells, a method of passively managing the heat is sought. For small systems operating at low-current densities with low heat output, the excess heat can be removed by the surrounding air through convective heat transfer that includes natural convection. Given that the temperature and humidity of ambient air is relatively constant, the operating temperature of the fuel cell can have a significant effect on electrolyte conductivity because it is strongly dependent on humidification.

1.2.6 Micro fuel cells

In order for a fuel cell to be viable in portable devices, current PEM fuel cells must undergo significant miniaturization. The adaptation of conventional fuel cell designs for smaller applications is restricted by the macro-scale materials and manufacturing processes they utilize. Exploitation of microscale transport processes in conjunction with micro-manufacturing processes, such as those applied in the production of integrated-circuits, make it possible to conceive extremely high power density fuel cells [16]. Such fuel cells have the potential to be significantly cheaper, smaller, and lighter than planar plate and frame fuel cells.

The implementation of thin layer manufacturing processes can reduce stack size and conductive path length; enhancing the volumetric power density. Micro-fabrication of flow fields, current collectors, and electrical interconnects has been reported in the literature [5, 13, 15]. In general, however, these fuel cell designs have relied on traditional planar MEA architecture.

Because the majority of PEM fuel cell designs are based on planar plate and frame architecture, the volumetric power density in such designs is inherently constrained by the two-dimensional active area. Non-planar designs can achieve much higher active area to volume ratios, and hence greater volumetric power density; this feature was demonstrated in the waved cell topology proposed by Mérida *et al.* [17]. The non-planar fuel cell devised by Mérida *et al.* [17] featured a waved membrane-electrode assembly supported by an expanded metallic mesh structure. In this design, the MEA played an additional function by forming the channels that distribute the fuel and oxidant. Thus, the volume that previously comprised the flow channels could support additional active area and generate increased volumetric power density. In practice, however, the pitch of the MEA undulations is limited by conventional fabrication techniques.

1.3 Fuel cell modelling

Fuel cell researchers are increasingly turning to fuel cell models to improve the fundamental understanding of the transport phenomena present in PEM fuel cells and to use these models for design optimization. The majority of the phenomena take

place in regions of the fuel cell that are in general inaccessible to experimental measurement. Therefore, a mathematical model is vital in developing a better understanding. The need for a physics-based model is compounded when considering device integrated fuel cells. As these forms of PEM fuel cells are emerging, the design process can be streamlined by the insight provided by a well-developed model.

The literature reviewed in this section include studies of PEM fuel cells employing analytical, semi-analytical, and other novel solutions [18-27]. These models contrast those employing advanced numerical methods such as computational fluid dynamics [28-34]. Analytical models typically require significant assumptions in order to arrive at tractable solutions. However, an analytical expression can provide ample insight through the mathematical forms of the solutions. Large parametric studies must be conducted with numerical models to obtain this degree of insight. Also, the complexity of the advanced numerical methods dramatically increases the required computational resources. The necessity for large amounts of computational resources is a significant factor in the present inability to use CFD to accurately model entire fuel cell stacks. Thus, the majority of CFD models of PEM fuel cells consider only a single straight channel or a lone serpentine. Some of the models reviewed herein are combinations of analytical and numerical methods that are computationally more economical than a full numerical model. This methodology may prove useful in expanding a hybrid CFD/analytical approach to the modelling of entire fuel cell stacks.

Springer *et al.* [18] presented one of the earliest semi-analytical solutions to a one-dimensional cross-section of a PEM fuel cell. Their model considered mass continuity

through the flow channels, gas diffusion in the GDL, water transport through the membrane (back diffusion and electro-osmotic drag), and proton conduction in the membrane. In addition, they determined the cathode overpotential by modelling the cathode catalyst layer as an interface that obeys Tafel kinetics. Their solution was obtained iteratively by employing numerical integration of the governing equations.

Bernardi and Verbrugge [19] presented a one-dimensional model of a PEM fuel cell. In their work, the governing equations were solved numerically. Due to the implementation of a numerical method, Bernardi and Verbrugge were able to couple a greater set of phenomena than Springer *et al.* These additional features include modelling the pressure driven flow of water, distinguishing vapor from liquid water, accounting for the anodic reaction, and solving electric conduction. Also, Bernardi and Verbrugge implemented the full Butler-Volmer equation to model the electrochemistry and Schlögl's equation for the membrane transport.

Fuller and Newman [20] produced one of the earliest along-channel models in which a solution is found for the model variables through the cross-section of the MEA at discrete locations along the path of the flow channel. This solution was obtained numerically and the properties along the channel were determined with an integral approach. This gave Fuller and Newman the ability to present variations along the length of the gas channel. The model also examined heat and water management. The membrane transport was resolved with concentrated solution theory.

Nguyen and White [21] developed a two-dimensional along-channel model of a fuel cell employing a semi-analytical solution procedure. Their model included the effect

of heat transfer within PEM fuel cells by prescribing a cell temperature and computing the heat transfer into the gas channels. In addition, heat generation within the cell was considered to be only a product of the latent heat of water phase change. These simplifications were addressed in a later work [23]. This model neglected mass transfer in the gas diffusion layer by considering it "ultrathin." Nguyen and White also only modelled the cathode catalyst layer, neglecting the anode. The cathode catalyst layer was approximated by considering the layer as an interface obeying Tafel kinetics. These simplifications allowed their group to refrain from employing numerical methods such as finite difference approximations. The solution strategy was to prescribe an average current density and use Newton's method to reveal the corresponding cell voltage.

Gurau *et al.* [24] fashioned an analytical model of a half-cell (neglecting the anode side) considering a cathode catalyst layer of a finite-thickness. They assumed constant overpotential through the cathode catalyst layer in order to achieve a solution of the electrolyte phase potential and the oxygen distribution. This is a significant simplification because it overestimates the potential change by decoupling the Tafel equation from the electrolyte phase solution. A novel aspect of this model was the sub-sectioning of the GDL into regions of different properties to represent liquid water accumulation. However, Gurau *et al.* neglected water transport through the membrane.

Bradean *et al.* [25] employed a novel method of reducing the computational effort required to achieve a pseudo three-dimensional solution by implementing a hybrid numerical model of a PEM fuel cell at discrete locations along a flow channel. A two-

dimensional cross-section of the fuel cell, perpendicular to the flow channel, was resolved with the finite difference method. The membrane and anode were not considered and the catalyst layer was modelled as a boundary condition with fluxes determined from a first-order reaction expression (i.e.; the reaction was dependent only on the local concentration of oxygen). Along the channel, the group used interpolated channel properties extracted from measured experimental quantities at the inlet and outlet of a PEM fuel cell.

Berg *et al.* [26] presented a (1+1)-dimensional model of a PEM fuel cell. In the (1+1) model, a solution of a two-dimensional cross-section parallel to the gas channel was achieved by solving a one-dimensional slice through the membrane at discrete locations along the gas channel. This approach is similar to the method employed by Nguyen and White [21]. Berg *et al.* solved the one-dimensional slice analytically by modelling the GDL with a mass transfer coefficient that correlated the channel concentration to that in the catalyst layer. The one-dimensional solution of the membrane was evaluated along the gas channel, providing coupling by solving the transport in the gas channel with an integral approach. Berg *et al.* model treated the cathode catalyst layer as an interface with the Tafel equation. This work neglected the overpotential in the anode catalyst layer.

Kulikovsky [27] also developed a (1+1)-dimensional semi-analytical model of a PEM fuel cell. In comparison to Berg *et al.*, who employ a mass transfer coefficient, this model resolved the mass transport in the gas diffusion layer. In addition, the total water flux through the membrane was set to zero by assuming that the electro-osmotic drag was perfectly balanced by diffusion from cathode to anode. The

overpotential in the cathode catalyst layer was considered constant along the thickness of the layer.

1.4 Objectives

Fuel cells for portable devices present new design objectives and constraints. The present work attempts to refine design objectives and identify constraints with a theoretical model using both analytical and semi-analytical approaches. Chapter 2 presents the derivation and validation of the analytical MEA model used throughout the following analysis. The analytical MEA model is subsequently applied to two distinct fuel cell architectures to explore the merits of each architecture for integration into portable devices. The first architecture, studied in Chapter 3, is the planar design commonly presented in the literature [5, 7, 12-14]. The second architecture is the patented non-planar microstructured architecture [10, 35-37] that Angstrom Power Inc. is currently developing. This non-planar architecture is investigated in Chapter 4.

The derivation of the MEA model in Chapter 2 is directed by the objective of optimizing micro-fuel cells that passively breathe ambient air [4, 6, 7, 14, 38, 39]. This mode of operation is likely to result in low-humidity conditions and lower current densities. Thus, the ohmic losses in the electrolyte have greater relative importance than mass transfer limitations. Due to these significant ohmic losses, the MEA model's derivation focuses on the ion transport rather than mass transport. Unlike a majority of analytical fuel cell models, the derivation resolves the ion transport through the cathode catalyst layer. Previous non-computational models have

typically treated the catalyst layer as an interface [18-21, 26]. A macrohomogeneous model is employed to correlate the catalyst layer's specifications to its microstructure, which is represented with volumetric properties [40]. A significant effort to avoid polarization curve fitting procedures is made by employing experimental characterizations of various catalyst layer properties. The detailed catalyst layer model enables the optimization of catalyst layers for micro-fuel cells. Another important feature of the model is the use of a membrane conductivity correlation with improved accuracy under low-humidity conditions.

Finally, there is a significant focus on the heat transfer between the fuel cell and the surrounding environment. The analysis considers both convective and radiative heat transfer from the fuel cell to the environment using a lumped-body formulation that is permissible due to the low Biot number of the proposed micro-fuel cells. The rate of heat transfer will be shown to be crucial when trying to maximize the performance of device integrated fuel cells.

Chapter 2

Analytical MEA model

2.1 Introduction

The following is a presentation of a one-dimensional model of the membrane electrode assembly in a PEM fuel cell. The derivation of the model facilitates the optimization of micro-fuel cells that passively breathe ambient air. This mode of operation is likely to result in low-humidity conditions and lower current densities. Thus, the ohmic losses in the electrolyte have greater relative importance than the mass transfer limitations, which is attributable to reduced electrolyte conductivity at low relative humidity. Because of the significant ohmic losses present in low humidity operation, the derivation focuses on the ion transport rather than mass transport.

2.2 Model

Analytical expressions are utilized for this model to avoid a discretized numerical implementation. The model domain includes both the cathode and anode catalyst layers and the membrane. Figure 2.1 presents a schematic of the model domain and the corresponding sub-models.

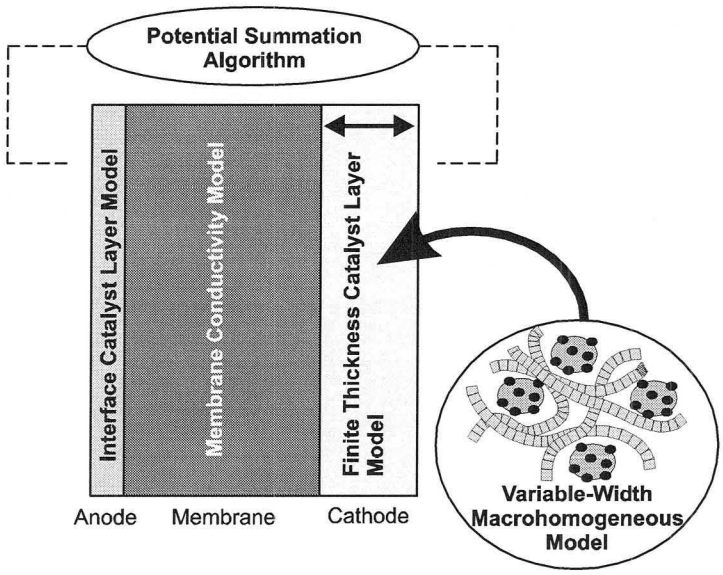

Figure 2.1: Schematic of the one-dimensional analytical MEA model.

As shown in Figure 2.1, the MEA model consists of five main components. The potential summation algorithm calculates the distribution of losses through the MEA. Individual potential losses in the cathode, anode, and membrane are calculated using a finite-thickness catalyst layer model, an interface catalyst layer model, and a linear membrane model with uniform conductivity, respectively. The finite-thickness model is implemented with parameters evaluated from a macrohomogeneous catalyst layer model. The macrohomogeneous catalyst layer model correlates the required volume average quantities with the microstructure of the catalyst layer. A novel feature of this

particular macrohomogeneous model is the variable catalyst layer width, which is determined from the catalyst layer specifications. Each of these sub-models will be presented in detail.

2.2.1 Potential summation algorithm

Unlike initial modelling efforts that used current density as the operating parameter [10, 41], the potential summation algorithm is similar to the voltage-to-current methods employed by Nguyen *et al.* [30] and Sivertsen and Djilali [32]. The algorithm originates from the allocation of the total potential loss from the open-circuit voltage ($E_{OC} - E_{cell}$). The potential drop is distributed between activation overpotentials in the cathode and anode (η^C, η^A) and the potential drop through the membrane. The potential drop through the electrical pathways is neglected due to its minimal contribution to the overall potential drop. The catalyst layer overpotentials are determined with models described in subsequent sections. The potential drop of the membrane is the product of the membrane resistance and current (i). The resistance is determined from the membrane width (W_{Mem}) and the protonic conductivity of the electrolyte (σ_{Mem}).

Considering the current to be a result of the overpotential in the cathode catalyst layer ($i_C(\eta^C)$), the following expression for the potential summation through the MEA is obtained:

$$(E_{OC} - E_{cell}) - \eta^C - \eta^A - \frac{W_{Mem}}{\sigma_{Mem}} i_C(\eta^C) = 0 \tag{2.1}$$

which is constrained by the relationship:

$$i_C(\eta^C) - i_A(\eta^A) = 0 \tag{2.2}$$

The theoretical open-circuit voltage (E_{OC}) in Eqn. (2.1) is calculated with the Nernst equation. The standard potential (E^o) is determined from the Gibbs energy of formation (ΔG^o):

$$E^o = -\Delta G^o / nF \tag{2.3}$$

where n is the electrons transferred per mole of product ($n = 2$) and F is Faraday's constant. The dependence of ΔG^o on the temperature was presented by Parthasarathy *et al.* [42] as:

$$\Delta G^o = -295800 - 33.5T \ln T + 388.7T \qquad [\text{J mol}^{-1}] \tag{2.4}$$

To represent the influence of reactant concentrations on the theoretical open-circuit potential, the Nernst relationship is employed. The activities of oxygen and hydrogen (a_{O2} and a_{H2}) are included in this expression:

$$E_{OC} = E^{o} + \frac{RT}{nF}\left(\ln(a_{H2}) + \frac{1}{2}\ln(a_{O2})\right) \tag{2.5}$$

2.2.2 Finite-thickness catalyst layer model

The cathode catalyst layer is distinguished from the anode by its lower activity, which results in a slower oxygen reduction reaction (ORR). The ORR is the rate limiting reaction and takes place in a more distributed manner within the catalyst layer. The impact of a distributed reaction rate within a catalyst is that the potential loss due to protonic conduction becomes significant. Due to a much higher electrical conductivity, the electronic potential can be assumed to be uniform [43].

In the derivation of a finite-thickness catalyst layer model, the influence of oxygen diffusion is neglected. This is acceptable when considering conditions where ohmic losses are the dominant influence. Eikerling and Kornyshev [44] presented an expression of the Tafel slope ($RT/\alpha F$), ionic conductivity (σ), and a diffusion parameter (Θ) that determines when these conditions exist:

$$g = \frac{\alpha F}{RT}\frac{\Theta}{\sigma} \tag{2.6}$$

where:

$$\Theta = \frac{4FP_{air}D_{O2}^{CL}}{RTW_{CL}} \tag{2.7}$$

in which D_{O2}^{CL} is the oxygen diffusivity in the catalyst layer and W_{CL} is the thickness of the catalyst layer. When $g \gg 1$, oxygen transport is rapid in comparison to proton conduction. With the values to be considered in subsequent analysis, the assumption of rapid oxygen transport is valid.

The present approach is similar to that of Eikerling and Kornyshev [44] when they considered rapid oxygen transport. However, their analysis focused solely on the catalyst layer. The present finite model is also similar to that derived by Gurau *et al.* [24] for their analytical half-cell model of a PEM fuel cell. However, the assumptions are reversed. Gurau *et al.* assumed a uniform overpotential within the catalyst layer to solve oxygen distribution and the membrane potential based on the resulting current density profile in the layer. Here, the overpotential is calculated as part of the solution and an important new feature of the present model is the coupling of the overpotential and electrolyte phase potential. The distribution of overpotential and ionic current within the cathode catalyst layer is resolved analytically. The governing equation for proton conduction is Ohm's law, which can be expressed as:

$$i = \sigma \frac{d\phi}{dx} \tag{2.8}$$

where ϕ is the potential. Cast in a conservative form with a source term for the current generation (j_T) the equation becomes:

$$\sigma \nabla^2 \phi = j_T \tag{2.9}$$

The rate of the ORR is considered locally dependent on the overpotential (the difference between the potential of electrolyte and that of the electric potential in the platinum $\eta = \phi - \phi_s$). It is assumed that the rate of reaction can be determined with the Tafel equation (Eqn. (2.10)). This is valid for high overpotentials ($\eta >> RT/\alpha F$) and was introduced for PEMFC modelling by Perry *et al.* [45] and is used by many others.

$$j_T = j_o \left(\frac{\bar{c}_{O2}}{c_{O2}^{ref}} \right)^{\gamma} \exp\left(\frac{\alpha F}{RT} \eta \right) \tag{2.10}$$

The volumetric form of the exchange current density j_o can be determined from experiment or theory. In addition, the exchange current density is affected by the average oxygen concentration through the thickness of the layer ($\bar{c}_{O2}$). The concentration dependence exponent (γ) specifies the sensitivity of the exchange current density to reactant concentration. The influences of the water vapour and hydrogen ion activities on the exchange current density are neglected.

Eqns. (2.8)-(2.10) can be solved analytically in an implicit fashion with the expression:

$$\eta(x)=\frac{1}{b}\ln\left\{\tan^2\left[\sqrt{\frac{bA\exp(b\eta_o)}{2}}(x-W_{CL})+\arctan\left(\frac{\sqrt{\exp(b\eta_1)-\exp(b\eta_o)}}{\sqrt{\exp(b\eta_o)}}\right)\right]+1\right\}+\eta_o \tag{2.11}$$

where:

$$A=\frac{j_o}{\sigma}\left(\frac{\bar{c}_{O2}}{c_{O2}^{ref}}\right)^{\gamma} \quad \& \quad b=\frac{\alpha F}{RT}$$

and where x is the location in the layer, W_{CL} is the thickness of the layer, and η_o and η_1 are the overpotentials at the GDL and membrane interfaces, respectively. η_1 corresponds to η^C in Eqn. (2.1). Eqn. (2.11) is similar, but not identical, to the expression obtained by Eikerling and Kornyshev [44]. The protonic current into the cathode at the membrane interface is obtained from the derivative of overpotential multiplied by the conductivity:

$$i=\sigma\sqrt{\frac{2A}{b}}\sqrt{\exp(b\eta_1)-\exp(b\eta_o)} \tag{2.12}$$

2.2.3 Macrohomogeneous catalyst layer model

A macrohomogeneous catalyst layer model is utilized to study of the effect of catalyst layer composition. As noted by Eikerling and Kornyshev [44], the macrohomogeneous model has been around for decades. However, variations in derivation and implementation continue to emerge [24, 40, 44, 46].

The macrohomogeneous model is distinguished by the representation of the catalyst layer microstructure as a homogeneous medium with properties reflecting the catalyst layer microstructure. This entails the determination of each material's volume fraction (platinum, carbon, Nafion, gas) and the structural properties (tortuosity, interfacial areas). This information enables the calculation of transport properties (effective ionic conductivity and gas diffusivity) and electrochemical parameters (volumetric exchange current density).

2.2.3.1 Catalyst layer composition

The volume of the catalyst layer is divided into four components: platinum, Nafion, carbon, and void space. By employing the standard catalyst layer specifications and a known catalyst layer width, each volume fraction can be determined [40]. The typical specifications, ranges, and units are [3]:

1. Platinum loading, m_{Pt} (0.05 – 5 mgPt cm^{-2}).

2. Platinum/carbon ratio, y_{Pt} (20 – 40% Pt/C).

3. Nafion content, y_N (20 – 60 % wt.).

The volume fraction of platinum is simply the loading divided by platinum's density (ρ_{Pt}) and the catalyst layer width (W_{CL}):

$$\varepsilon_{Pt} = m_{Pt} \frac{1}{\rho_{Pt} W_{CL}} \tag{2.13}$$

The volume fraction occupied by carbon is determined by calculating the carbon loading (m_C) from the platinum loading and the platinum/ carbon ratio:

$$\varepsilon_C = m_C \frac{1}{\rho_C W_{CL}} = \frac{m_{Pt}(1-y_{Pt})}{y_{Pt}} \frac{1}{\rho_C W_{CL}} \tag{2.14}$$

As shown below in Eqn. (2.15), the volume fraction of Nafion is evaluated from the area loading of the Nafion (m_N) divided by the Nafion density (ρ_N) and the width of the catalyst layer. The loading of the Nafion is determined from three commonly presented catalyst layer properties: Nafion content (weight percentage of the catalyst layer that is Nafion), platinum loading, and platinum/carbon ratio:

$$\varepsilon_N = m_N \frac{1}{\rho_N W_{CL}} = \frac{y_N m_{Pt}}{y_{Pt}(1-y_N)} \frac{1}{\rho_N W_{CL}} \tag{2.15}$$

Subsequently, the void fraction (ε_V) can be calculated from the constraint of the volume fractions summing to unity:

$$\varepsilon_V = 1 - (\varepsilon_{Pt} + \varepsilon_C + \varepsilon_N) \tag{2.16}$$

2.2.3.2 Variable-width implementation

Previous studies using similar relations for catalyst layer composition during optimization [40, 47, 48] have typically considered the void fraction to vary with catalyst layer specifications and the catalyst layer width to remain constant regardless of specifications. The case will be made herein that the width should be a function of the catalyst layer specifications and that the void fraction should remain constant.

The argument for constant void fraction arises from the consistently high ratio of solvent to Nafion and carbon supported catalyst in the ink used to prepare the catalyst layer [3]. It is hypothesized that the volume fraction of solvent in the catalyst layer prior to the evaporation step in the MEA fabrication is consistent over a range of catalyst layer specifications. This is a result of the high proportion of solvent in the applied catalyst ink. Subsequent to the evaporation process, the consistent solvent distribution will present a consistent void fraction in the catalyst layer.

Figure 2.2 presents a schematic of the effect of changing two different catalyst layer specifications (Nafion content and platinum loading). From the present hypothesis of constant void fraction it can be shown that increasing the Nafion content increases the width of the catalyst. In addition, for constant platinum loading, an increase in Nafion content increases the mean distance between catalyst particles. This can be both beneficial and detrimental.

Increased Nafion content, resulting in a higher Nafion volume fraction, improves the ability of ions to reach the catalyst sites. However, the increased width also lengthens the transport length scales; the longer length scale hinders ion conduction and reactant transport. Thus, although the oxygen transport to the cathode catalyst sites is not

restricted by lower porosity with greater Nafion content, it is restricted by the greater thickness through which it must diffuse. The present hypothesis is supported by established experimental results of greater mass transport limitations with higher Nafion contents [3].

In contrast to the effect of increasing Nafion content, when the platinum loading is increased there is no change in volume fractions. The only change is the thickness of the layer. Thus, the benefit of increasing the platinum content, namely the increased total electrochemically active area, is countered by increased diffusion and conduction lengths.

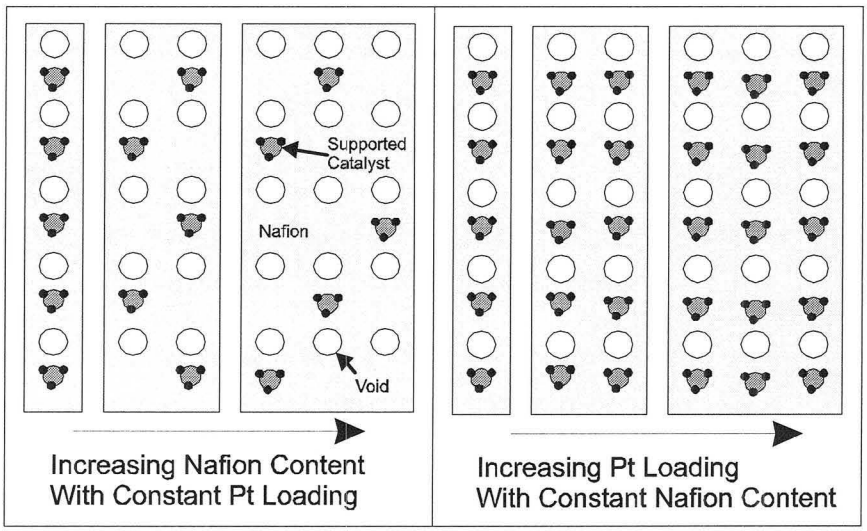

Figure 2.2: Schematic of the influence of changing Nafion content or platinum loading has on the microstructure and width of the catalyst layer.

The width of the catalyst layer is determined by solving the previous set of volume fraction equations (Eqns. (2.13)-(2.16)) for a constant void fraction. The resulting expression for the catalyst layer width is presented in Eqn. (2.17). From this equation,

Figure 2.3 depicts the influence of platinum loading and Nafion content on the catalyst layer width when the void fraction is 55%.

$$W_{CL} = \frac{1}{1-\varepsilon_v}\left(m_{Pt}\frac{1}{\rho_{Pt}} + \frac{m_{Pt}(1-y_{Pt})}{y_{Pt}}\frac{1}{\rho_C} + \frac{y_N m_{Pt}}{y_{Pt}(1-y_N)}\frac{1}{\rho_N} \right) \tag{2.17}$$

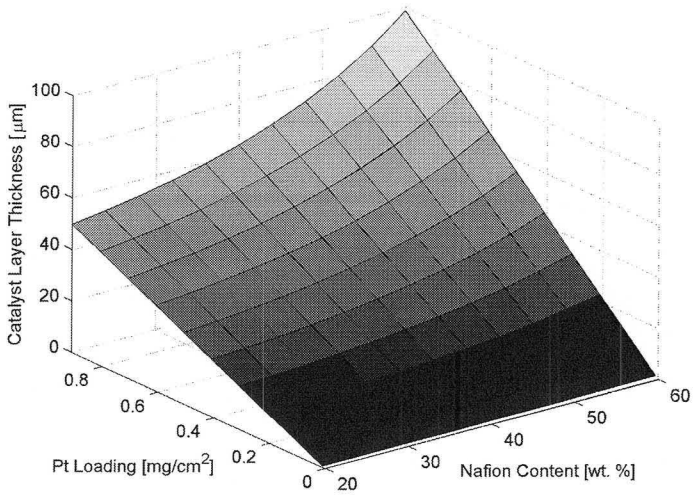

Figure 2.3: Catalyst layer width as a function of platinum loading and Nafion content. $y_{Pt} = 20\%$ and $\varepsilon_V = 55\%$.

The volume fraction of Nafion in the catalyst layer is subsequently used to calculate the layer's effective ionic conductivity. The bulk ionic conductivity is determined from the humidity and temperature in the layer. The effective conductivity is calculated with the Bruggemann correction, which employs the Nafion volume fraction (ε_N) with a Bruggemann exponent of 1.5. This particular Bruggemann exponent was obtained from a study on the electrical conductivity of dispersions [49].

This correction, which is formulated in Eqn. (2.18), is suitable here because of the disperse catalyst agglomerates in the layer. It has been employed in this fashion by many researchers [24, 47, 48, 50].

$$\sigma = \varepsilon_N^{1.5} \sigma_{Bulk} \tag{2.18}$$

2.2.3.3 Volumetric exchange current density

When solving the Tafel equation in the finite-thickness model, the main electrochemical parameter is the volumetric exchange current density (j_o). As shown in Eqn. (2.19), the volumetric exchange current density is the product of three factors. The main contributor to this property is the exchange current density of the platinum/Nafion interface ($i_o^{Pt/N}$). The second term is the area of platinum/Nafion interface per unit volume (A_{Pt}). The third contributor is the platinum utilization (υ_{Pt}), which is the percentage of the area that is electrochemically active.

$$j_o = A_{Pt} \upsilon_{Pt} i_0^{Pt/N} \tag{2.19}$$

The platinum surface area per unit volume (A_{Pt}) is determined from the platinum loading (m_{Pt}), platinum surface area per unit mass (s_{Pt}), and the width of the catalyst layer (W_{CL}):

$$A_{Pt} = m_{Pt} s_{Pt} / W_{CL} \tag{2.20}$$

To account for the utilization of the total platinum surface area, an empirical relationship between the Nafion content in the catalyst layer and utilization is employed. Sasikumar *et al.* [51] presented the relationship between utilization and

Nafion content in their experimental study. The utilization data were obtained using the ratio of electrochemical surface area measured with cyclic voltammetry to the theoretical value for a platinum/carbon ratio of 20% Pt/C. The results for an electrode with a platinum loading (m_{Pt}) of 0.25 mg cm^{-2} are shown in Figure 2.4. The platinum utilization (υ_{Pt}) data have been fit to a third-order polynomial that is presented in Eqn. (2.21) and Figure 2.4. The optimum Nafion content (y_N) from a utilization standpoint is approximately 35-40 wt. %; this is similar to other results [3].

$$\upsilon_{Pt} = 1.833\times10^{-5} y_N^3 - 2.807\times10^{-3} y_N^2 + 1.332\times10^{-1} y_N - 1.476 \qquad (2.21)$$

The initial increase in utilization with higher Nafion content, shown in Figure 2.4, is the result of the increased connectivity of the electrolyte. In addition, this trend represents higher electrolyte coverage of the platinum surface. It is hypothesized that the later decline in utilization with further increase in Nafion content is the result of reduced electrical connectivity of the catalyst particles. The high Nafion content should increase the mean distance between carbon particles, which would decrease the connectivity.

The exchange current density of the platinum/Nafion interface and its temperature dependence is obtained from the experimental work of Beattie *et al.* [52]. The microelectrode analysis of Beattie *et al.* is in agreement with those of Parthasarathy *et al.* [42] and Zhang *et al.* [53]. However, the Beattie *et al.* study features better repeatability between studies of temperature and pressure dependence. The interfacial exchange current density is extracted from the high current density portion of the Tafel curves (Langmuirian conditions). This region results from the loss of the oxide

layer found at low current densities. An empirical correlation for the interfacial exchange current density as a function of temperature is expressed as:

$$i_o^{Pt/N} = 6.379\times10^{-14}\exp(6.782\times10^{-2}T) \tag{2.22}$$

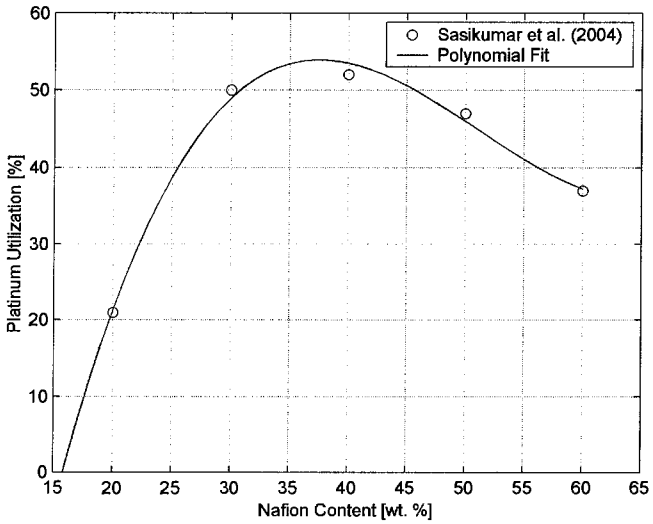

Figure 2.4: Platinum utilization versus Nafion content as experimentally determined by Sasikumar et al. [51] for a electrode featuring a platinum loading of 0.25 mgPt cm^{-2}. The 3rd order empirical fit of Eqn. (2.21) is also shown.

2.2.4 Interface model of the anode catalyst layer

Due to the faster kinetics of anode reaction in PEM fuel cells, the low conductivity of the electrolyte drives the anode reaction into a thin strip next to the membrane. This can be revealed by the expression for the width of the reactive strip in a catalyst layer developed by Kornyshev and Kulikovsky [54]. Therefore, in contrast with the cathode, it is much more acceptable to model the anode catalyst layer as an interface. A contributing factor to modelling the anode as an interface is the need to employ the full Butler-Volmer equation. The lower overpotential in the anode can undermine the

validity of the Tafel equation. It thus requires the more suitable full Butler-Volmer formulation. The influence of hydrogen concentration on the anode's exchange current density (i_o^A) is neglected and is considered constant. The equation for the interfacial anode reaction is formulated with the complete Butler-Volmer equation as:

$$i = i_o^A \left[\exp\left(\frac{\alpha_a F}{RT} \eta^A \right) - \exp\left(-\frac{\alpha_c F}{RT} \eta^A \right) \right] \tag{2.23}$$

2.2.5 Solution approach

The equations presented in the previous section are solved with non-discretized analytical approaches. Numerical techniques such as finite-element, finite difference, or finite-volume or control volume methods were not employed. The one-dimensional MEA model uses the bisection algorithm to solve the set of equations. The function solved is the difference between the current calculated in the cathode and the current calculated in the anode ($f = i_C(\eta^C) - i_A(\eta^A)$). The independent variable is the cathode overpotential at the membrane interface (η^C). The overpotential in the anode is determined from the expression $\eta^A = (E_{OC} - E_{cell}) - \eta^C - W_{Mem}\sigma_{Mem}^{-1} i_C(\eta^C)$, which results from the potential summation algorithm. The zero crossing, or root, of this function resolves the overpotential in the cathode catalyst layer.

The sub-routine for solving the finite-thickness catalyst layer model employs the Newton-Rhaphson method for solving the implicit catalyst layer model, which determines the overpotential distribution and current generation in the cathode. In this subroutine the Newton-Rhapson function is the difference between the previous

solution of the overpotential at the catalyst layer/GDL interface ($x = W_{CL}$), and that determined by Eqn.(2.11); $f = \eta_o - \eta(W_{CL})$.

2.3 Results and discussion

To evaluate the present model, comparisons are made with the experimental results of Sasikumar *et al.* [51]. This study is an appropriate reference because of the special attention paid to the catalyst layer specifications and the wide scope of the parametric study. In addition, Sasikumar *et al.* used oxygen instead of air, allowing for better validation of the MEA model (there is significantly less mass transport influence). There are typically a large number of ambiguities associated with mass transport limitations (i.e. liquid water flooding and flow field design) that deteriorate the validation of a one-dimensional and single-phase model.

2.3.1 Properties and parameters

The operating conditions and fuel cell features are listed in Table 2.1. The operating conditions represent the experimental conditions of the Sasikumar *et al.* study [51]. This includes a cell temperature of 80°C and fully humidified oxygen and hydrogen gas streams at a pressure of 1 atm. Moreover, a membrane width of 125 μm is used to represent the Nafion 115 membrane employed in the experimental study.

Table 2.1: Operating conditions.

Property	Value
Air pressure, P_{air}	1atm
Fuel pressure, P_f	1atm
Fuel cell temperature, T	353K (80°C)
Relative humidity	100%
Membrane thickness (Nafion 115), W_{Mem}	125 μm

Table 2.2 lists the catalyst layer properties and parameters. A key property is the void fraction, which is specified as 55% (based on the results of Navessin [55]). Also, a platinum/carbon ratio of 20% Pt/C was studied. As a result of a theoretical symmetry factor (β) of 0.5 [52], the transfer coefficient (α) for the rate limiting step in the oxygen reduction reaction is considered to be 1 ($\alpha = 2\beta$). Although Beattie *et al.* [52] presented variations in the symmetry factor with temperature, they conjectured that these uncharacteristic results were likely caused by membrane impurities. Zhang *et al.* [53] had similar findings. Another parameter worth mention is the reference oxygen concentration in Eqn. (2.10). The molar density of oxygen at three atmospheres of pressure (113 mol m^{-3}) is used to correlate the exchange current density of Beattie *et al.* [52] to other gas pressures and concentration polarization. In lieu of a comprehensive mass transfer model, the oxygen concentration in the catalyst layer is set to a reduced value of 5 mol m^{-3}.

Table 2.2: Catalyst layer properties and parameters.

Property	Value
Catalyst layer void fraction, ε_V	55% [55]
Membrane conductivity, $\sigma_{Mem,Bulk}$	6.94 S m^{-1} [56]
Platinum/Carbon ratio, y_{Pt}	20 % Pt/C
Platinum surface area, s_{Pt}	1120 cm^2 mg^{-1}
Platinum density, ρ_{Pt}	21500 kg m^{-3}
Nafion density, ρ_N	1900 kg m^{-3}
Carbon density, ρ_C	2267 kg m^{-3}
Cathode transfer coefficient, α	1 [52] [53]
Anode transfer coefficient, α_a & α_c	1 [50]
O_2 concentration, c_{O2}	5 mol m^{-3}
H_2 concentration, c_{H2}	34.3 mol m^{-3}
O_2 concentration exponent, γ_{O2}	1.03 [52]
H_2 concentration exponent, γ_{H2}	0.5 [50]
O_2 reference concentration, c_{O2}^{ref}	113 mol m^{-3} [52]
H_2 reference concentration, c_{H2}^{ref}	40.88 mol m^{-3} [50]
Anode exchange current density, i_o^A	6 x 10^3 A m^{-2} [41]

2.3.2 Model validation

The efficacy of the analytical MEA model is evaluated by comparing its results to the experimental data of Sasikumar *et al.* [51]. The predictive capability of the macrohomogeneous model is measured by the difference in response to changes in the catalyst layer specifications between the model and the experimental observations. In the following results, the platinum loading varies between 0.10 and

0.25 mgPt cm^{-2} and the Nafion content is specified in the range of 20 to 60 % wt. Over this spectrum of specifications, the main modelling parameters influenced are the volumetric exchange current density, the catalyst layer width, and the effective conductivity. The resulting parameters for four points in this spectrum of specifications are presented in Table 2.3.

Table 2.3: Catalyst layer properties resulting from the macrohomogeneous model.

Configuration (Pt. Loading | Nafion Content)	Volumetric Exchange Current Density [A m^{-3}]	Catalyst Layer Width [μm]	Nafion Volume Fraction [%] (effective conductivity [Sm^{-1}]) [1]
0.10 mgPtcm^{-2} | 40 % wt.	13355	6.9	25 (0.88)
0.25 mgPtcm^{-2} | 40 % wt.	13355	17.4	25 (0.88)
0.25 mgPtcm^{-2} | 20 % wt.	6825	13.7	12 (0.29)
0.25 mgPtcm^{-2} | 60 % wt.	6088	27.1	36 (1.57)

[1]Bulk conductivity = 6.94 S m^{-1}

As discussed in the development of the model, a change in platinum loading impacts only the catalyst layer width. The volumetric exchange current density and effective conductivity are unchanged. In contrast, the results in Table 2.3 show that changing the Nafion content has a significant impact on all three parameters. It is evident in the table that there is a maximum value to the volumetric exchange current density at approximately 40% wt. The volumetric exchange current changes with respect to Nafion content based on utilization data (see Figure 2.4). However, the reduction at higher Nafion contents is due to the diminishing platinum concentration as the layer expands.

Figure 2.5 presents the polarization curves of two validation cases with platinum loadings of 0.10 and 0.20 mgPt cm^{-2}. Both cases feature a Nafion content of 40% wt. It can be seen, especially for 0.10 mgPt cm^{-2}, that there is excellent agreement between the experimental curves of Sasikumar *et al.* [51]. In addition, it is evident that the variable-width macrohomogeneous model reasonably tracks the influence of changing the platinum loading to 0.25 mgPt cm^{-2}.

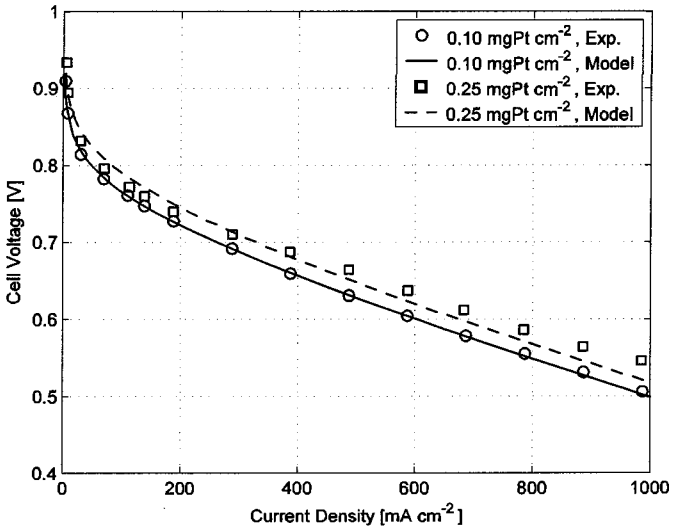

Figure 2.5: Comparison between polarization curves obtained experimentally by Sasikumar et al. [51] and those calculated by the present model for platinum loadings of 0.10 and 0.25 mgPt cm^{-2}.

Figure 2.6 depicts the response of the polarization curve obtained by the model when the Nafion content varies. It also shows that the model's accounting of Nafion content agrees well with the experimental observations of Sasikumar *et al.* [51]. In the experimental data, increasing the Nafion content from 20 to 40 % wt. significantly improves performance and an increase from 40 to 60 % wt. worsens performance to a lesser degree. This same trend is found with the model. Although the catalyst layer

conductivity is almost doubled at a Nafion content of 60 % wt., the cell exhibits a small drop in performance due to reduced utilization and a longer conduction distance.

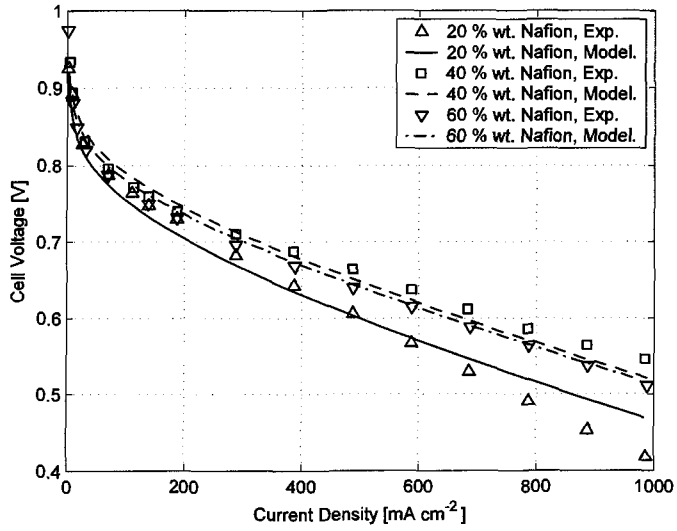

Figure 2.6: Comparison between polarization curves obtained experimentally by Sasikumar *et al.* [51] and those calculated by the present model for Nafion contents of 20, 40 and 60 % wt.

Figure 2.7 presents the modelled and experimentally observed influence of Nafion content on a catalyst layer with a platinum loading of 0.10 mgPt cm^{-2} at cell voltages of 0.6 and 0.7 Volts. Similar plots are also given for a platinum loading of 0.25 mgPt cm^{-2}. The plot shows that the agreement between the model and Sasikumar *et al.*'s [51] measurements for 0.10 mgPt cm^{-2} is not as good as that for 0.25 mgPt cm^{-2}. For the 0.10 mgPt cm^{-2} case, the model does not present the sharper peak in performance at a Nafion content of 50 % wt. This is likely the influence of using utilization data obtained for a catalyst layer with a platinum loading of 0.25 mgPt cm^{-2}. Thus,

utilization data over a wider range of platinum loadings would be valuable for further analysis. Nevertheless, the trends remain adequately captured.

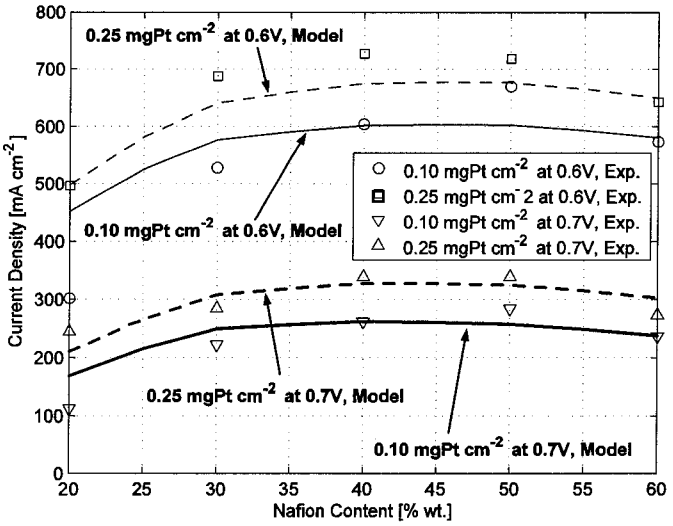

Figure 2.7: Current density versus Nafion content for multiple platinum loadings and cell voltages for the experimental results of Sasikumar et al. [51] and those calculated by the model.

Figure 2.8 provides a closer inspection of the impact that cathode catalyst layer specifications have on the overpotential profile in the layer. The plot compares overpotential profiles by plotting the difference between the local overpotential and the overpotential at the GDL/catalyst layer interface. The plot aptly depicts the effect that Nafion content has on the effective conductivity. The catalyst layer with the Nafion loading of 20 % wt. features the steepest slope; this is clearly because it has the lowest effective conductivity (see Table 2.3). For similar reasons, the layer with a Nafion loading of 60% wt. features the flattest slope due to its high effective conductivity. Changing the platinum loading has the singular effect of extending the

overpotential profile and does not affect the slope. This influence is due to the volumetric properties remaining constant and only the width adjusting.

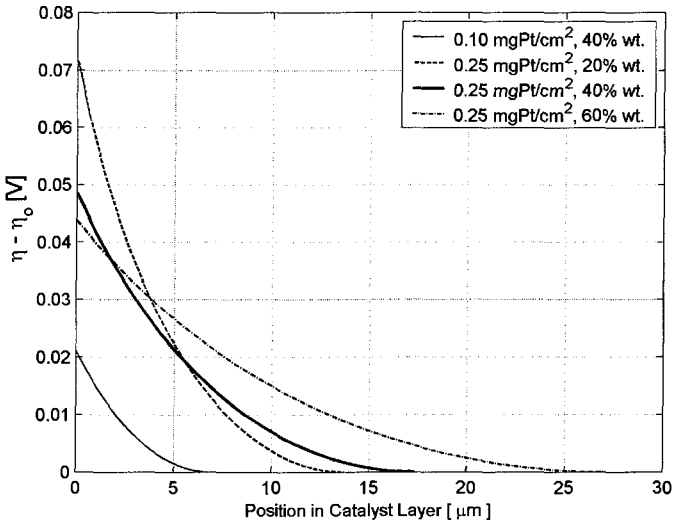

Figure 2.8: Overpotential profile in the cathode catalyst layer for four catalyst layer configurations.

2.4 Summary

This chapter presented a one-dimensional analytical model of the MEA in a PEM fuel cell. Emphasis was placed on the derivation of the system of equations that determine the catalyst layer properties and the transport of ions in the cathode. This emphasis stems from an intent to derive a MEA model for low-humidity operation of air-breathing micro-fuel cells where mass transport losses are less significant. The model featured a finite-thickness derivation for the cathode catalyst layer that accounts for the resulting ohmic losses. In addition, a macrohomogeneous representation of the catalyst layer was implemented with a variable-width formulation. This formulation

accounted for the change in the catalyst layer width based on its specifications. Many supplementary relationships were employed to determine the catalyst layer properties without resorting to fitting techniques.

The capability of the MEA model to predict variations in PEMFC performance when catalyst layer specifications are changed was demonstrated with comparisons to experimental data. Agreement with experimental data was found for all catalyst layer configurations. Thus, the macrohomogeneous model with the variable-width formulation features the ability to correlate the catalyst layer specifications to the layer's microstructure and subsequently translate the microstructure to volume-average parameters for modelling. This ability makes the present MEA model an excellent candidate for the optimization of catalyst layers and MEAs for PEMFCs operating under low-humidity conditions.

Chapter 3

Planar fuel cells

3.1 Introduction

Planar device integrated fuel cells feature a membrane electrode assembly that is parallel to the ambient air interface. A schematic of such a fuel cell is shown in Figure 3.1. This arrangement features multiple methodologies for reducing the size and number of ancillary components:

1. To alleviate the need for air distribution channels, along with the necessary pumps and fans, the cathode gas diffusion layer is in direct contact with the ambient air.

2. External humidification systems are eliminated and the fuel cell relies on the ambient relative humidity and water production in the cathode for the humidification of the membrane.

3. The circulating ambient air facilitates the cooling of the fuel cell in lieu of a dedicated heat management system.

4. The anode is fed dry hydrogen at roughly ambient temperature and pressure, eliminating hydrogen conditioning components.

5. Electrical current is distributed across the cell in an edge-collection arrangement.

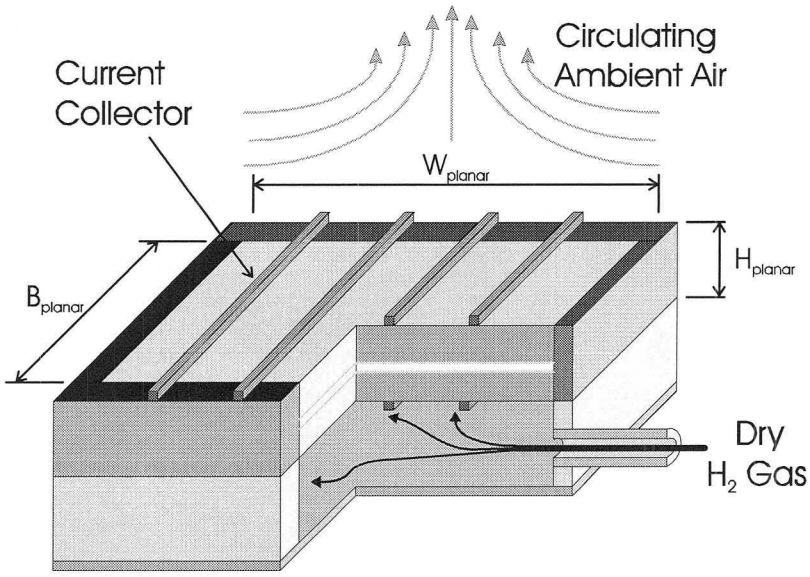

Figure 3.1: Schematic of the planar device integrated fuel cell.

The literature highlights three main examples of the planar device integrated fuel cell designs that passively breathe ambient air. The first design was presented by Wainright *et al.* [13] of Case Western Reserve University in 2003. The second and third designs were published by Schmitz *et al.* [12] and Hahn *et al.* [5] of the Fraunhofer Institute of Solar Energy Systems in 2004. All of these fuel cells follow the design principles previously listed.

The Wainright *et al.* [13] fuel cells were assembled on ceramic substrates with thick-film fabrication techniques. The design featured hydrogen storage in a reservoir wafer located directly below the anode; this is similar to the arrangement shown in Figure 3.1. Current was distributed in porous metal gas diffusion layers in which the current traveled through the gas diffusion layer parallel to the membrane. The long conduction distance and lowered conductivity of porous material resulted in large ohmic resistances.

The first Fraunhofer planar micro fuel cell, first presented by Schmitz *et al.* [12], was produced using printed circuit board (PCB) technology. In this design, the surface of the cathode gas diffusion layer was largely open to the ambient air. A plate with rectangular openings placed over the gas diffusion layer provided improved current conduction and allowed the passage of air to the cathode. The arrangement is similar to the current collectors depicted in Figure 3.1. The opening between current collectors was 1.5 mm and the thickness of the current collector was 1 mm. The active area of this fuel cell was 10 cm^2. The fuel cell was able to maintain a power density of 100 mW cm^{-2} at cell voltage of 0.5 V.

The second Fraunhofer planar micro fuel cell, depicted by Hahn *et al.* [5], was fabricated with wafer-level patterning technologies. The dimensions of this fuel cell were 1 cm × 1 cm × 200 μm; these dimensions are comparable with the fuel cells considered in this study. The fuel cell was able to operate in a stable manner at a power density of 80 mW cm^{-2} using dry hydrogen as the fuel. The electrical current was collected from the cathode's patterned flow-field/current collector that conducted electricity and allowed air to pass into the cathode from the ambient environment.

3.2 Model

The core of the planar device integrated fuel cell model is the analytical MEA model that was presented in Chapter 2. In this chapter, that model is expanded to include the additional phenomena that affect the performance of planar device integrated fuel cells when breathing ambient air. These additional phenomena include:

1. The transport of oxygen and water vapour between the surface of the GDL and the ambient air.

2. The diffusion of gases through the GDL.

3. The diffusion of oxygen into the catalyst layer.

4. The influence of temperature and humidity on the conductivity of the membrane.

5. The heat transfer from the fuel cell to the ambient air.

3.2.1 Assumptions

In addition to the assumptions used in the derivation of the analytical MEA model, the following list contains some of the major assumptions used in developing the model of the planar device integrated fuel cell. The justifications for these assumptions will be discussed in the derivation of the model.

1. Transport in the fuel cell is considered one-dimensional.

2. The fuel cell operates in steady state conditions.

3. Water vapour is produced in the cathode.

4. The water exists only as vapour.

5. There is zero net transport of water through the membrane.

6. The hydrogen supply is "dead-ended" and is not recycled.

7. The hydrogen supply is dry (zero humidity).

8. Water does not accumulate in the hydrogen storage system.

9. The water activity is uniform across the electrolyte in the membrane and catalyst layers and is equal to the water activity at the cathode interface of the gas diffusion layer and the catalyst layer.

10. Potential loss due to electrical conduction is neglected.

11. The anode side of the fuel cell is perfectly insulated against heat fluxes and heat only exits the fuel cell through the cathode surface.

3.2.2 Gas diffusion

The diffusion of gases through the gas diffusion layer is the result of the consumption of reactants and the supply of products in the catalyst layer. Herein, it is assumed that water exists only in the vapor phase. In the cathode, the local consumption of oxygen is simply expressed as a function of the local current:

$$S_{O2} = -\frac{M_{O2} i}{4F} \tag{3.1}$$

and the local source of water due to the reaction is:

$$S_{H2O} = \frac{M_{H2O} i}{2F} \tag{3.2}$$

The governing equation for gas transport in the GDL, assuming negligible advection, is Fick's law. When expressed in terms of a mass flux $\dot{n}_A$, the differential form of Fick's is expressed as:

$$\dot{n}_A = -\rho D_A^{eff} \nabla y_A \tag{3.3}$$

where D_A^{eff} is the effective molecular diffusivity of species A in the porous media and y_A is the mass fraction of species A. The density of air (ρ) is corrected for temperature using the ideal gas law. The diffusivity is corrected by porosity ε and the tortuosity factor τ of the porous gas diffusion media:

$$D_A^{eff} = \frac{\varepsilon}{\tau} D_A \tag{3.4}$$

The form of Fick's law employed herein is typically used for binary mixtures, not ternary systems such as the humidified air in the cathode. However, the diluted concentration of the oxygen and similar molecular weights of the species allows for this simplification. The binary diffusivity is calculated with the empirical method presented by Cussler [57]:

$$D_{AB} = \frac{T^{1.75}}{P} \frac{\sqrt{1/M_A + 1/M_B}}{(\phi_A^{1/3} + \phi_B^{1/3})} \tag{3.5}$$

The mass fractions at the interface (y_A^o) of the GDL with ambient air are determined by mass transfer coefficients (h_{O2}, h_{H2O}) extracted from previous CFD simulations [10]. The interface mass fractions are determined by:

$$y_{O2}^o = y_{O2}^{Amb} - \frac{1}{\rho h_{O2}} \frac{M_{O2} i}{4F} \tag{3.6}$$

$$y_{H2O}^o = y_{H2O}^{Amb} + \frac{1}{\rho h_{H2O}} \frac{M_{H2O} i}{2F} \tag{3.7}$$

where i is the current density of the fuel cell and y_A^{amb} is the mass fraction in the ambient air.

Considering the GDL as a homogeneous and isotropic porous medium, the oxygen and water mass fractions at the interface between the GDL and the catalyst layer ($y_A^{GDL/CL}$) can be derived from Eqn. (3.3). The mass fractions are determined with the expressions:

$$y_{O2}^{GDL/CL} = y_{O2}^{o} - \frac{W_{GDL}}{\rho D_{O2}^{GDL}} \frac{M_{O2} i}{4F} \tag{3.8}$$

$$y_{H2O}^{GDL/CL} = y_{H2O}^{o} + \frac{W_{GDL}}{\rho D_{H2O}^{GDL}} \frac{M_{H2O} i}{2F} \tag{3.9}$$

In addition, the oxygen mass fraction in the catalyst layer is approximated in order to capture the onset of reactant starvation. An approximation is derived by assuming a uniform reaction rate through the catalyst layer. The mass fraction employed is the value in the middle of the layer. The oxygen concentration obtained from this mass fraction is that specified in the Tafel equation. Notably, the average oxygen concentration in the catalyst layer is corrected for the reduced diffusivity in the catalyst layer, as done by Berg *et al.* [26]. The expression for the approximate catalyst layer mass fraction is:

$$y_{O2}^{CL} = y_{O2}^{GDL/CL} - \frac{M_{O2} i w^2}{32 F \rho D^{CL}} \tag{3.10}$$

3.2.3 Water transport through the membrane

It is assumed that there is zero net transport of water across the membrane. This assumption is facilitated by the assertion of a dry hydrogen supply and a "dead-ended" hydrogen distribution system. In addition, it assumed that water does not

accumulate in the hydrogen storage system. Thus, assuming steady state operation, there can be no water transport across the membrane due to species conservation. A similar assumption was made by Kulikovsky [27] in his semi-analytical 1+1 model. Moreover, this assumption is supported by the experimental results of Janssen and Overvelde [58]. They found that at a relatively low current density (400 mA cm^{-2}), while using dry air and hydrogen with low stoichiometries, the effective drag across the membrane was -0.01. Thus, a very small percentage of the product water was diffusing from the cathode to the anode.

It is also assumed that water activity is uniform across the membrane. This assumption is supported by the low current density and low humidity. For this circumstance, the electro-osmotic drag is minimal because it is proportional to the current and the water content of the membrane. Thus, diffusion from the cathode to the anode, which is less affected by water content than electro-osmotic drag [18], is the dominant mode of non-equilibrium transport. On the anode side, a water vapour concentration gradient develops to form a diffusion flux that offsets the advection of the hydrogen being consumed; this maintains a total water vapour flux of zero. Thus, the relatively small length scale of the membrane facilitates the assumption of uniform water content in the membrane.

3.2.4 Membrane conductivity

The potential drop through the electrolyte contributes significantly to the polarization of the fuel cell. An important aspect of polymer electrolyte membranes (PEM) is their ionic conductivity's dependence on water content. Thus, the membrane's efficacy relies on the humidification of both the anode and cathode. The membrane water

content (λ) is typically expressed as the number of water molecules per sulfonic head ($SO_3^-H^+$) in the polymer chain and is calculated as a function of water activity (a). Springer *et al.* [18] presented the water uptake isotherm for 303 K (30°C) as:

$$\lambda(a) = 0.043 + 17.81a - 39.85a^2 + 36a^3 \tag{3.11}$$

where:

$$a = \frac{x_{H2O}P}{P_{sat}(T)} \tag{3.12}$$

The expression for ionic conductivity employed herein is an empirical fit to the data presented by Sone *et al.* [56] for Nafion 117 without heat treatment. An assumption of equilibrium between water vapor in the gas phase and that in the membrane permits the use of this data. When considering the water in only the vapour phase, relative humidity and activity (Eqn. (3.12)) are interchangeable. The polynomial for ionic conductivity as a function of activity at 303 K is expressed as [56]:

$$\sigma_{303K} = 3.46a^3 + 0.0161a^2 + 1.45a - 0.175 \tag{3.13}$$

Sone *et al.*'s results also showed a variation of ionic conductivity with respect to temperature that was independent of relative humidity. However, Sone *et al.* did not provide a correlation for the influence of temperature. Thus, a temperature correction was derived from the Sone *et al.* results for the present study:

$$\sigma = \left(4.171\times10^{-4}T^2 - 0.2676T + 43.95\right)\sigma_{303K} \tag{3.14}$$

The influence of temperature and relative humidity, as predicted by Eqns. (3.13) and (3.14), is shown in Figure 3.2.

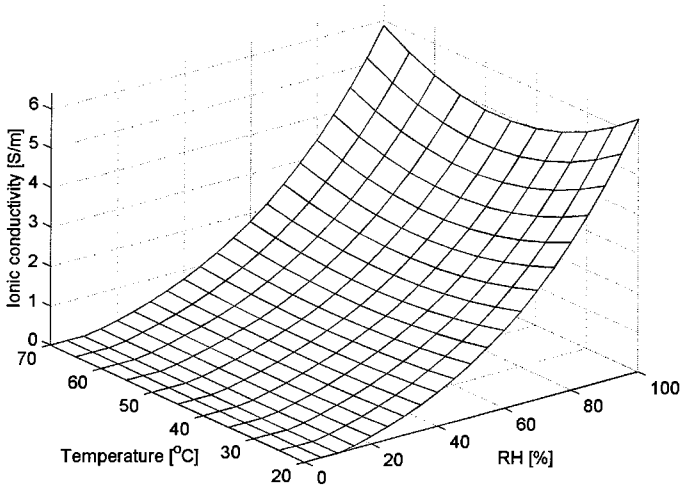

Figure 3.2: Conductivity correlation (Eqn.(3.14)) that was derived from the data of Sone *et al.* [56] data for a Nafion 117 membrane without heat treatment.

It is evident in Figure 3.2 that the influence of temperature is secondary in comparison to humidification. Also note that almost all conductivity is lost below a relative humidity of 20%. This approach has been chosen over the commonly implemented model of Springer *et al.* [18] because of that model's poor accuracy at low membrane water content. This approach also avoids using a water uptake isotherm ([26] and [50] for example), which could promote significant error when studying a range of temperatures [59]. In contrast, Thampan *et al.*'s [60] model predicts the conductivity well at low water contents but greatly differs from experimental values at higher water contents. A suitable replacement for the present

empirical approach would be the model of Fimrite *et al.* [59], which agrees well with experimental data over a large range of water content.

Although the data of Sone *et al.* [56] was obtained experimentally for Nafion 117 (208 μm thick when hydrated), it will be used herein to model much thinner Nafion membranes, such as Nafion 112 (58 μm thick when hydrated). Slade *et al.* [61] presented an experimental comparison of the conductivities measured for a number of Nafion membranes of different thicknesses. Their results presented decreased conductivity with reduced membrane thickness. Slade *et al.* hypothesized that this was the result of the membrane fabrication process. Similiarly, Büchi and Scherer [62] found that the change in thickness from a Nafion 117 membrane to Nafion 112 membrane resulted in a 14% decrease in conductivity at 50°C as well as zero current. Nevertheless, the broad spectrum of environmental conditions studied by Sone *et al.* [56] make it one of the best sources of membrane conductivity data.

3.2.5 Heat transfer

Temperature assumes a critical role in the performance of PEM fuel cells because of its impact on relative humidity through the saturation pressure and reaction kinetics. Temperature is also significant for device integrated fuel cells because they passively dissipate the heat produced by the fuel cell and do not feature the complex cooling systems of full-scale PEMFC stacks. The response time of a fuel cell's temperature to changes in the fuel cell's heat production decreases as the length scale is reduced.

This relationship is shown by the equation for the heat transfer time constant for solid bodies with a spatially lumped temperature:

$$\tau = \frac{V}{A}\frac{\rho c}{h} \tag{3.15}$$

where V and A are the volume and surface area of the body, ρ is the density of the body, c is the specific heat, and h is the heat transfer coefficient. Thus, when the scale of the solid body is reduced, causing the volume to surface area ratio (V/A) to decrease, the time constant of the heat transfer reduces proportionally. To consider a solid body as having a spatially lumped temperature, the Biot number (Bi) should meet the condition:

$$Bi < 0.1 \tag{3.16}$$

The Biot number is the ratio of convection heat transfer from the solid body to the conductive heat transfer within the solid body. The Biot number is expressed as:

$$Bi = \frac{h\delta}{k_{sb}} \tag{3.17}$$

where δ is the conductive length scale and k_{sb} is the solid body conductivity. A conservative estimate of the Biot number is made by assuming a low thermal conductivity of 1 W m^{-1} K^{-1}. In addition, an estimated vertical height of 3mm for the entire fuel cell is used as the conductive length. This dimension is chosen because the principal direction of heat transfer through the fuel cell is expected to be vertical. A heat transfer coefficient of 10 W m^{-2} K^{-1} is assumed for this characterization and is

applicable to natural convection cooling. With these parameters, the Biot number for the fuel cell is approximately 0.03. With this low Biot number, the heat transfer modelling of the fuel cell can proceed using a spatially lumped temperature assumption. This assumption is supported by CFD modelling, which predicts minimal temperature variation within these fuel cells [10].

The heat generated in the fuel cell is a combination of the heat of reaction and an array of irreversibilities. The heat of reaction is the difference between the change in the enthalpies of the incoming and outgoing fluid streams (Δh) and the energy converted into electricity or the change in Gibbs free energy (Δg). The heat of reaction is also the product of the temperature and the change in entropy ($\triangle s$) between the incoming and outgoing fluid streams:

$$T\Delta s = \Delta h - \Delta g \tag{3.18}$$

The irreversibilities of the fuel cell can be summed into the difference between the reversible open-circuit potential and the cell potential ($E_{OC} - E_{cell}$). Thus, overall heat production (q_p) can be expressed as the product of the heat of reaction and reaction rate ($i/2F$) plus the product of the voltage loss due to irreversibilities and the current density:

$$q_p = \left\{ \frac{T(-\Delta s)}{2F} + \left(E_{OC} - E_{cell}\right) \right\} i \tag{3.19}$$

The heat generated by the fuel cell is assumed to be rejected by convection through the exterior surfaces of the fuel cell and by radiative heat transfer to the surroundings. It is also assumed that no heat is transferred into the device that houses the fuel cell. The overall heat transfer to the environment (q_t) can be expressed as:

$$q_t = \frac{A_A}{A_S}\left\{h\left(T - T_\infty\right) + \varepsilon_r \sigma_r \left(T^4 - T_\infty^4\right)\right\} \tag{3.20}$$

where A_A is the electrochemically active area, A_S is the surface area, T_∞ is the temperature of the ambient environment, ε_r is the radiative emissivity of the fuel cell's top surface, and σ_r is the Stefan-Boltzmann constant. For planar fuel cells with heat transfer from the cathode surface only, the ratio A_A / A_S is equal to one. In addition, h is the convective heat transfer coefficient accounting for the rate at which heat can be advected from the fuel cell by surrounding air currents. The Nusselt number (Nu), which is a non-dimensional ratio of heat convection to conduction, is commonly used to express the rate at which heat can be advected from a surface. The heat transfer coefficient can be determined from the Nusselt number with the expression:

$$h = \frac{Nu \cdot k}{l} \tag{3.21}$$

where l is the characteristic length of the geometry and k is the air's thermal conductivity. Herein, the characteristic length is that of the shortest side of the fuel cell.

An empirical correlation for the natural convection Nusselt number was obtained by Martorell *et al.* [63] for heated rectangular plates; this correlation is employed herein to model natural convection. The correlation was shown to agree well with experiments and numerical calculations for Rayleigh numbers (Ra) between 200 and 20,000. The Rayleigh number is a measure of the buoyancy forces generated by temperature differences. The Nusselt number correlation is expressed as:

$$Nu = 1.20 Ra^{1.75} \tag{3.22}$$

where the Rayleigh number is calculated with the following formula:

$$Ra = \frac{g \beta C_p}{\mu k} \Delta T l^3 \tag{3.23}$$

where g is the gravitational acceleration, β is the air's thermal expansion coefficient, C_p is the air's specific heat, and μ is the air's viscosity.

3.2.6 Solution procedure

The solution of the temperature and current density for a given cell potential is obtained using the classical bisection method. The robust bisection method is preferred over more rapidly converging approaches, such as Newton-Raphson, because the system of equations is highly sensitivity to temperature, causing other methods to fail. The bisection method begins with a bounded function with bounds on each side of the point at which the function crosses zero. The function is solved at the midpoint between these bounds. Subsequently, one of the bounds is replaced with that

midpoint depending on the function's sign and a new midpoint is calculated. This process repeats iteratively until the root of the function is satisfactorily determined.

The procedure begins by solving the current for a given potential with the temperature at the midpoint between the initial bounds. With two main exceptions, the current is solved with the method described in Chapter 2. The first exception is that the exchange current density of the cathode is corrected for the oxygen concentration in the catalyst layer and the fuel cell temperature. Second, the membrane and catalyst layer ionic conductivities are now determined from the relative humidity and temperature with the correlation presented in Section 3.2.4.

Based on that current and potential, the temperature is recalculated by iteratively solving Eqns. (3.19) and (3.20) until the condition $q_p = q_t$ is met. This temperature is then employed in the bisection method to redefine the bounds. This entire process repeats until the temperature is adequately determined.

3.3 Results and discussion

The influence of operating and ambient air conditions, and design parameters are now identified with the analytical MEA model and the correlations specific to the planar fuel cell that were introduced in this chapter. The operating and ambient air conditions include the temperature and relative humidity of the ambient air, as well as the convective air currents surrounding the fuel cell. The design parameters include both the gas diffusion layer's thickness and microstructure and the platinum loading

and Nafion content of the cathode catalyst layer. In addition, the model is compared to experimental results for an ambient air-breathing fuel cell. Notably, the necessity of using the improved membrane correlation, which was introduced in Section 3.2.4, is shown by contrasting the results it provides to that of the Springer correlation [18].

3.3.1 Base-line properties and parameters

Table 3.1 lists the base-line operating conditions used in the following study of planar device integrated fuel cells. The dimensions of the fuel cell are considered similar to the fuel cell presented by Hahn *et al.* [5] (1 cm × 1 cm). Thus, the length scale used in the heat convection correlations is 1 cm. The ambient air temperature of 293 K (20 ^{o}C) and the ambient relative humidity of 60% have been selected because of their broad applicability. The prescribed Nusselt number of 10 is moderately greater than that feasible by natural convection alone to represent the effect of plausible larger ambient air currents.

Table 3.1: Operating conditions for the planar device integrated fuel cell.

Property	Value
Heat transfer length scale, l	1 cm
Air pressure, P_{air}	1atm
Fuel pressure, P_f	1atm
Ambient air temperature, T_∞	293K (20°C)
Ambient relative humidity	60%
Nusselt number, Nu	10
Radiative emissivity, ε_r	0.8

The properties of the gas diffusion layer are presented in Table 3.2. The thickness and porosity is that typical of carbon papers that are commonly employed in conventional PEM fuel cell stacks [64]. The tortuosity value of 2.5 is an estimated value due to a lack of empirical data. The oxygen and water vapour mass transfer coefficients (h_{O2}, h_{H2O}) were determined from a CFD analysis of an ambient air breathing microstructured fuel cell [10].

Table 3.2: Gas diffusion layer properties of the planar device integrated fuel cell.

Property	Value
GDL thickness, W_{GDL}	200 μm
GDL porosity, ε_{GDL}	0.8
GDL tortuosity, τ_{GDL}	2.5
Oxygen mass transfer coefficient, h_{O2}	13 m s^{-1}
Water vapour mass transfer coefficient, h_{H2O}	14.5 m s^{-1}

Table 3.3 presents the catalyst layer properties and parameters used in the study of planar device integrated fuel cells. These catalyst layer properties and parameters are generally unchanged from the study of the analytical MEA model in the previous chapter. The base-line catalyst layer features a relatively low platinum loading of 0.25 mg cm^{-2} to correspond with state-of-the-art PEMFC electrodes [3]. The catalyst layer also features a Nafion content of 40% wt., which is higher than the common 33 % wt. [3]. This higher value was chosen because of the diminished electrolyte conductivity during low-humidity operation and the reduced mass transfer limitations at low current densities. Unlike the validation of the analytical model in Chapter 2, which

used a correlation for the Gibb's free energy of formation for liquid water to determine the reversible open-circuit potential, the model of ambient air breathing fuel cells uses interpolated values from thermochemical tables [65] for the production of water vapour.

Table 3.3: Catalyst layer properties and parameters of the planar device integrated fuel cell.

Property	Value
Platinum loading, m_{Pt}	0.25 mg cm^{-2}
Nafion content, y_N	45 % wt.
Catalyst layer void fraction, ε_V	55% [55]
Platinum/Carbon ratio, y_{Pt}	20 % Pt/C

3.3.2 Temperature

Isothermal polarization curves were first generated to demonstrate the impact of fuel cell temperature on the performance of planar device integrated fuel cells. The physical analog of these isothermal curves is the performance of these fuel cells with ideal temperature regulation. The polarization curves were generated for fuel cell temperatures between 303 K (30 °C) and 328 K (55 °C) in 5 K intervals. The isothermal polarization curves are presented in Figure 3.3. These plots demonstrate the increasing deterioration of performance as the fuel cell temperature steadily increases. At the highest temperature shown, 328 K (55 °C), the fuel cell generates negligible current across the entire spectrum of cell voltage. However, for the remainder of the curves shown, the current rapidly increases once a critical potential is reached. The rapid increase in current presents itself in the almost horizontal slope

of the polarization curves at high current densities. This critical potential is most evident in the curve for 323 K (50 °C) and represents the potential drop necessary to overcome the low membrane conductivity.

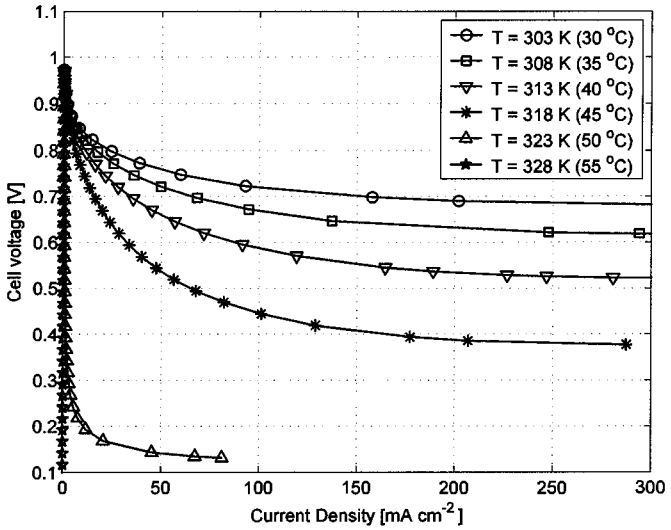

Figure 3.3: Isothermal polarization curves for the planar air-breathing fuel cell.

The rapid increase in current at a critical potential is the result of the positive feedback introduced by the coupling of the membrane conductivity's dependence on humidity with the water production in the cathode catalyst layer. The positive feedback of current density on membrane conductivity, at a constant temperature, is depicted in Figure 3.4. Both the first and second derivatives of the membrane conductivity with respect to the current density are positive, indicating the positive feedback.

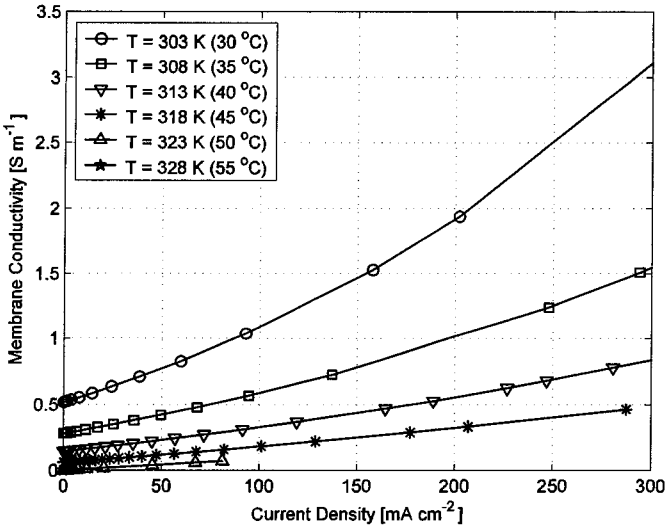

Figure 3.4: Isothermal curves of membrane conductivity versus current density.

The increase in membrane conductivity with rising current density for isothermal polarization curves is directly related to the increase in relative humidity shown in Figure 3.5. This plot shows a linear relationship between the relative humidity and the current density. By observing Figure 3.5 in conjunction with the polarization curves in Figure 3.3, it is evident that the onset condensation and two-phase transport will eventually occur at lower cell voltages. The presence of liquid water would ultimately discontinue the positive feedback between membrane conductivity and current density and introduce mass transfer limitations. However, two-phase phenomena are neglected herein and the negative feedback associated with liquid water accumulation is not present.

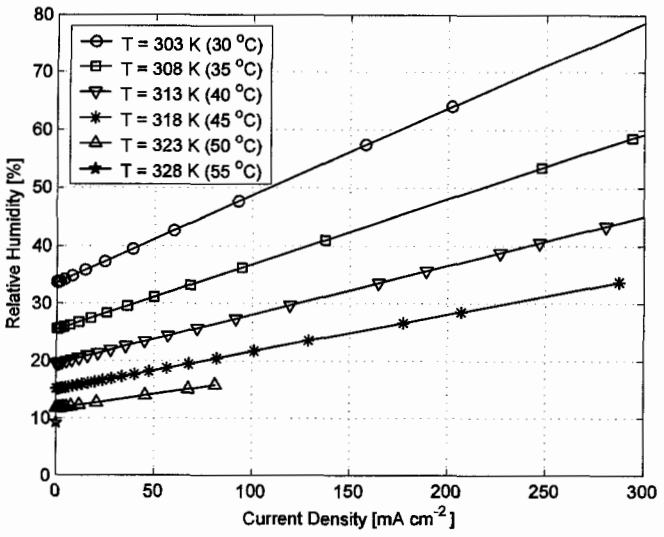

Figure 3.5: Isothermal curves of the membrane relative humidity at the interface of the GDL and the catalyst layer.

A similar "ignition" phenomenon was observed experimentally by Moxley *et al.* [66]. They found a critical initial membrane water content at which the fuel cell would auto-humidify for a given load resistance. In this study, for a given cell voltage and ambient conditions there is a critical "ignition" fuel cell temperature. Figure 3.6 depicts the impact of fuel cell temperature on current density for a cell voltage of 0.7 V. The plot shows that the fuel cell can adequately self-humidify at temperatures below 313 K (40°C). Above this temperature the low relative humidity cannot be sufficiently overcome and the membrane resistance remains high.

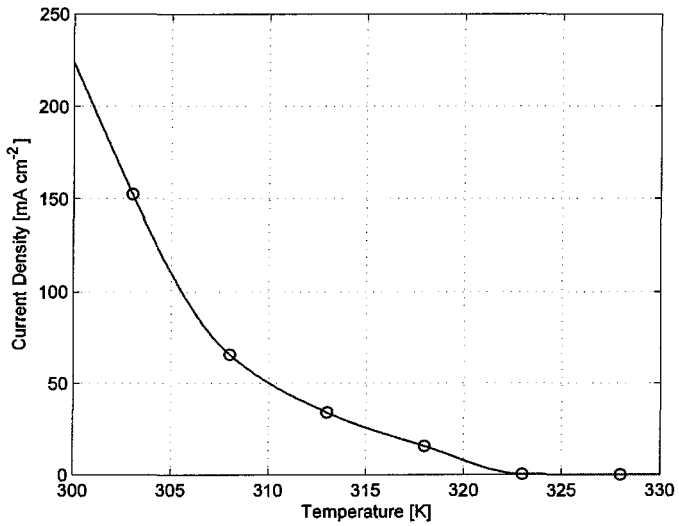

Figure 3.6: Effect of fuel cell temperature on current density at cell voltage of 0.7 V.

3.3.3 Comparison with experiment

To demonstrate the validity of the model, a comparison was conducted between the model and experimental results for a planar ambient air-breathing fuel cell with an active area of 10 cm^2. The experimental results were those of Schmitz *et al.* [12]. Their micro fuel cell was fabricated using printed circuit board technology in which the cathode and anode plates were constructed from ordinary printed circuit boards with a thin copper layer for current conduction. The MEA, however, was a rather conventional arrangement for PEMFCs. Figure 3.8 illustrates the Schmitz *et al.* fuel cell.

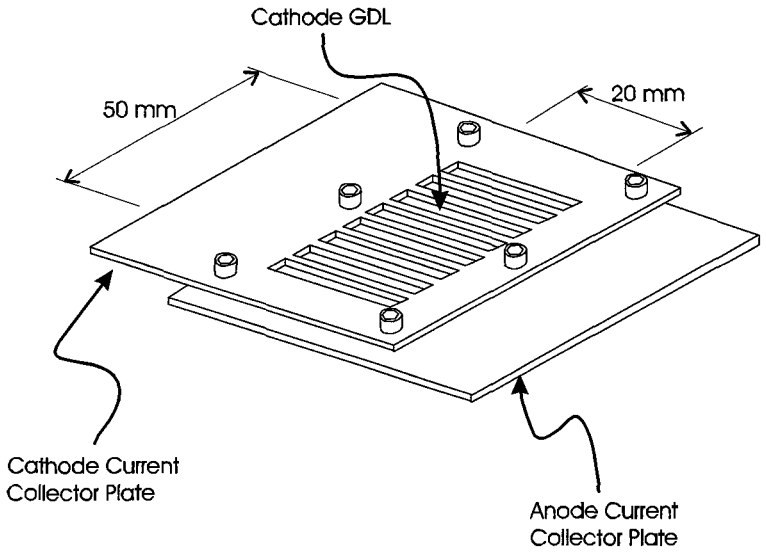

Figure 3.7: Illustration of the planar ambient air-breathing fuel cell that was fabricated by Schmitz *et al.* [12].

Some modifications were made to the fuel cell model's properties and parameters to reflect the experimental fuel cell; these changes are listed in Table 3.4. With the exception of the area specific heat transfer coefficient $h\left(A_S A_A^{-1}\right)$, all of the parameters listed in Table 3.4 were given in the Schmitz *et al.* [12] paper. To calculate this parameter, the experimentally observed ~15 K temperature difference between the fuel cell and the ambient air at a cell voltage of approximately 0.65 V and current density of 100 mA cm^{-2} was used in the set of heat production and transfer equations presented in Section 3.2.5. An area specific heat transfer coefficient of 38.0 W $m^{-2}K^{-1}$ was calculated. This heat transfer coefficient would correspond to a Nusselt number of approximately 14.6 when considering the 1 × 1 cm fuel cell that is simulated in subsequent sections.

Table 3.4: Adjusted parameters and conditions to match experiments of Schmitz et al. [12]

Parameter	Value
Platinum loading	0.3 mgPt cm^{-2}
GDL thickness, W_{GDL}	350 μm
Area specific heat transfer coefficient, $h\left(A_S A_A^{-1}\right)$	38.0 W $m^{-2}K^{-1}$
Ambient temperature, T_∞	298 K (25 °C)
Ambient relative humidity	50 %

Two important features of the Schmitz *et al.* fuel cell that could not be accurately portrayed were the Gore membrane and the influence of the cathode current collectors on electrical ohmic losses and gas transport. At this time, no conductivity data exist in the open literature for the 35 μm Gore membrane found in Gore PRIMEA® 5510 MEAs. Due to its composite structure, it is assumed that the Gore membrane features a lower conductivity than Nafion membranes. The Gore membrane is fabricated by impregnating a polymer matrix with Nafion solution. Therefore, the Nafion conductivity correlation is employed and a membrane thickness of 50 μm is used in order to represent the lower conductivity. If viewed as applying a membrane porosity to the Nafion conductivity ($\sigma_{eff} = \varepsilon_{Mem}\sigma$) to represent the composite structure, this would represent a Nafion porosity of 70 %. Schmitz *et al.*'s paper did not provide the Nafion content of the cathode catalyst layer, but this does not greatly influence results within a reasonable range of Nafion contents (see Figure 3.28).

Figure 3.8 presents a comparison between the polarization curve obtained with the present model and the experimental curve of Schmitz *et al.* [12]. A limiting current density is evident in the polarization curve predicted by the model. Although the limiting current density presents like a mass transfer limitation, it is the result of membrane dry-out. The membrane dry-out is due to increased fuel cell temperatures at higher current densities.

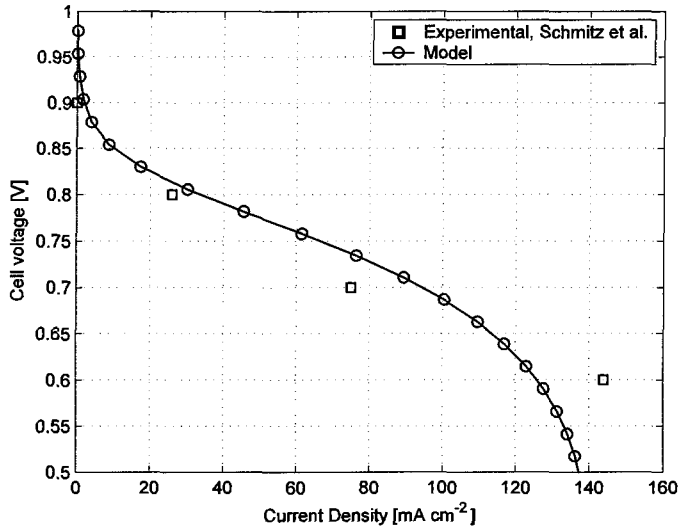

Figure 3.8: Comparison between the polarization curve obtained experimentally by Schmitz *et al.* [12] and that predicted by the model for the same conditions and specifications.

This comparison shows reasonable agreement between the Schmitz *et al.* data and the model. This is notable considering there was no tuning or fitting of the model and there being only four experimental points to compare. The percent difference in current density at each of the experimental cell voltages was below 22%. In addition, Schmitz *et al.* found that the cell voltage was approximately 0.66 V and the temperature ranged between 313 K (40 °C) and 317 K (44 °C) when the current

density was held at 100 mA cm^{-2}. At this current density, the model predicted a fuel cell temperature of 311 K (38 °C) with a cell voltage of 0.68 V. This demonstrates the reasonable accuracy of the rather simple heat transfer model employed in this analysis.

Nevertheless, the predicted membrane dry-out remains a significant discrepancy between the model and Schmitz *et al.* polarization curves. The Schmitz *et al.* polarization curve did not present membrane dry-out. Moreover, it did not present any form of limiting current, such as mass transfer limitations, when the cell voltage was swept from 0.9 V to 0.0 V. However, the rate of the polarization curve measurements was not presented. Moxely *et al.* [66] show that the equilibration of membrane water content can take anywhere from a few minutes to many hours. Thus, if the time interval between polarization curve measurements was quicker than the membrane equilibration time, the steady-state membrane dry-out phenomena predicted by the model would not present itself in the experimental polarization curve.

3.3.4 Membrane conductivity correlation

This section is devoted to demonstrating the necessity of the improved membrane conductivity correlation based on the prediction of fuel cell performance. Polarization curves were generated using the conductivity correlation extracted from the 1996 data of Sone *et al.* [56] (see Section 3.2.4) and that presented by Springer *et al.* [18] in

1991. Corrected for the temperature, the Springer conductivity $\sigma_{Springer}$ is expressed in Eqn. (3.24) as a function of water content (λ) [18].

$$\sigma_{Springer}(\lambda) = (0.005139\lambda - 0.00326) \cdot \exp\left[1268\left(\frac{1}{303} - \frac{1}{T}\right)\right] \tag{3.24}$$

The water content is calculated from the water activity with Eqn. (3.11). The Springer correlation is commonly employed for membrane conductivity when modelling PEM fuel cells [14, 18, 24, 48, 50, 67]. However, this correlation should not be employed for modelling ambient air-breathing PEM fuel cells operating in low humidity conditions [59]. The Springer correlation is a linear fit of conductivity to water content at higher relative humidities. The later works of Sone *et al.* and Fimrite *et al.* [59] show that this relationship is invalid for low water vapour activity. Figure 3.9 presents a comparison of membrane conductivity versus activity (or relative humidity) between the Sone and Springer correlations. The plots are generated for a temperature of 303 K (30 °C). The figure demonstrates that there is a very large disagreement between the two correlations at low relative humidities. In fact, at relative humidities of 30% and below, the difference approaches an order of magnitude Moreover, the Sone correlation better matches the experimental results of Sone *et al.* [56].

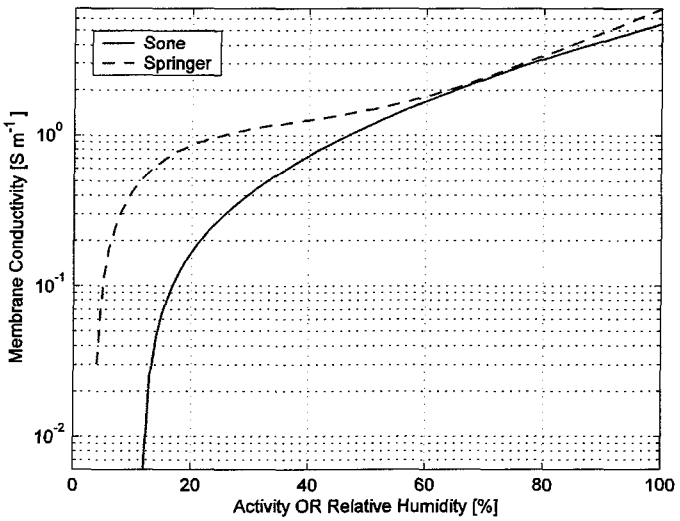

Figure 3.9: Comparison of the Sone (Eqn. (3.14)) and Springer (Eqn. (3.24)) correlations with plots of membrane conductivity versus activity (or relative humidity) for a temperature of 303 K (30 °C).

The polarization curves in Figure 3.10 demonstrate the detrimental impact of employing the Springer membrane conductivity correlation when modelling fuel cells operating in low-humidity conditions. The polarization curves show that the Springer correlation's over-prediction of the conductivity at low humidities increases the predicted limiting current by 140%. Thus, incorrect conclusions could be drawn due to the Springer correlation. Unfortunately, one of the few other published mathematical studies of planar micro fuel cells of this nature (Ziegler *et al.* [14]) employed the Springer correlation.

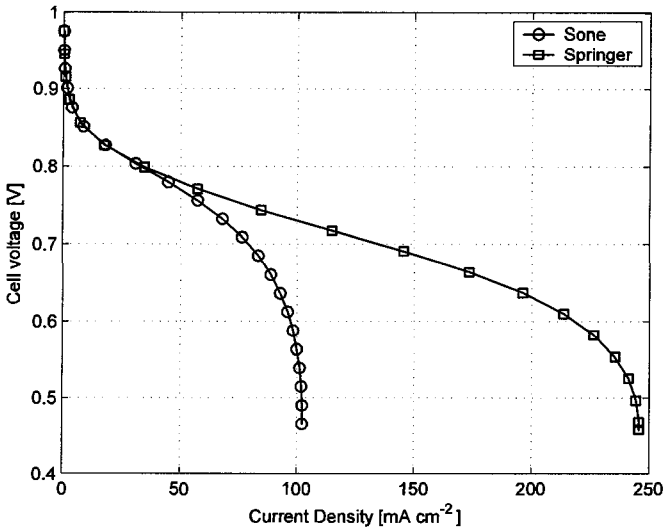

Figure 3.10: Polarization curves for the membrane conductivity correlations of Sone (Eqn. (3.14)) and Springer (Eqn. (3.24)).

3.3.5 Nusselt number

The influence of the air currents surrounding the planar device integrated fuel cell is investigated by specifying a range of fixed Nusselt numbers in the heat transfer model. Unlike Section 3.3.2 where the temperature was constant along each polarization curve, the temperature now varies along the polarization curve. The variation of the Nusselt number with the magnitude of air current's velocity can be determined from a number of correlations for forced convection over various geometries and flow directions [68]. Results for a range of Nusselt numbers are presented to maintain broad applicability and to refrain from selecting a particular arrangement of geometry and flow.

Figure 3.11 presents the polarization curves for Nusselt numbers between 1 and 20. It is evident in the polarization curves that the rate at which heat dissipates from the fuel

cell can dramatically affect performance. For a Nusselt number of 1 (negligible convection) the current density is heavily restricted. When the Nusselt number equals 20, the performance is greatly improved. A Nusselt number of 15 results in approximately the same heat transfer coefficient calculated for the Schmitz *et al.* [12] fuel cell. This Nusselt number is relatively high because the surface area is much greater than the active area as illustrated in Figure 3.7. As shown in the power density curves found in Figure 3.12, the increase in Nusselt number from 1 to 20 increases the maximum power density by 500%. These power densities agree well with the 80 mW cm^{-2} achieved by Hahn *et al.* [5] using their 1 × 1 cm ambient air-breathing micro fuel cell.

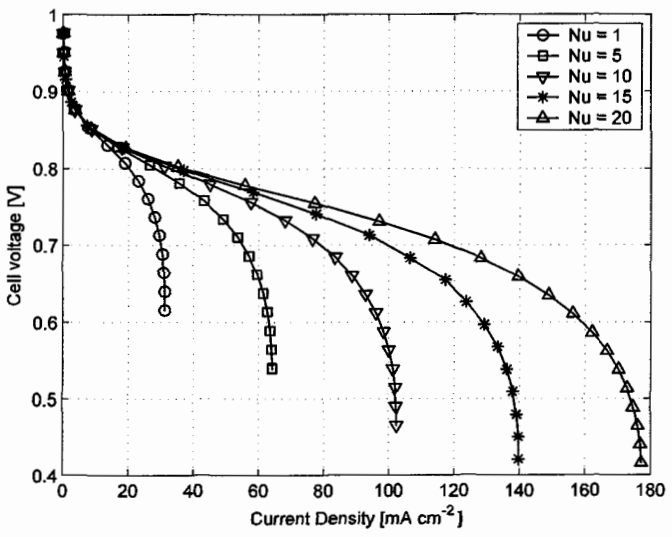

Figure 3.11: Polarization curves for a range of fixed Nusselt numbers.

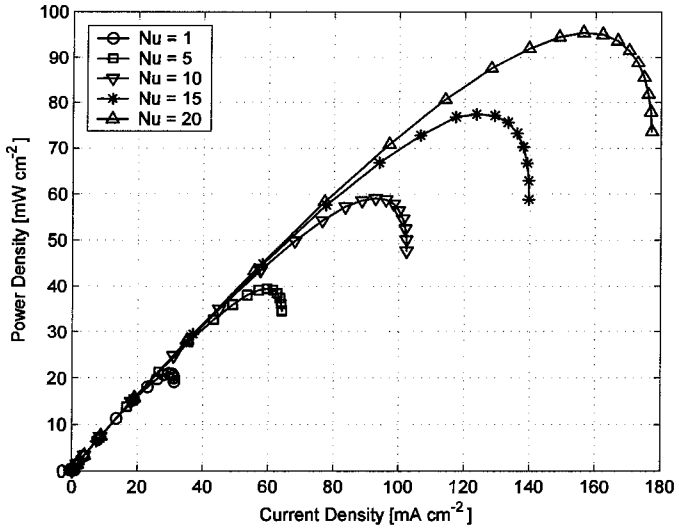

Figure 3.12: Power density versus current density for a range of fixed Nusselt numbers

Although the limiting current density shown in the polarization curves of Figure 3.11 resemble the common mass transfer limitation, the change in the oxygen concentration from the ambient air to the catalyst layer is insignificant at these low current densities. At the maximum current of 177.2 mA cm^{-2} the oxygen concentration at the catalyst layer interface was still 97% that of the ambient air. This minimal reduction in concentration has a negligible effect on fuel cell performance.

The limiting current results from the fuel cell temperature increasing, which causes the membrane conductivity to diminish via its dependence on the relative humidity. This drop in performance is typically referred to as membrane dry-out. This phenomena becomes evident when relating the plots of membrane conductivity (Figure 3.13), fuel cell temperature (Figure 3.14), and relative humidity (Figure 3.15) to the polarization curves (Figure 3.11). It is important to note that for all the Nusselt numbers considered, the limiting currents share a common temperature. Figure 3.14

indicates that the limiting current is associated with a temperature of approximately 318 K (45 °C).

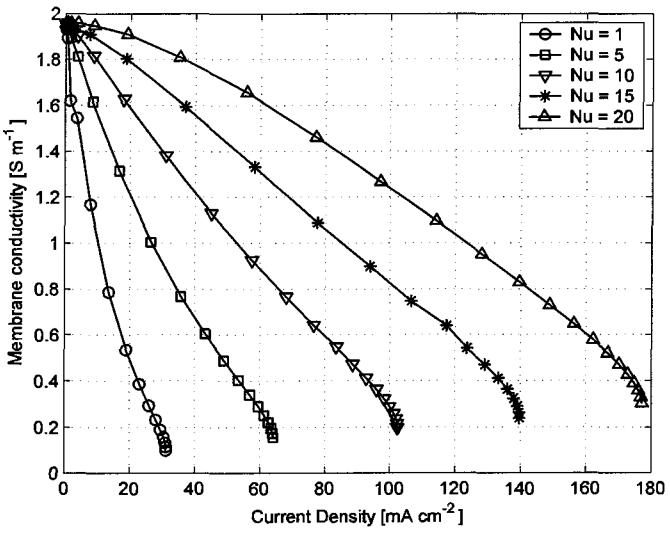

Figure 3.13: Membrane conductivity versus current density over a range of fixed Nusselt numbers.

The presence of a rate limiting current due to membrane dry-out is not an unprecedented phenomenon and is observed experimentally [69, 70]. Sena *et al.* [69] studied PEM fuel cells fed dry hydrogen and a fully-humidified oxidant of varying levels of oxygen concentration. They found that, under these conditions, oxygen concentration had little effect on the limiting current density and that the limitation was solely the result of increased membrane resistance. Sena *et al.* [69] state that: "These results clearly show that the fast decay of the cell performance at high current densities for Nafion® 117 and 115 is due to a marked increase in the membrane resistance." However, their study's fully humidified oxidant allowed for higher current densities than found in the present results. Therefore, the membrane dry-out in their results is largely due to electro-osmotic drag expelling water from the

membrane. It could also be partially due to a temperature rise; however, they did not present simultaneous temperature measurements. Previous studies of PEM fuel cells with dry reactants [69-71] typically feature an oxidant flow-field where the relative humidity increases along the flow channels, reducing the severity of the membrane dry-out.

The plots of temperature versus current density in Figure 3.14 depict the influence of irreversibilities on heat production within the fuel cell. Eqn. (3.19) shows that, when considering isothermal conditions, the heat of the reaction ($T\Delta s$) is a linear function of the current. However, the relative contribution of the heat of reaction to the total heat generation diminishes as the cell voltage lowers and the current increases. At lower cell potentials the majority of the heat generated is due to cell polarization. This is evident in the significant positive second derivative of the temperature curves. Moreover, the irreversibilities at the sharp drop in cell voltage due to membrane dry-out present themselves in the rapid rise in temperature near the end of each temperature curve.

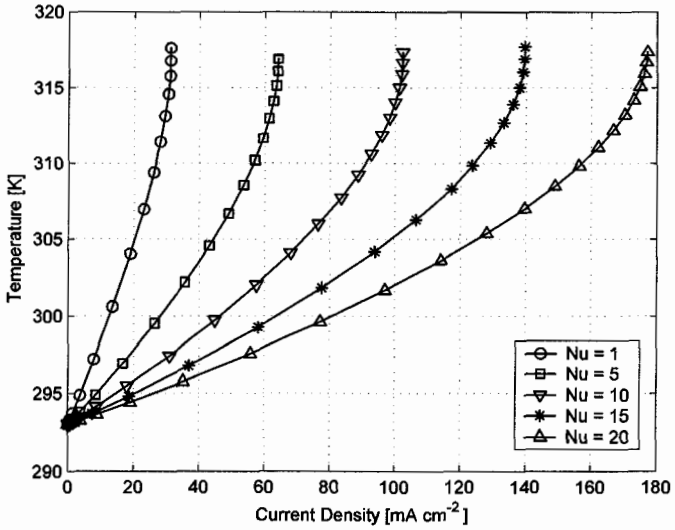

Figure 3.14: Temperature versus current density over a range of fixed Nusselt numbers.

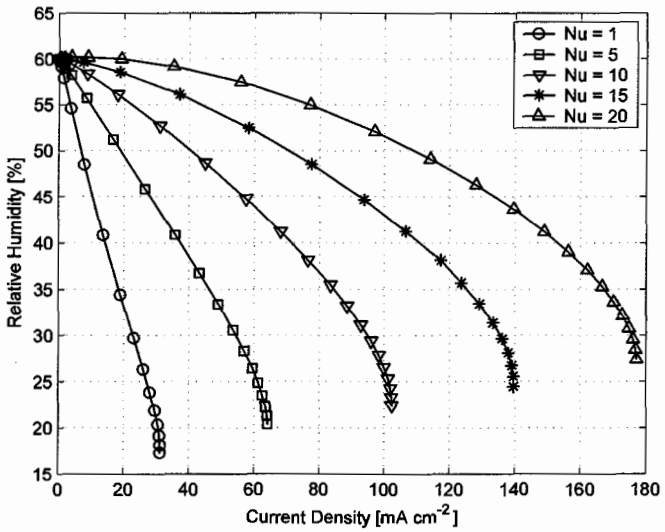

Figure 3.15: Membrane relative humidity versus current density over a range of fixed Nusselt numbers.

3.3.6 Natural convection

The Nusselt number correlations for natural convection above a rectangular heated plate, presented in Section 3.2.5, are now employed to model a micro fuel cell with completely passive cooling. The main distinction between the previous fixed Nusselt number cases and natural convection correlation is that the Nusselt number increases as the temperature increases; this constitutes passive temperature regulation. Thus, the heat generated by the fuel cell establishes the natural convection that helps to remove the heat. To show the impact of the variable natural convection Nusselt number, the natural convection results are compared to the results of two fixed Nusselt number cases.

Figure 3.16 presents the polarization curves for the natural convection Nusselt number correlation and Nusselt numbers of 1 and 5. The results show that the introduction of a variable Nusselt number due to natural convection does not dramatically change the polarization curve from the case of a Nusselt number of 5. The cause of this similarity is evident in the plot of the natural convection Nusselt number in Figure 3.17. This plot shows that the Nusselt number rises rapidly at low current densities, indicating that micro fuel cells can generate natural convection capable of improving the heat transfer rate. At the limiting current density, the Nusselt number reaches approximately 4.5; thus, the natural convection limiting current density is similar to that of a Nusselt number of 5.

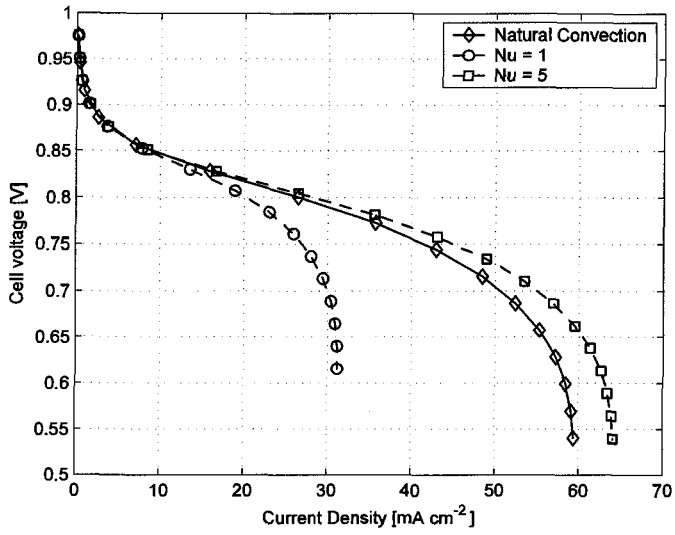

Figure 3.16: Polarization curves for natural convection and Nusselt numbers of 1 and 5.

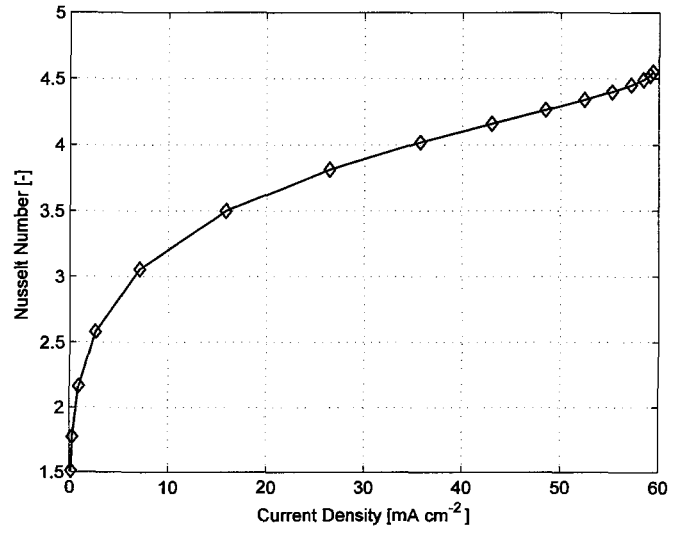

Figure 3.17: Natural convection Nusselt number versus current density.

Figure 3.18 presents the effect of the natural convection Nusselt number correlation on the temperature along the polarization curve. The influence is evident in the roughly consistent temperature difference between the natural convection case and

that of a Nusselt number of 5. The moderate temperature difference at low-current densities is a result of low natural convection Nusselt numbers in this range.

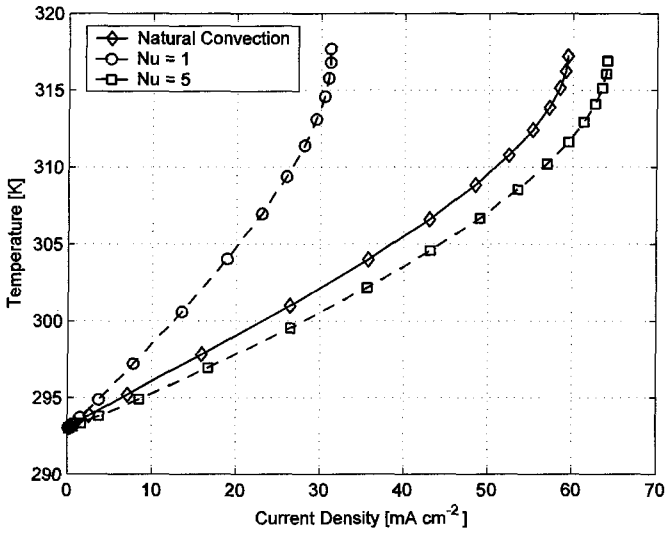

Figure 3.18: Temperature versus current density for natural convection and fixed Nusselt numbers of 1 and 5.

It is important to note that each of the cases in Figure 3.18 feature approximately the same temperature at the limiting current density. In addition, the polarization curve for natural convection (see Figure 3.16) does not vary significantly from the fixed Nusselt number case with a Nusselt number of 5. Thus, the performance of a passively cooled micro fuel cell is predictable using a fixed Nusselt number.

3.3.7 Ambient condition

The state of the ambient air can have significant impacts on the performance of device integrated fuel cells. The temperature and humidity of the ambient air both influence performance. These influences arise from the dependence of the fuel cell's performance on the membrane conductivity. Because the membrane conductivity has

significant consequences for fuel cell performance, and because portable electronics with device integrated fuel cells need to operate in variety of environments, it was deemed necessary to conduct a parametric study of the ambient air condition. Table 3.5 lists the range of ambient conditions that are studied. Temperatures range from 278 K (5 °C) to 308 K (35 °C) and relative humidity ranges from 30 % to 95 %.

Table 3.5: Ambient conditions.

Ambient condition	Temperature	Relative humidity
Moderate	293 K (20 °C)	60%
Cold and dry	278 K (5 °C)	30%
Cold and humid	278 K (5 °C)	95%
Hot and dry	308 K (35 °C)	30%
Hot and humid	308 K (35 °C)	95%

Figure 3.19 presents the polarization curves obtained for the ambient conditions listed in Table 3.5. The polarization curves show that the highest current densities are obtained when the ambient air features a high humidity. For the hot ambient air condition (35 °C), the limiting current density increases by 230% when the ambient relative humidity rises from 30 % to 95%.

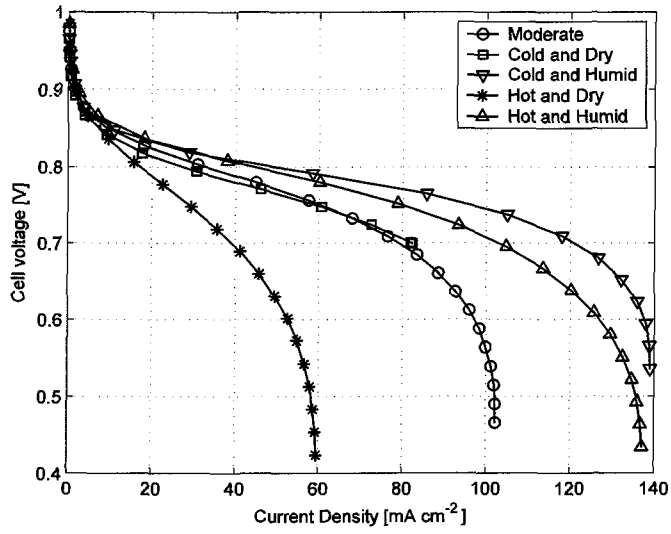

Figure 3.19: Polarization curves for five different ambient air conditions.

An unconventional result of improved performance at lower temperatures was obtained. Typically, performance increases with temperature due to the influence of reaction kinetics and liquid water flooding. The improved performance in colder temperatures found here result from improved self-humidification. As depicted in the study of the Nusselt number in Section 3.3.5, the water production in the cathode is not sufficient for humidifying the membrane as the influence of the rising temperature on the relative humidity has a larger effect. However, because less water is required to saturate the air at lower temperatures the fuel cell is better able to self-humidify. This phenomenon is most evident in Figure 3.20 in the plot of relative humidity versus current density for the "cold and dry" ambient condition. Unlike other ambient conditions, the plot for the "cold and dry" ambient condition shows the relative

humidity increasing with current density even though Figure 3.21 shows that the increase in fuel cell temperature with current density is comparable with the other ambient conditions.

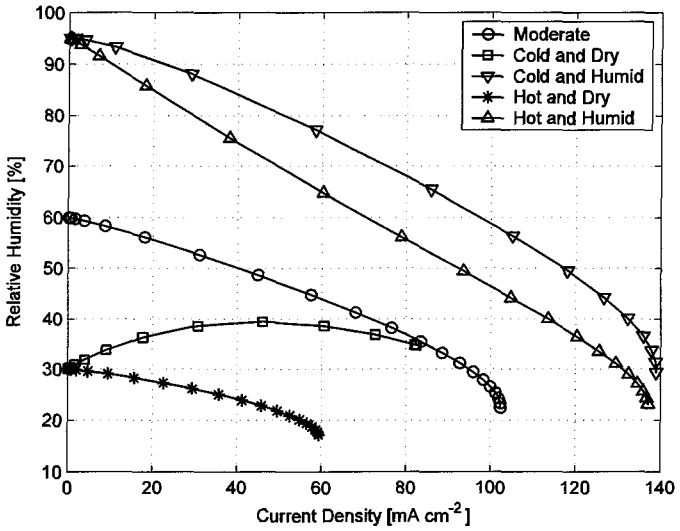

Figure 3.20: Membrane relative humidity versus current density for five different ambient air conditions.

The polarization curve, and other plots, for the "cold and dry" ambient condition were not able to proceed below a cell voltage of 0.7 V. The curve could not continue beyond this point because instabilities produced an intractable problem. At colder temperatures the system requires very little water production to increase relative humidity. However, a low ambient relative humidity restricts membrane conductivity. Those sensitivities introduce large instabilities. Notably, for a temperature of 278 K (5 °C) a solution of the limiting current density was only possible for ambient relative humidities of 70% and greater.

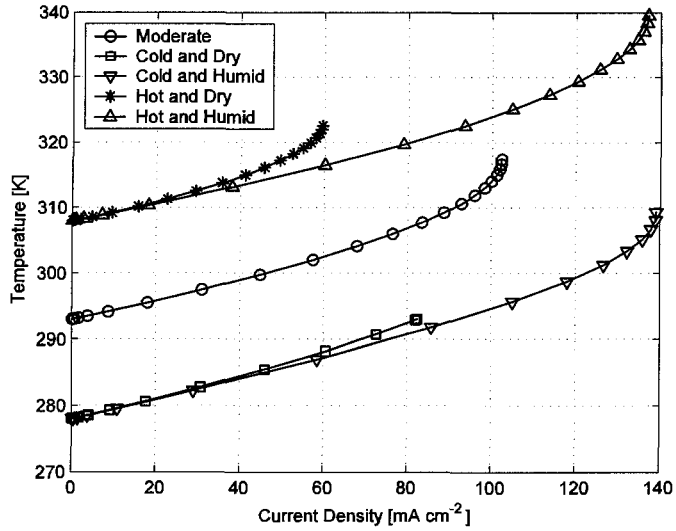

Figure 3.21: Temperature versus current density for five different ambient air conditions.

3.3.8 Gas diffusion layer

Beyond the GDL's typical roles as a conductor of electricity and as a gas conduit, the GDL also acts as an insulator of humidity for ambient air-breathing fuel cells. This insulating effect is a product of the porous GDL's resistance to the diffusion of product water to the ambient air. This resistance increases the water vapour concentration at the interface of the catalyst layer and GDL raising the internal relative humidity. The resistance to diffusion that the GDL introduces can be represented by an effective GDL thickness:

$$W_{GDL}^{eff} = \frac{\tau}{\varepsilon_{GDL}} W_{GDL} \tag{3.25}$$

The effective thickness accounts for the actual thickness of the GDL (W_{GDL}), as well as its tortuosity factor (τ) and porosity (ε_{GDL}). Thus, for a given temperature and

current density, increasing the effective thickness causes the relative humidity at the catalyst layer to rise. There are two main approaches to increasing the effective thickness. The first approach is use a thicker GDL with the same porous structure. However, this increases the volume of the MEA, an undesirable result. The second approach is to fabricate a denser GDL featuring a lower porosity and likely a higher tortuosity factor. For reference, the effective thickness of a 200 μm thick carbon paper ($\varepsilon_{GDL} = 0.8$ and $\tau = 2.5$) is 0.625 mm.

Figure 3.22 presents the polarization curves for four different effective GDL thicknesses. It is evident in the polarization curves that the effective thickness of the GDL significantly influences performance. With each interval of increased effective GDL thickness there was dramatic improvement in performance. This is also evident in the power density curves presented in Figure 3.23.

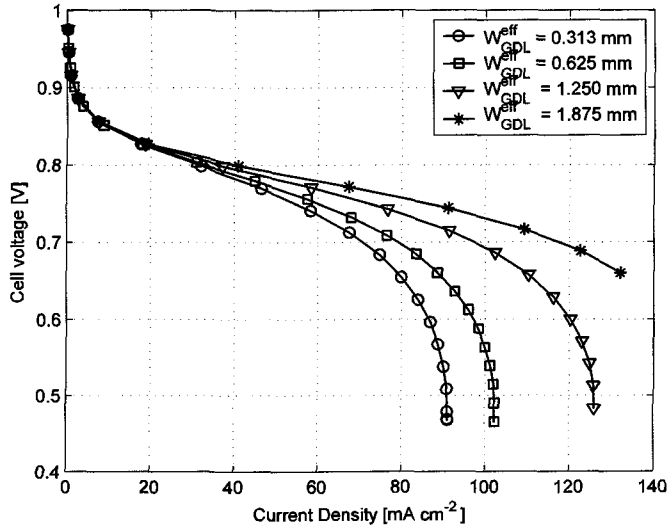

Figure 3.22: Polarization curves for a range of effective thicknesses of the cathode gas diffusion layer.

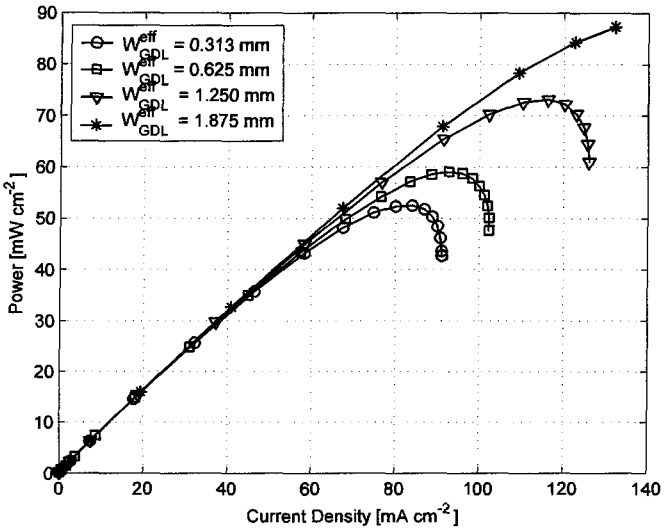

Figure 3.23: Power density curves for a range of effective thicknesses of the cathode gas diffusion layer.

Figure 3.24 presents the influence of the effective GDL thickness on the current density at a cell voltage of 0.7 V. The total increase of effective thickness from 0.313 mm 1.875 mm resulted in a 65% increase in current density. The approximately linear effect of the effective GDL thickness is evident. It is important to note that, although the increased effective thickness of the GDL restricts oxygen diffusion to the catalyst layer, the oxygen mass fraction at the catalyst layer is above 90% of the ambient for all thicknesses and current densities. This is in agreement with the work of Berning *et al.* [41] who considered a GDL with an effective thickness of 1.038 mm. At 200 mA cm^{-2}, they found that at the centre of the channel, next to the oxidant inlet, the oxygen concentration adjacent to the catalyst layer was only 8% below that of the channel concentration. In addition, increasing the thickness of the gas diffusion layer is not likely to introduce significant polarization because of the low current densities.

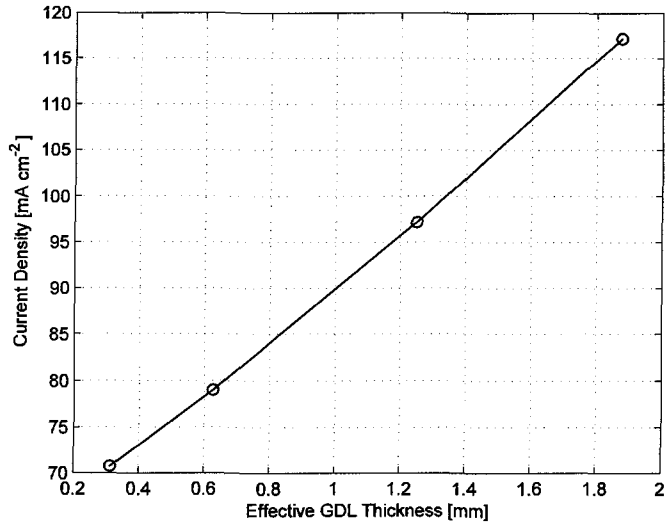

Figure 3.24: Effect of the effective thickness of the cathode gas diffusion layer on the current density at a cell voltage of 0.7 V.

Increasing the effective GDL thickness within reasonable limits improves performance through better membrane humidification and does not adversely effect the oxygen concentration; thus, an effort should be made to employ GDLs with a high effective thickness. To conserve volume, the effective thickness of the cathode GDL should be increased by reducing the porosity rather than increasing actual thickness. This can be achieved by using carbon powder to reduce the void space; or a woven carbon cloth could be used because it is typically denser and slightly thicker than carbon paper [64].

3.3.9 Platinum loading

The platinum catalyst used in PEM fuel cells represents a significant material cost; thus, the amount of platinum should be minimized. Consequently, a major objective when formulating catalyst layers is to reduce platinum loading without seriously impeding performance [72]. By employing the correlations of the variable-width macrohomogeneous model presented in Section 2.2.3 a parametric study of platinum loading was conducted. Platinum loadings of 0.05 mgPt cm^{-2}, 0.10 mgPt cm^{-2}, 0.25 mgPt cm^{-2}, and 0.50 mgPt cm^{-2} were considered in this study. Figure 3.25 depicts the polarization curves for these four platinum loadings.

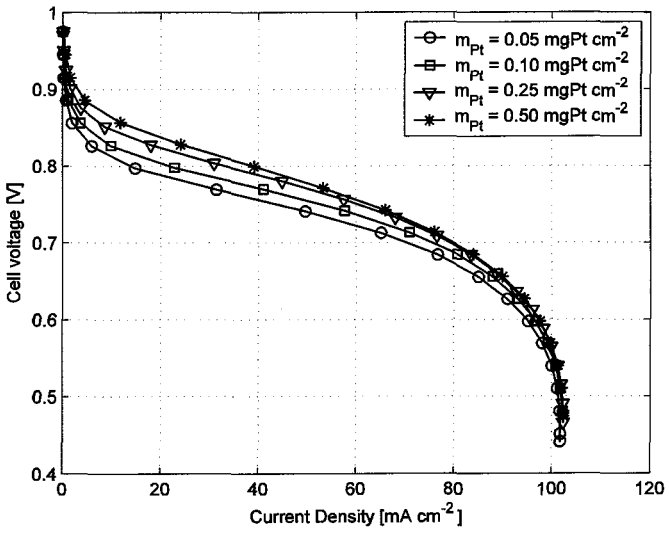

Figure 3.25: Polarization curves for a range of platinum loadings in the cathode catalyst layer.

As depicted by Figure 3.25, the effect of platinum loading is apparent at low current densities. The predominantly low-current density effect is due to the increased platinum surface area of the catalyst layer; it reduces the overpotential necessary for a

given current density. However, the limiting current does not significantly change because it is a result of membrane dry-out. In addition, Figure 3.26 illustrates that the variation in platinum loading studied does not significantly alter the power density curves.

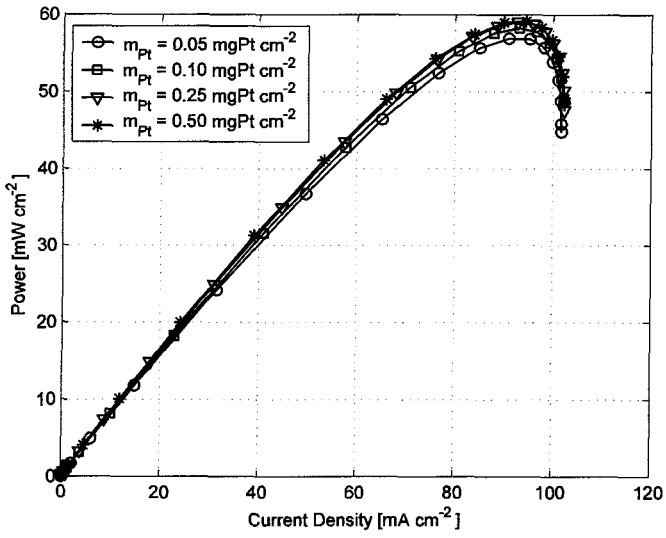

Figure 3.26: Power density curves for a range of platinum loadings in the cathode catalyst layer.

Figure 3.27 presents the effect that platinum loading has on the current density at a cell voltage of 0.7 V. This plot demonstrates that the current density rises steadily as additional platinum is first introduced and has a diminishing effect. This trend was also experimentally identified by Paganin *et al.* [73], Song *et al.* [74], and Qi and Kaufman [72]. Based on Figure 3.27, the optimum platinum loading is approximately 0.25 mgPt cm^{-2} (based on the diminishing returns beyond this value). This optimum value is in good agreement with that found by Qi and Kaufman [72].

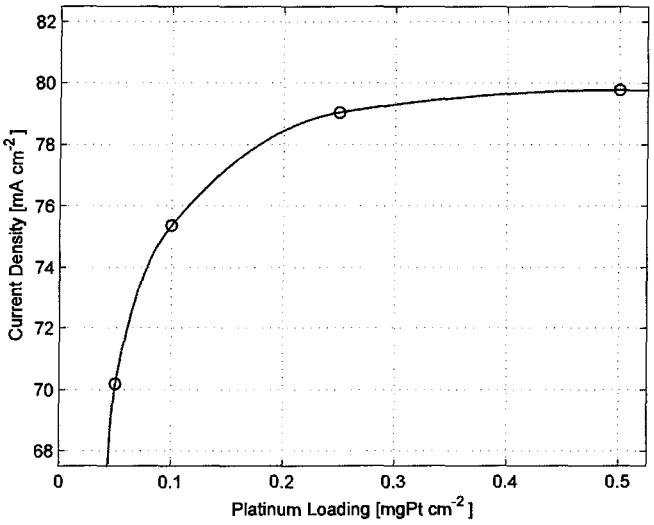

Figure 3.27: Effect of platinum loading in the cathode catalyst layer on the current density at a cell voltage of 0.7 V.

3.3.10 Nafion content

Nafion ionomer is a critical component of the catalyst layer because it facilitates the conduction of protons to regions of the catalyst layer not directly adjacent to the membrane. The Nafion content of the catalyst layer has an optimum value with respect to performance [3]. Too little Nafion raises the ionic resistance of the catalyst layer, causing the reaction zone to shift towards the membrane and reducing platinum utilization due to low Nafion coverage of the platinum. Similarly, if the Nafion content is too high, it reduces the ability of reactants to diffuse through the entire catalyst layer. In addition, too much Nafion diminishes the connectivity of the carbon/platinum matrix that conducts electricity, deteriorating platinum utilization. Ionic resistance is a major component of the fuel cell polarization for ambient air-

breathing fuel cells; thus, the effect of Nafion content on the ionic resistance of the catalyst layer is significant. A parametric study of Nafion content was conducted for Nafion contents of 20 % wt., 33 % wt., 45 % wt., and 60 % wt. Figure 3.28 presents polarization curves for these four Nafion contents.

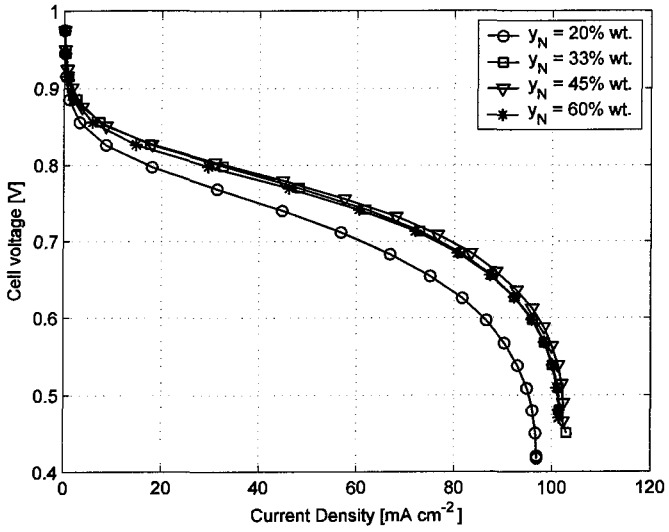

Figure 3.28: Polarization curves for a range of Nafion contents in the cathode catalyst layer.

The polarization curve for a Nafion content of 20 % wt. presents a significant drop in platinum utilization and ionic conductivity in the cathode catalyst layer. The reduced platinum utilization for this low Nafion content presents itself in the reduced voltage at low current densities. Moreover, the reduced ionic conductivity in the catalyst layer is evident in the earlier onset of the membrane dry-out. Nevertheless, for Nafion contents between 33 % wt. and 60 % wt., there is little difference in performance. The effect of Nafion content on performance is also evident in the power density curves in Figure 3.29.

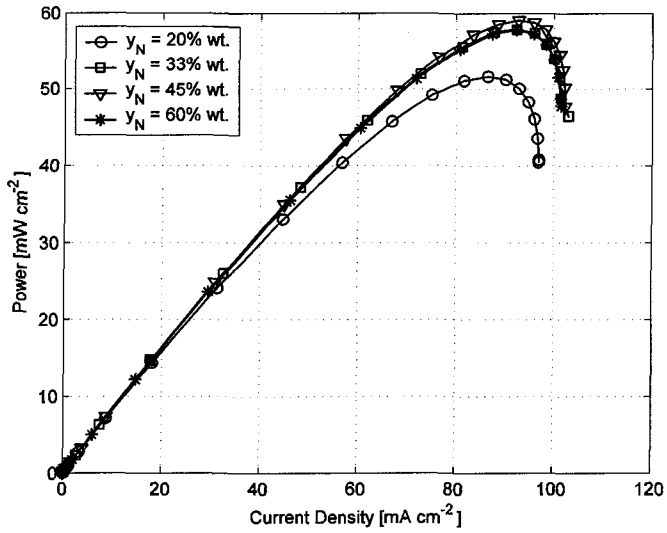

Figure 3.29: Power density curves for a range of Nafion contents in the cathode catalyst layer.

Figure 3.30 depicts the influence of Nafion content on current density at a cell voltage of 0.7 V. The plots shows that there is a dramatic performance drop when the Nafion content is reduced beyond 33 % wt. In contrast to a majority of experimental studies of thin-film electrodes that show an optimum Nafion content of 33 % wt. [72, 73], the plot in Figure 3.30 shows that optimum Nafion content is roughly 45 % wt. This difference is expected because those experimental studies were conducted at higher current densities for which mass transport issues are more dominant. Increased Nafion content reduces the effective diffusivity of the catalyst layer. In addition, the current density at 33 % wt. is only slightly less than that for 40 % wt., putting this result in close agreement with experimental observations.

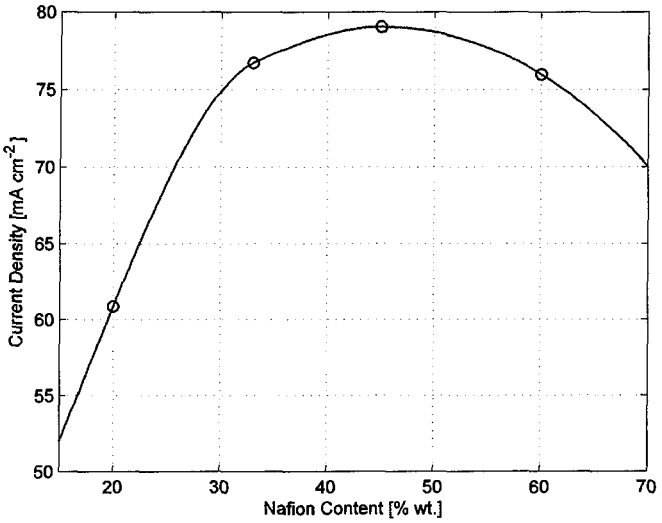

Figure 3.30: Effect of Nafion content in the cathode catalyst layer on the current density at a cell voltage of 0.7 V.

3.4 Summary

In this chapter, the 1-D analytical MEA model introduced in Chapter 2 was expanded to include the transport phenomena associated with planar air-breathing fuel cells to be implemented in device integrated formats. The additional transport phenomena include the transport of oxygen and water vapor between the fuel cell and ambient air, the diffusion of oxygen and water vapor within the cathode, and heat transfer from the fuel cell to the ambient air. The model was shown to agree well with experimental results for these particular fuel cells. The model's improved membrane conductivity correlation helped to provide evidence that membrane dry-out is problematic for air-breathing fuel cells that run on dry hydrogen. In addition, a comprehensive parametric study of operating conditions and design specifications elucidated their

relative impact on performance. In summary, the results indicate that maintaining a reasonable relative humidity within the fuel cell's membrane is a key objective when designing ambient air-breathing fuel cells for portable devices.

Chapter 4

Microstructured fuel cells

4.1 Introduction

The microstructured fuel cell presents a novel approach to the miniaturization of PEM fuel cells capable of dramatically increasing the volumetric power density by adopting a non-planar architecture. Traditional PEM fuel cells have adopted planar designs consisting of approximately two-dimensional consecutive layers. The non-planar architecture features an "on-end" arrangement of the electrodes. "On-end" refers to the fact that the microstructure fuel cell can be visualized as a segment of planar membrane electrode assembly placed on its end.

Figure 4.1 illustrates the architecture of the non-planar microstructured fuel cell. With the exception of the bipolar plates, this fuel cell contains the same components as traditional planar PEMFCs. The electrically-conductive separator takes on the role of the bipolar plate by collecting current and separating the oxidant and fuel stream. In addition, the caps on the bottom and top surfaces segregate the oxidant and fuel streams. As shown in Figure 4.1, reactant and product gases diffuse through the GDL

parallel to the catalyst layer. In contrast, the gases diffuse through the GDL in a perpendicular manner in the planar architecture. However, the ionic and electrical current still travels perpendicular to the membrane.

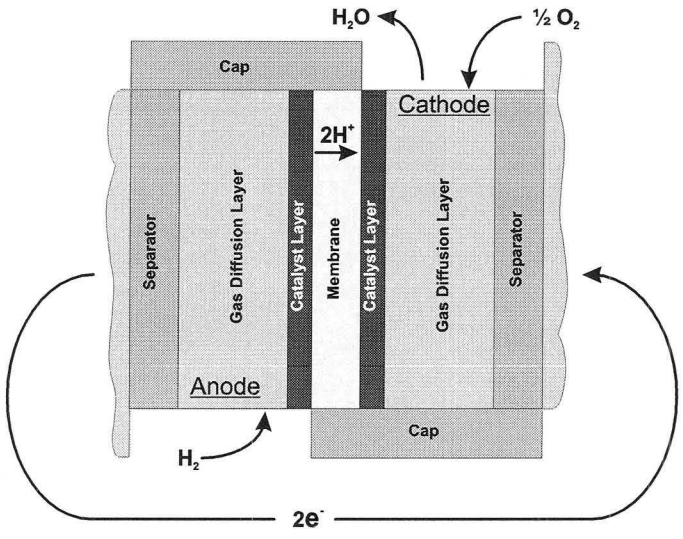

Figure 4.1: Schematic of the unit cell for the non-planar microstructured fuel cell.

Figure 4.2 illustrates the implementation of the microstructured architecture in an air-breathing device integrated fuel cell. Most features of this fuel cell system are the same as those described for the planar architecture (see Section 3.1). As the schematic shows, a fuel cell stack forms by stacking microstructured cells at adjacent separators. Forming a fuel cell stack allows the microstructured fuel cell system to achieve greater voltages than the planar architecture.

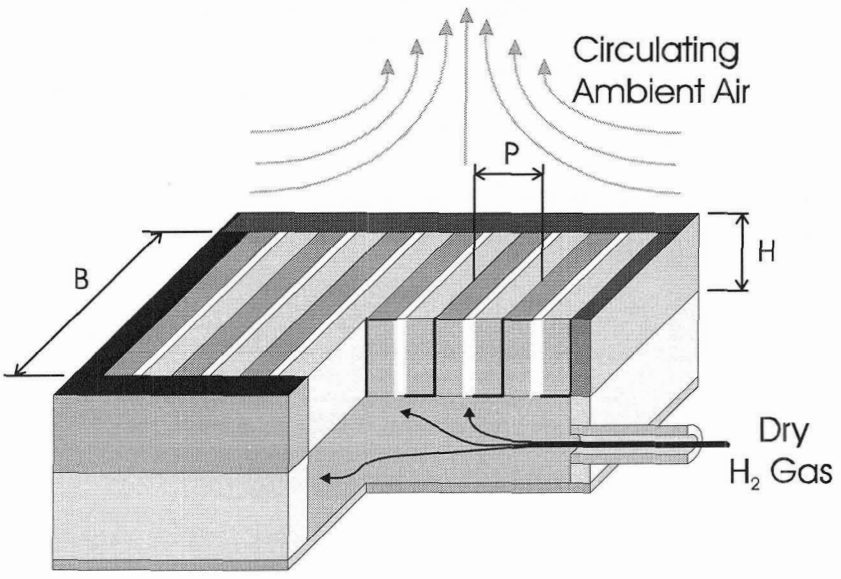

Figure 4.2: Schematic of the non-planar microstructured device integrated fuel cell.

The non-planar architecture has an intrinsic ability to achieve greater maximum power densities than its planar counterpart. The increase in power density is achieved through the ratio of active area to planar area, which can be greater than 1 for the microstructured fuel cell. For planar fuel cells, however, this ratio is constrained to 1. For microstructured fuel cells, this ratio increases as the pitch (P in Figure 4.2) is reduced. Therefore, if the fuel cell's current density is based on the planar area, the current density of the fuel cell can be greater than the average current density over the active area.

4.2 Model

In order to model the microstructured fuel cell, the analytical MEA model from Chapter 2 is expanded in a similar manner as in Chapter 3 for planar fuel cells. Mass transfer is modelled in the "on-end" cathode to elucidate its influence on oxygen concentration and relative humidity. A two-dimensional analytical expression for the distribution of gas species calculates the oxygen concentration and relative humidity at the MEA's interface with the GDL. The species flux at the MEA boundary condition is resolved by solving the analytical MEA model at discrete locations along the cathode's MEA/GDL interface. In this work, the mass transfer on the anode side of MEA is neglected using the same assumptions listed in Section 3.2.1 for the planar fuel cell model. It is assumed that there is negligible in-plane transport of mass and ions inside the membrane or catalyst layer. Heat transfer is modelled with the lumped-body formulation. Figure 4.3 presents a schematic of this semi-analytical model.

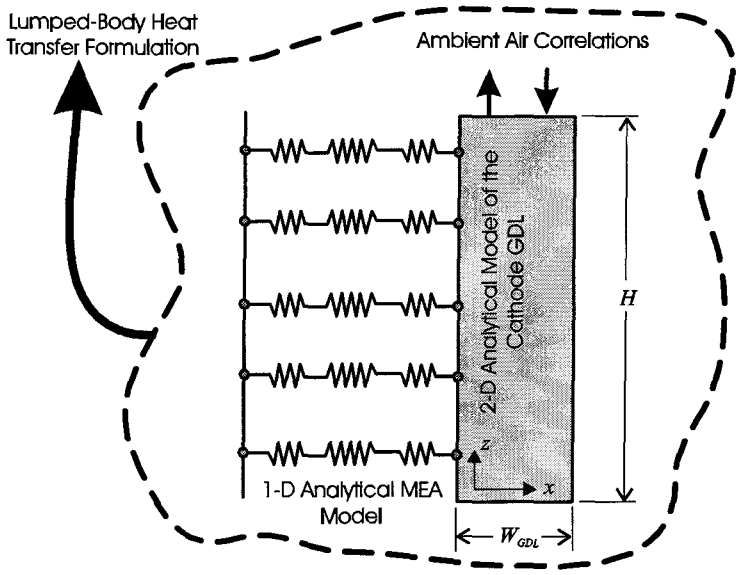

Figure 4.3: Schematic for the semi-analytical model of the non-planar microstructured fuel cell.

4.2.1 Gas diffusion layer

Solving for the oxygen and water vapour mass fraction distributions in two dimensions provides the following expressions:

$$y_{O2}(x,z) = \frac{M_{O2}}{4FW\rho D_{O2}^{eff}} \left[\int_0^z \int_0^z i(z)\,dzdz - \int_0^H \int_0^z i(z)\,dzdz + \ldots \right. \\ \left. i(z)\left(W_{GDL}x - \frac{x^2}{2} - \frac{3W_{GDL}^2}{8} \right) \right] + y_{O2}^o \qquad (4.1)$$

$$y_{H2O}(x,z) = -\frac{M_{H2O}}{2FW\rho D_{H2O}^{eff}} \left[\int_0^z \int_0^z i(z)\,dzdz - \int_0^H \int_0^z i(z)\,dzdz + \ldots \right. \\ \left. i(z)\left(W_{GDL}x - \frac{x^2}{2} - \frac{3W_{GDL}^2}{8} \right) \right] + y_{H2O}^o \qquad (4.2)$$

where H is the height of the GDL cavity and W_{GDL} is the GDL width. y_{O2}^{o} and y_{H2O}^{o} are the mass fractions at the interface of the GDL with the ambient air (evaluated with Eqns. (3.6) and (3.7)). The derivation of Eqns. (4.1) and (4.2) is given in Appendix B. The assumptions associated with this analytical approach were validated by using this formulation to approximate the oxygen distribution that was calculated by Litster *et al.* [10] using CFD. Figure 4.4 compares the numerical and analytical results; they agree reasonably well. The upper left corner of the GDL features the largest disagreement, but Figure 4.4 c) shows that the percent error is within 10%. This chapter will show that the lower left region, where the accuracy is better, has a significantly greater impact on performance.

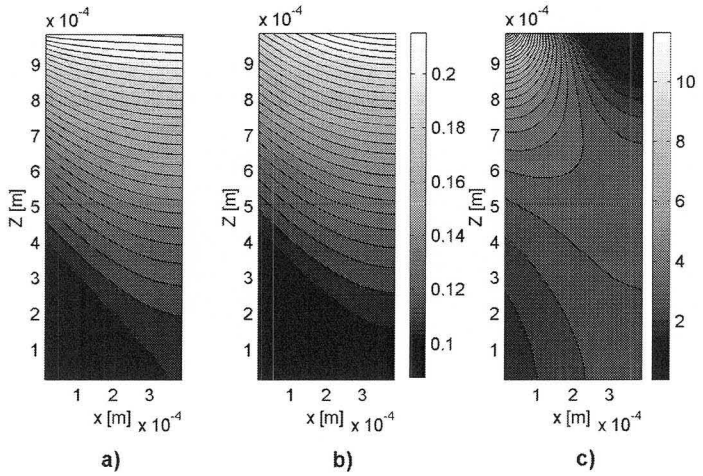

Figure 4.4: Comparison of a) numerical results [10] with the prediction of the b) analytical approximation, including the c) local percent difference.

4.2.2 Solution procedure

The solution strategy consists of discretizing the MEA (not including the GDL) along the z-axis and solving the MEA analytically along the x-axis. Thus, a profile of the current density at the catalyst layer/ GDL interface can be calculated. This profile is then employed in the two-dimensional analytical model of the gas transport within the GDL.

For a given temperature, the solution algorithm solves the current density at each discretization point i along the MEA. At each of these locations, the oxygen concentration and relative humidity at the GDL/catalyst layer interface of the cathode determine that location's exchange current density and electrolyte conductivity, respectively. The oxygen and water vapour mass fractions are solved with the analytical mass transfer formulations. This process is repeated until convergence is achieved for the given temperature. The temperature is solved using the same procedure discussed in Section 3.2.6.

The current boundary condition for the gas diffusion model is determined by fitting the MEA current distribution to a 3rd order polynomial, as shown in Eqn. (4.3). The form of the polynomial is constant and only the coefficients (a_n) vary. Thus, approximations of the integrals and double integrals are obtainable (Eqns. (4.4) and (4.5)). The integrations are facilitated in the given system because the constants of

integration are zero. In the solution algorithm, the polynomial integrals and the calculated polynomial coefficients are inserted into the integrals found in Eqn. (26). The polynomial fitting is conducted using a least-squares method.

$$i_i(z_i) \xrightarrow{polyfit} \sum_{n=1}^{3} a_n z^n \approx i(z) \tag{4.3}$$

$$\int_0^z \sum_{n=1}^{3} a_n z^n dz = \sum_{n=1}^{3} \frac{a_n}{n+1} z^{n+1} \approx \int_0^z i(z)dz \tag{4.4}$$

$$\int_0^z \int_0^z \sum_{n=1}^{3} a_n z^n dzdz = \sum_{n=1}^{3} \frac{a_n}{n+2} z^{n+2} \approx \int_0^z \int_0^z i(z)dzdz \tag{4.5}$$

4.3 Results and discussion

A parametric study of the cathode GDL width (W_{GDL}) in the microstructured fuel cell was undertaken to elucidate its effect on performance. The planar area of the microstructured fuel cell is constrained to 1 cm^2. The height of the microstructured fuel cell (H) is specified as 600 μm. This height is selected because it corresponds to the equivalent height of the planar fuel cell studied in Chapter 3. This similarity allows for a performance comparison of fuel cells occupying the same volume. The number of unit cells stacked in series is prescribed in order to achieve a fuel cell width (B in Figure 4.2) of roughly 1 cm. Herein, gas diffusion layer thicknesses of 50, 100, 150, 200, and 230 μm are studied. The case of a 230 μm thick GDL corresponds to a ratio of active area to planar surface area ($A_A A_S^{-1}$) of 1, which is

equal to that ratio for planar fuel cells. All other thicknesses considered produce ratio of areas greater than 1. Table 4.1 presents the effect of the GDL width on the area ratio and other geometrical parameters of the microstructured fuel cell. All other physical parameters are the same as those used in Chapter 3 for the study of planar fuel cells (Section 3.3.1).

Table 4.1: Effect of the gas diffusion layer width on the geometric properties of the microstructured fuel cell stack with a height of 600 μm, a 50 μm wide membrane, 20 μm wide catalyst layers, 50 μm wide separators, and a surface area of 1.00 cm^2.

Property	Gas Diffusion Layer Width, W_{GDL} [μm]				
	50	100	150	200	230
Cell pitch, P [μm]	240	340	440	540	600
Number of cells [-]	42	29	23	19	16
Width of cell, B [cm]	0.992	1.014	0.988	0.975	1.042
$A_A A_S^{-1}$ [-]	2.500	1.765	1.364	1.111	1.000

4.3.1 Active area polarization curves

Figure 4.5 presents polarization curves with current densities based on the active area for the microstructured fuel cell with four different GDL widths. The plot also presents the polarization curve of the planar fuel cell using the base-line parameters. The most notable information in this figure is extracted by comparing the planar fuel cell's polarization curve with that of a microstructured fuel cell with a GDL width of 230 μm. Both of these cases feature a ratio of active area to planar surface area of 1. The current density is considerably higher in the microstructured fuel cell even when the ratio of areas is equal. However, as this ratio increases with thinner GDLs the

performance of the microstructured fuel cell decreases (based on active area). The microstructured fuel cell with a 100 μm wide GDL performs worse than the planar fuel cell (when compared on an active area basis).

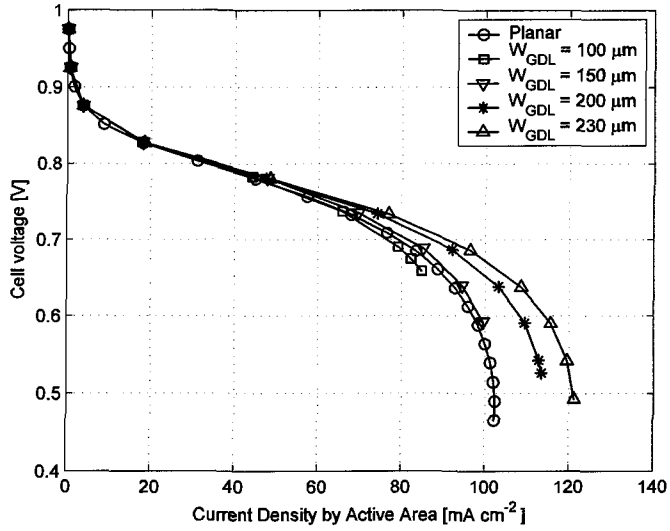

Figure 4.5: Polarization curves based on the electrochemically active area.

The increase in performance with the introduction of the microstructured fuel cell and the decrease in performance as the GDL width is reduced are the results of two competing phenomena: increased diffusion resistance and greater volumetric heating. The performance increases with the introduction of the non-planar architecture because the vapour diffuses through the entire height of the fuel cell (roughly three times greater than the width of the planar GDL). This longer diffusion length increases humidity at the bottom of the microstructured fuel cell and therefore the ionic conductivity at the bottom of the fuel cell is relatively high. The performance decreases as the GDL width is reduced because this increases the ratio of active area

to volume, which corresponds to higher heating per unit volume of fuel cell. The increased volumetric heating accelerates membrane dry-out.

4.3.2 Relative humidity

Figure 4.6 depicts how the microstructured architecture and width of the GDL influence relative humidity in the cathode. Each plot is shown for a cell voltage of 0.7 V. The relative humidity distribution contours demonstrate increased relative humidity at the bottom of the GDL ($z = 0$) and decreased relative humidity at the top of the GDL ($z = 600$ μm). The lower relative humidity indicates membrane dry-out in upper regions of the fuel cell. The higher relative humidity at the bottom of GDL is intensified by increased water production due to higher current densities (the result of a lower membrane resistance). This feedback is moderated by increased heat production that effectively reduces relative humidity.

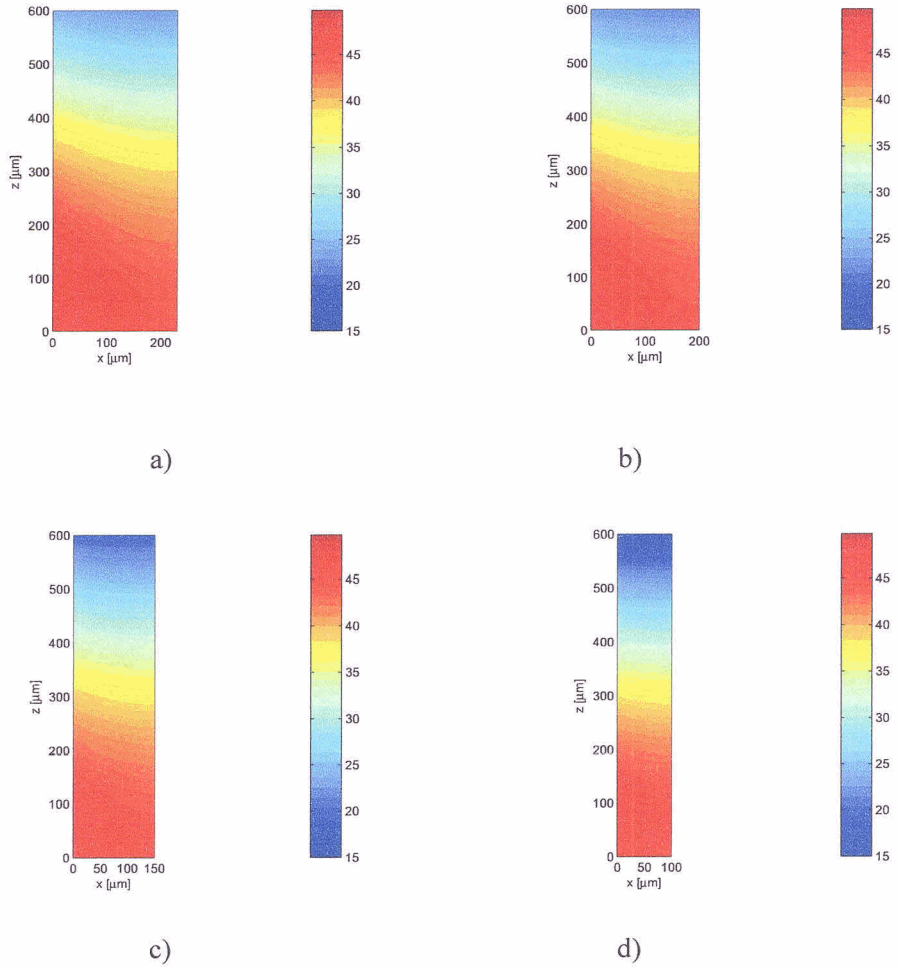

Figure 4.6: Relative humidity [%] distribution in the cathode gas diffusion layer at a cell voltage of 0.7 V. a) $W_{GDL} = 230$ µm; b) $W_{GDL} = 200$ µm; c) $W_{GDL} = 150$ µm; d) $W_{GDL} = 100$ µm.

4.3.3 Membrane conductivity

Figure 4.7 presents the influence that the relative humidity distributions (shown in Figure 4.6) have on the ionic conductivity of the membrane. For all GDL widths, the membrane conductivity profile is relatively constant (only the magnitude of the conductivity changes). As expected from observing the relative humidity distribution, the conductivities are dramatically higher at the bottom of the fuel cell than they are at the top. The difference is roughly one order of magnitude.

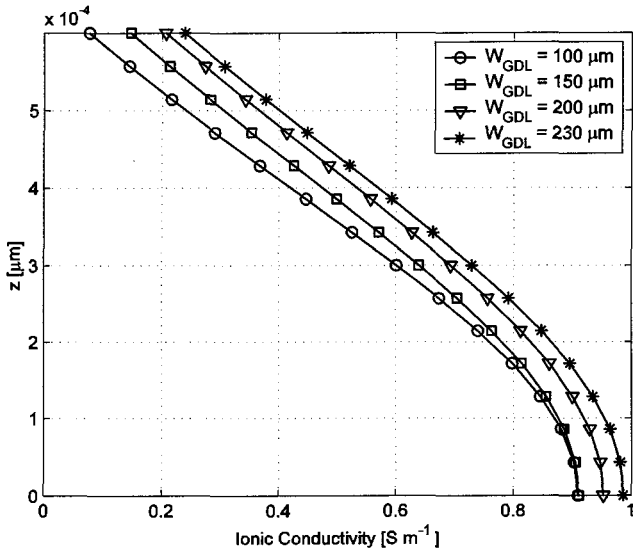

Figure 4.7: Vertical profile of the membrane's ionic conductivity.

As the GDL width varies, the relative magnitude of change in local conductivity varies with the vertical position in the membrane. The width of the GDL has a more significant impact at the top of the fuel cell where performance-quenching membrane dry-out occurs. The drop in conductivity at the top of cell is approximately double that at the bottom. It is also interesting to note that the conductivity no longer reduces at the bottom of the fuel cell when GDL width drops below a value of 150 μm.

4.3.4 Oxygen distribution

Figure 4.8 presents the contours of the oxygen mass fraction for the four GDL widths in the microstructured fuel cell. The oxygen contours illustrate a decrease in the oxygen mass fraction towards the bottom of the GDL. In addition, the width of the GDL affects the oxygen mass fraction. The oxygen mass fraction at the bottom of the 100 μm wide GDL is roughly half that of the 230 μm wide GDL. However, the magnitude of oxygen depletion is insignificant from a performance viewpoint. For all of the operating points plotted in the polarization curves of Figure 4.5, the minimum oxygen concentration in the GDL is 92% of the ambient mass fraction or higher. Therefore, the ohmic resistance and the cathode reaction's activation dictate the performance of the microstructured fuel cell (same as the planar fuel cell).

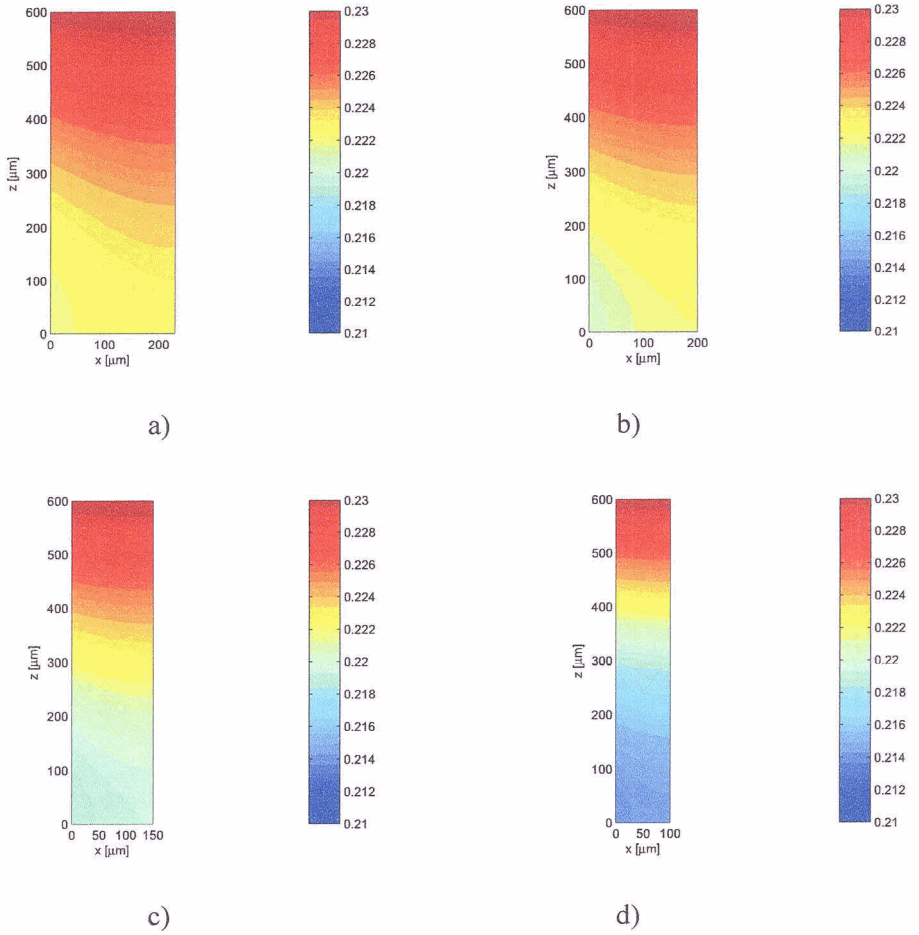

Figure 4.8: Oxygen mass fraction (y_{O2}) [-] distribution in the cathode gas diffusion layer at a cell voltage of 0.7 V. a) $W_{GDL} = 230$ µm; b) $W_{GDL} = 200$ µm; c) $W_{GDL} = 150$ µm; d) $W_{GDL} = 100$ µm.

4.3.5 Local polarization curves

Figure 4.9 presents the local polarization curves along the vertical height of the MEA. There is a distinct change in the polarization curve along the vertical height. This current distribution is generated by the variation in membrane conductivity shown in Figure 4.7. The current density is roughly uniform down to a cell voltage of 0.8 V. At lower cell voltages, the current density at the bottom of the GDL can be several times greater than that at the top.

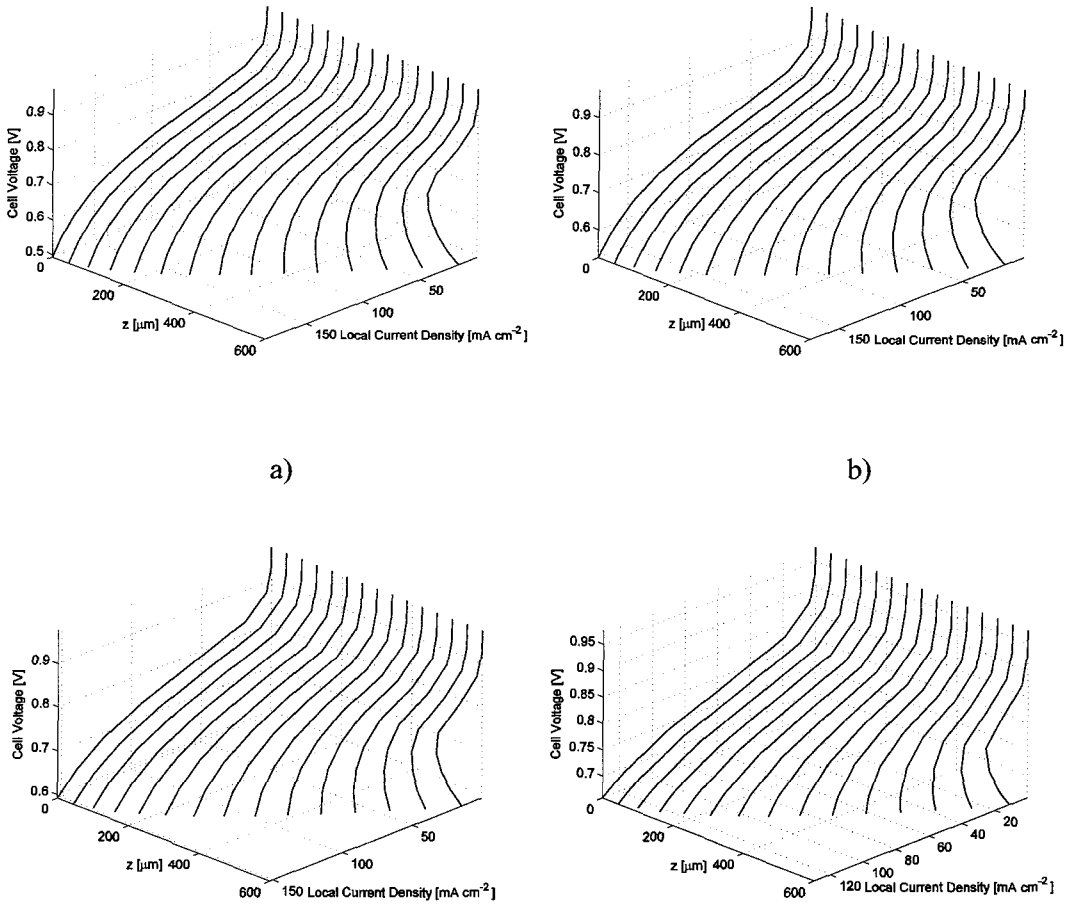

Figure 4.9: Local polarization curves for a) $W_{GDL} = 230$ μm; b) $W_{GDL} = 200$ μm; c) $W_{GDL} = 150$ μm; d) $W_{GDL} = 100$ μm.

A notable feature of the local polarization curves at the top of the GDL during low cell voltages is the reduction in current density as the cell voltage is further decreased. Similar bent back local polarization curves have been observed experimentally [75] and in computational simulations [50, 76] as a result of mass transfer limitations at the end of the oxidant channel due to the larger consumption of oxygen in the first portion of the channel. In this study, the bent back polarization curves are instead due to membrane dry-out because the humidified region at the bottom of the cell allows

for greater heat production that advances the membrane dry-out at the top of the fuel cell.

4.3.6 Planar area based performance

The polarization curves presented in Section 4.3.1 were plotted using the active area of the fuel cell, which is a good indicator of fuel cell performance. To make comparisons between fuel cells for portable devices, volume is critical. It is best to compare fuel cells by volumetric current density or by volumetric power density. However, because all the fuel cell configurations presented in this chapter feature the same thickness (~600 μm), comparisons are now made with the planar area instead of volume. Thus, the current densities and power densities presented in this section are based on the planar area, which is equal to the active area in the planar architecture.

Figure 4.10 presents the planar area polarization curves. The polarization curves indicate that the performance increases as the GDL width is reduced. This trend is the opposite of that found when comparing performance by active area; comparing by active area showed that performance diminished as the GDL width was decreased. That trend was the result of increased volumetric heating inducing membrane dry-out. However, when the surface area to active area ratio is employed the results show that the ratio of areas has a more substantial effect on performance than does volumetric heating. It should be noted that the polarization curves for the planar fuel cell and the microstructured fuel cell with a 230 μm wide GDL are unchanged from the active area representation because their ratio of active area to planar surface area is 1.

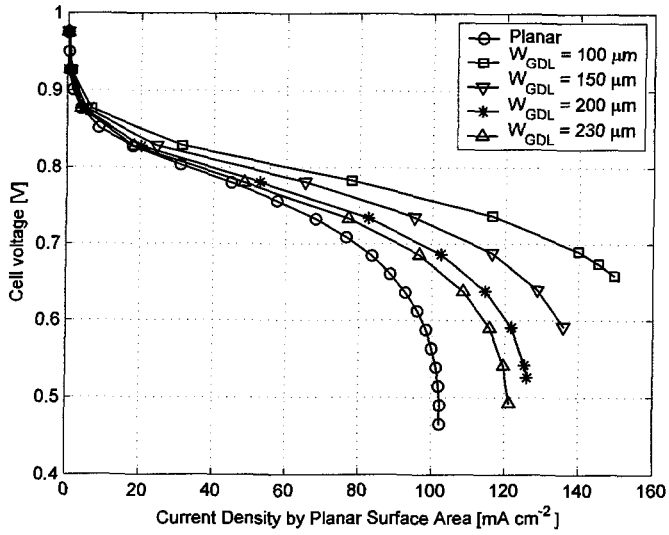

Figure 4.10: Polarization curves based on the planar surface area.

The polarization curves in Figure 4.10 demonstrate that reducing the GDL width dramatically improves fuel cell performance. Moreover, the rate of increase in performance also grows with GDL width reduction. Continual thinning of the GDL would face a number of issues including manufacturability, liquid water flooding, and oxygen starvation. It should be noted that the maximum current density achievable when using the 100 μm wide GDL is greater than that found with the thickest GDL studied during the analysis of gas diffusion layer thickness in planar fuel cells (Section 3.3.8). For that particular planar case, the fuel cell volume would be greater due to the thicker GDL.

Another feature of the microstructured fuel cell that makes it well suited to portable devices is the improved efficiency (ratio of the cell voltage to the reversible voltage) for all current densities. Efficiency is critical in portable devices because of the volume dedicated to carrying fuel. At higher efficiencies, a larger portion of the

stored fuel goes to producing electricity rather than heat. Higher efficiency at low current densities is difficult to achieve in the planar configuration and is typically only achieved by reducing activation losses with higher platinum loadings (see Section 3.3.9).

Figure 4.11 illustrates power density curves based on the planar area for the four configurations of the microstructured fuel cell and the planar fuel cell. These plots demonstrate notable increases in maximum power densities with the introduction of the microstructured architecture and thinner GDLs. The figure shows that the maximum power density can increase from 59 mW cm^{-2} for the planar fuel cell to as high as 100 mW cm^{-2} for the microstructured fuel cell.

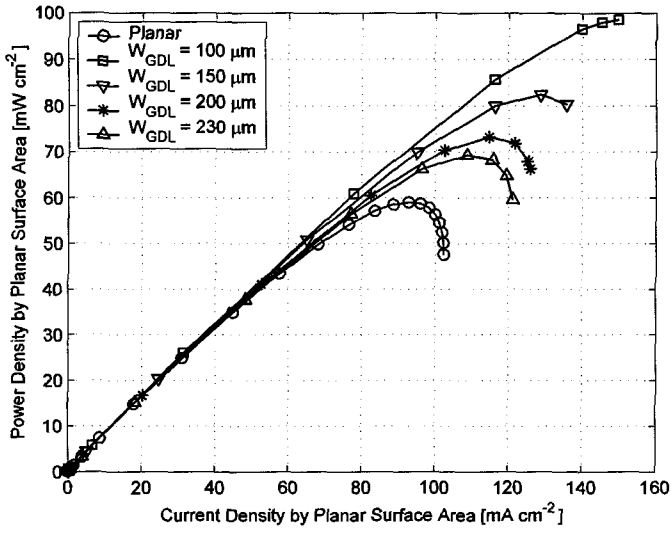

Figure 4.11: Power density curves based on the planar surface area.

Figure 4.12 presents the fuel cell temperature for the five fuel cells with respect to planar power density. The figure illustrates how the depth of the microstructured fuel cell's GDL, which effectively insulates humidity, allows for the microstructured fuel

cell to operate at higher temperatures than the planar fuel cell. The figure shows that the temperature associated with the rate limiting current density is 3-4 K higher for the microstructured fuel cell. More importantly, these plots demonstrate that if fuel cell temperature is a concern, and if it should be minimized, then the microstructured architecture should be employed. When microstructured fuel cells are operated at the same power density as the planar fuel cell's maximum power density, the temperature of a microstructured fuel cell is 4-7 K lower.

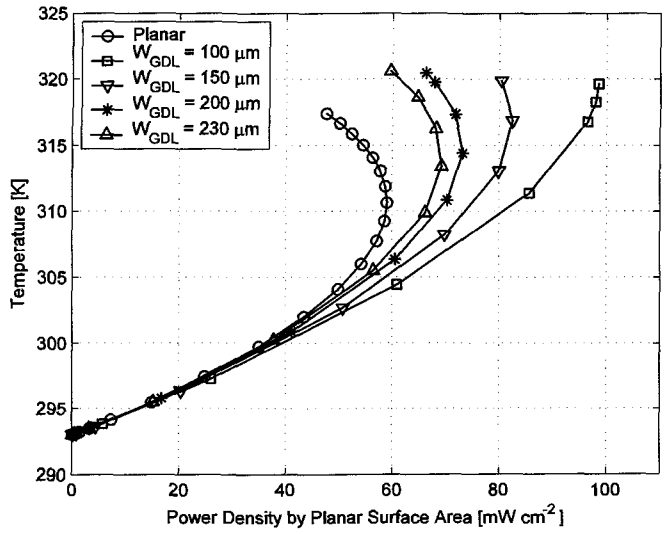

Figure 4.12: Temperature versus power density based planar surface area.

Figure 4.13 presents plots of the maximum relative humidity in the GDL with respect to temperature. The temperature can be correlated to the power density via the previous figure. These plots of relative humidity show the insulation of relative humidity by the aspect ratio and depth of the microstructured fuel cell's GDL. It is evident that the relative humidity in the planar fuel cell drops almost linearly with temperature because it does not retain enough product water vapour. However, the

microstructured fuel cell features an initial rise in the relative humidity. This represents a form of auto-humidification. The region of increased relative humidity and a resulting higher efficiency occurs at relatively low current and power densities. The plot also shows that the microstructured fuel cell is more capable of self-humidifying as the GDL width is reduced.

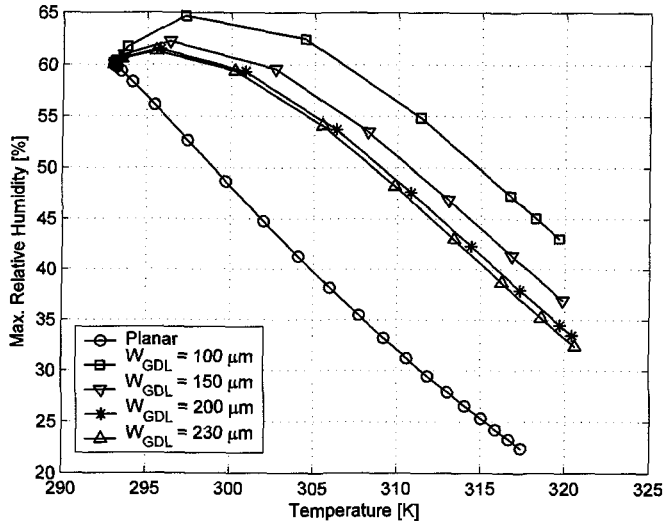

Figure 4.13: Maximum relative humidity versus temperature.

4.4 Summary

This chapter introduced a two-dimensional model of a microstructured fuel cell featuring an "on-end" electrode arrangement. A two-dimensional analytical expression was derived to model mass transport within the GDL and a solution algorithm was developed to interface the analytical one-dimensional MEA model

with the two-dimensional mass transfer model. The results clearly demonstrate the advantages of employing the non-planar architecture of the microstructured fuel cell. The most inherent benefit was the increased active area per unit volume, which allowed for greater maximum power densities and higher efficiencies. The second advantage addresses the humidification issues facing these fuel cells. The aspect ratio and depth of the microstructured fuel cell's GDL provided a means to entrap more water vapour in the MEA, improving performance and allowing the fuel cell to withstand higher temperatures.

Chapter 5

Conclusions, technical insights, and outlook

5.1 Conclusions

Fuel cells have the potential to supplant batteries in portable electronic devices because of increased cost tolerances for fuel cells at this scale, their rapid recharges, and their higher energy densities. This thesis presented one- and two-dimensional models of air-breathing fuel cells for portable devices. The models employed both analytical and semi-analytical approaches to resolve the transport of ions, heat and mass. The key component of the models is a 1-D analytical model of the membrane electrode assembly (MEA). Evidence was provided that the MEA model accurately predicts fuel cell performance through detailed accounting of catalyst layer specifications and electrochemical parameters via a variable-width macrohomogeneous formulation. The last major component of these fuel cell models is a lumped-body heat transfer formulation. The heat transfer model was employed to elucidate the coupling between the operating condition and temperature, as well as the overall effect of heat transfer on performance.

The thesis examined two fuel cell architectures; the first was a conventional planar architecture and the other was a microstructured non-planar architecture. A large-scale parametric study of the planar fuel cell was conducted to identify the trends associated with a variety of design specifications and operating conditions. Knowledge of these trends can supplement the design of fuel cells to be integrated into portable devices. Mass transfer models enabled the discovery of the dramatic impact that relative humidity can elicit on performance and that oxygen starvation does not arise in the conditions investigated. The parametric study elucidated the significant effect heat transfer has on membrane dry-out in ambient air-breathing fuel cells. The model demonstrated the high sensitivity of the fuel cell performance to temperature via the temperature dependence of the water vapour's saturation pressure. In addition, evidence of a limiting current density with respect to membrane dry-out was presented.

Notably, the inaccuracy of the Springer membrane conductivity correlation for low-humidity conditions was demonstrated by introducing an improved correlation. The Springer correlation was shown to over-predict the current density corresponding to membrane dry-out by roughly 100%. This finding revealed the inaccuracy of low-humidity fuel cell models featuring the Springer correlation.

The study of the non-planar microstructured fuel cell gave convincing evidence that significantly greater power densities and higher efficiencies can be obtained with that architecture. The non-planar architecture achieved these distinctions by increasing the amount of active area per unit volume. In addition, the "on-end" arrangement of the

microstructured electrodes provided a greater diffusion barrier to the water vapour, improving performance by increasing the membrane conductivity.

In summary, this thesis demonstrated that PEM fuel cells fueled with dry hydrogen can meet the power density requirements of portable devices such as mobile phones with video playback. The analysis also demonstrated that the elimination of many common ancillary systems is permissible. The objective power density of 60 mW cm^{-2} was demonstrated without the inclusion of dedicated systems for oxygen distribution, hydrogen conditioning, and heat management.

5.2 Technical insights

The following are some technical insights obtained in the course of this thesis with respect to fuel cells integrated into portable devices:

- These fuel cells can effectively operate in an ambient air-breathing mode and do not require auxiliary fans, compressors, or manifolding.

- Dry hydrogen is a viable fuel and does not require conditioning prior to entering the fuel cell.

- Emphasis during the design process should be placed on maximizing the heat transfer from the fuel cell while maintaining a passive cooling method. An example of this approach is the integration of high surface area heat sinks into the fuel cell system.

- The fuel cell system should be specified to operate in all reasonable environmental conditions. Variations in the ambient air's relative humidity can significantly impact performance.

- The gas diffusion layer should feature low-porosity or greater thickness to entrap more water vapour next to the membrane. However, increasing gas diffusion layer thickness deteriorates volumetric power density. Thus, the preference is to reduce gas diffusion layer porosity with carbon powder and other treatments.

- Platinum loadings greater than 0.25 mgPt cm^{-2} are not necessary when formulating thin-film catalyst layers for ambient air-breathing fuel cells. Higher platinum loadings do not significantly increase performance.

- The optimum Nafion content in ambient air-breathing fuel cells is greater than that for humidified PEM fuel cells. The higher Nafion content reduces the ionic resistance in the catalyst layer. It was found that a Nafion content of approximately 45 % wt. provided the best performance.

- Adopting a non-planar architecture in a microstructured fuel cell can greatly improve performance by increasing the active area per unit volume and maintaining humidity within the fuel cell.

- The volumetric performance of non-planar microstructured fuel cells can be heightened by reducing the width of the gas diffusion layer. Thinning of the

gas diffusion layers increases the active area per unit volume and allows the fuel cell to entrap more humidity.

5.3 Outlook

Although the assumptions employed in this thesis are justifiable, a number of them could be replaced with additional physics for improved resolution. The following are some plausible expansions of the model that maintain the objectives of this thesis:

- Resolve the mass transport on the anode side of the MEA and employ a membrane water transport model. The addition of these two components would allow an approximation of the water distribution across the membrane. In addition, this would enable an improved estimation of the ionic resistance.

- Numerical methods could improve the fidelity of the mass transfer models for the gas diffusion layer and the ambient air.

- Improvement of the correlations for the diffusion of oxygen in the catalyst layer. This improved resolution for oxygen was not shown as necessary in this analysis. However, if the analytical MEA model is to be implemented in the modelling of larger fuel cells, it would become necessary to further validate this component of the model.

- Obtain a more specific definition for the heat transfer coefficient. An improved definition could be achieved through both experimental and numerical characterization of the heat transfer from device integrated fuel cells.

References

[1] C. K. Dyer, "Fuel cells for portable applications," *Journal of Power Sources*, vol. 106, pp. 31-34, 2002.

[2] H. Kariatsumari and H. Yomogita, "Mobile Phones Drive Fuel Cell Development," *Nikkei Electronics Asia*, February 2005.

[3] S. Litster and G. McLean, "PEM fuel cell electrodes," *Journal of Power Sources*, vol. 130, pp. 61-76, 2003.

[4] D. Chu and R. Jiang, "Performance of polymer electrolyte membrane fuel cell (PEMFC) stacks Part I. Evaluation and simulation of an air-breathing PEMFC stack," *Journal of Power Sources*, vol. 83, pp. 128-133, 1999.

[5] R. Hahn, Wagner, S., Schmitz, A., Reichl, H., "Development of a planar micro fuel cell with thin film and micro patterning technologies," *Journal of Power Sources*, vol. 131, pp. 73-78, 2004.

[6] T. Hottinen, I. Himanen, and P. Lund, "Effect of cathode structure on planar free-breathing PEMFC," *Journal of Power Sources*, vol. 138, pp. 205-210, 2004.

[7] T. Hottinen, M. Mikkola, and P. Lund, "Evaluation of planar free-breathing polymer electrolyte membrane fuel cell design," *Journal of Power Sources*, vol. 129, pp. 68-72, 2004.

[8] T. Hottinen, M. Noponen, T. Mennola, O. Himanen, M. Mikkola, and P. Lund, "Effect of ambient conditions on performance and current distribution of a polymer electrolyte membrane fuel cell," *Journal of Applied Electrochemistry*, vol. 33, pp. 265-271, 2003.

[9] P. W. Li, T. Zhang, Q. M. Wang, L. Scharfer, and M. K. Chyu, "The performance of PEM fuel cells fed with oxygen through the free-convection mode," *Journal of Power Sources*, vol. 114, pp. 63-69, 2003.

[10] S. Litster, J. G. Pharoah, G. McLean, and N. Djilali, "Computational Analysis of Heat and Mass Transfer in a Micro-Structured PEMFC Cathode," *Journal of Power Sources, IN PRESS*, 2005.

[11] M. Noponen, T. Mennola, M. Mikkola, T. Hottinen, and P. Lund, "Measurement of current distribution in a free-breathing PEMFC," *Journal of Power Sources*, vol. 106, pp. 304-312, 2002.

[12] A. Schmitz, S. Wagner, R. Hahn, H. Uzun, and C. Hebling, "Stability of planar PEMFC in Printed Circuit Board technology," *Journal of Power Sources*, vol. 127, pp. 197-205, 2004.

[13] J. S. Wainright, R. F. Savinell, C. C. Liu, and M. Litt, "Microfabricated fuel cells," *Electrochimica Acta*, vol. 48, pp. 2869-2877, 2003.

[14] C. Ziegler, A. Schmitz, M. Tranitz, E. Fontes, and J. O. Schumacher, "Modeling Planar and Self-Breathing Fuel Cells for Use in Electronic Devices," *Journal of the Electrochemical Society*, vol. 151, pp. A2028-A2041, 2004.

[15] S. J. Lee, A. Chang-Chien, S. W. Cha, R. O'Hayre, Y. I. Park, Y. Saito, and F. B. Prinz, "Design and fabrication of a micro fuel cell array with "flip-flop" interconnection," *Journal of Power Sources*, vol. 112, pp. 410-418, 2002.

[16] G. McLean, N. Djilali, M. Whale, and T. Niet, "Application of Micro-scale Techniques to Fuel Cell Systems Design," *10th Canadian Hydrogen Conference,* 2000.

[17] W. R. Mérida, G. McLean, and N. Djilali, "Non-planar architecture for proton exchange membrane fuel cells," *Journal of Power Sources*, vol. 102, pp. 178-185, 2001.

[18] T. E. Springer, T. A. Zawodzinski, and S. Gottesfeld, "Polymer Electrolyte Fuel Cell Model," *Journal of the Electrochemical Society*, vol. 138, pp. 2334-2342, 1991.

[19] D. M. Bernardi and M. W. Verbrugge, "A Mathematical Model of the Solid-Polymer-Electrolyte Fuel Cell," *Journal of the Electrochemical Society*, vol. 139, pp. 2477-2491, 1992.

[20] T. F. Fuller and J. Newman, "Water and Thermal Management in Solid-Polymer-Electrolyte Fuel Cells," *Journal of the Electrochemical Society*, vol. 140, pp. 1218-1225, 1993.

[21] T. V. Nguyen and R. E. White, "A Water and Heat Management Model for Proton-Exchange-Membrane Fuel Cells," *Journal of the Electrochemical Society*, vol. 140, pp. 2178-2186, 1993.

[22] J. C. Amphlett, R. M. Baumert, B. A. Peppley, and P. R. Roberge, "Performance Modeling of the Ballard Mark IV Solid Polymer Electrolyte Fuel Cell I. Mechanistic Model Development," *Journal of the Electrochemical Society*, vol. 142, pp. 1-8, 1995.

[23] J. S. Yi and T. V. Nguyen, "An Along-the-Channel Model for Proton Exchange Membrane Fuel Cells," *Journal of the Electrochemical Society*, vol. 145, pp. 1149-1159, 1998.

[24] V. Gurau, F. Barbir, and H. Liu, "An Analytical Solution of a Half-Cell Model of PEM Fuel Cells," *Journal of the Electrochemical Society*, vol. 147, pp. 2468-2477, 2000.

[25] R. Bradean, K. Promislow, and B. Wetton, "Transport phenomena in the porous cathode of a proton exchange membrane fuel cell," *Numerical Heat Transfer, Part A*, vol. 42, pp. 121-138, 2002.

[26] P. Berg, K. Promislow, J. St. Pierre, and J. Stumper, "Water Management in PEM Fuel Cells," *Journal of the Electrochemical Society*, vol. 151, pp. A341-A353, 2004.

[27] A. A. Kulikovsky, "Semi-analytical 1D+1D model of a polymer electrolyte fuel cell," *Electrochemistry Communications*, vol. 6, pp. 969-977, 2004.

[28] T. Berning and N. Djilali, "Three-dimensional computational analysis of transport phenomena in a PEM fuel cell--a parametric study," *Journal of Power Sources*, vol. 124, pp. 440, 2003.

[29] D. Natarajan and T. V. Nguyen, "Three-dimensional effects of liquid water flooding in the cathode of a PEM fuel cell," *Journal of Power Sources*, vol. 115, pp. 66-80, 2003.

[30] P. T. Nguyen, T. Berning, and N. Djilali, "Computational model of a PEM fuel cell with serpentine gas flow channels," *Journal of Power Sources*, vol. 130, pp. 149, 2004.

[31] S. Shimpalee, S. Greenway, D. Spruckler, and J. W. Van Zee, "Predicting water and current distribution in a commercial-size PEMFC," *Journal of Power Sources*, vol. 135, pp. 79-87, 2004.

[32] B. Sivertsen and N. Djilali, "CFD Based Modelling of Proton Exchange Membrane Fuel Cells," *Journal of Power Sources*, vol. 141, pp. 65-78, 2005.

[33] S. Um and C. Y. Wang, "Three-dimensional analysis of transport and electrochemical reactions in polymer electrolyte fuel cells," *Journal of Power Sources*, vol. 125, pp. 40-51, 2004.

[34] L. Wang and H. Liu, "Performance studies of PEM fuel cells with interdigitated flow fields," *Journal of Power Sources*, vol. 134, pp. 185-196, 2004.

[35] G. F. McLean, "Apparatus of high power density fuel cell layer with micro for connecting to an external load," United States Patent 6864010, 2005.

[36] G. F. McLean, "Apparatus of high power density fuel cell layer with micro structured components," WO03067693, 2003.

[37] G. F. McLean, "Electrochemical cell," United States Patent 6872287, 2005.

[38] T. Mennola, M. Noponen, M. Aronniemi, T. Hottinen, M. Mikkola, O. Himanen, and P. Lund, "Mass transport in the cathode of a free-breathing polymer electrolyte membrane fuel cell," *Journal of Applied Electrochemistry*, vol. 33, pp. 979-987, 2003.

[39] T. Mennola, M. Noponen, T. Kallio, M. Mikkola, and T. Hottinen, "Water balance in a free-breathing polymer electrolyte membrane fuel cell," *Journal of Applied Electrochemistry*, vol. 34, pp. 31-36, 2004.

[40] Q. Wang, M. Eikerling, D. Song, Z. Liu, T. Navessin, Z. Xie, and S. Holdcroft, "Functionally graded cathode catalyst layers for polymer electrolyte fuel cells," *Journal of the Electrochemical Society*, vol. 151, pp. A950-A957, 2004.

[41] T. Berning, D. M. Lu, and N. Djilali, "Three-dimensional computational analysis of transport phenomena in a PEM fuel cell," *Journal of Power Sources*, vol. 106, pp. 284-294, 2002.

[42] A. Parthasarathy, S. Srinivasan, A. J. Appleby, and C. R. Martin, "Pressure-dependence of the oxygen reduction reaction at the platinum microelectrode nafion interface - Electrode-kinetics and mass-transport," *Journal of the Electrochemical Society*, vol. 139, pp. 2856-2862, 1992.

[43] C. Y. Du, P. F. Shi, X. Q. Cheng, and G. P. Yin, "Effective protonic and electronic conductivity of the catalyst layers in proton exchange membrane fuel cells," *Electrochemistry Communications*, vol. 6, pp. 435-440, 2004.

[44] M. Eikerling and A. A. Kornyshev, "Modelling the performance of the cathode catalyst layer of polymer electrolyte fuel cells," *Journal of Electroanalytical Chemistry*, vol. 453, pp. 89-106, 1998.

[45] M. L. Perry, J. Newman, and E. J. Cairns, "Mass Transport in Gas Diffusion Electrodes: A Diagnostic Tool for Fuel-Cell Cathodes," *Journal of the Electrochemical Society*, vol. 145, pp. 5-15, 1998.

[46] L. Pisani, M. Valentini, and G. Murgia, "Analytical pore scale modeling of the reactive regions of polymer electrolyte fuel cells," *Journal of the Electrochemical Society*, vol. 150, pp. A1549-A1559, 2003.

[47] C. Marr and X. Li, "Composition and performance modelling of catalyst layer in a proton exchange membrane fuel cell," *Journal of Power Sources*, vol. 77, pp. 17-27, 1999.

[48] W. Sun, B. A. Peppley, and K. Karan, "An improved two-dimensional agglomerate cathode model to study the influence of catalyst layer structural parameters," *Electrochimica Acta*, vol. IN PRESS, 2005.

[49] R. E. De La Rue and C. W. Tobias, "On the Conductivity of Dispersions," *Journal of the Electrochemical Society*, vol. 106, pp. 827-833, 1959.

[50] H. Ju and C. Y. Wang, "Experimental validation of a PEM fuel cell model by current distribution data," *Journal of the Electrochemical Society*, vol. 151, pp. A1954-A1960, 2004.

[51] G. Sasikumar, J. W. Ihm, and H. Ryu, "Optimum Nafion content in PEM fuel cell electrodes," *Electrochimica Acta*, vol. 50, pp. 598-602, 2004.

[52] P. D. Beattie, V. I. Basura, and S. Holdcroft, "Temperature and pressure dependence of O2 reduction at Pt | Nafion 117 and Pt | BAM 407 interfaces," *Journal of Electroanalytical Chemistry*, vol. 468, pp. 180-192, 1999.

[53] L. Zhang, C. Ma, and S. Mukerjee, "Oxygen reduction and transport characteristics at a platinum and alternative proton conducting membrane interface," *Journal of Electroanalytical Chemistry*, vol. 568, pp. 273-291, 2004.

[54] A. A. Kornyshev and A. A. Kulikovsky, "Characteristic length of fuel and oxygen consumption in feed channels of polymer electrolyte fuel cells," *Electrochimica Acta*, vol. 46, pp. 4389-4395, 2001.

[55] T. Navessin, S. Holdcroft, Q. Wang, D. Song, Z. Liu, M. Eikerling, J. Horsfall, and K. Lovell, "The role of membrane ion exchange capacity on membrane|gas diffusion electrode interfaces: a half-fuel cell electrochemical study," *Journal of Electroanalytical Chemistry*, vol. 567, pp. 111-122, 2004.

[56] Y. Sone, P. Ekdunge, and D. Simonsson, "Proton conductivity of Nafion 117 as measured by a four-electrode AC impedance method," *Journal of the Electrochemical Society*, vol. 143, pp. 1254-1259, 1996.

[57] E. L. Cussler, *DIFFUSION-Mass Transfer in Fluid Systems*. New York: Cambridge University Press, 1997.

[58] G. J. M. Janssen and M. L. J. Overvelde, "Water transport in the proton-exchange-membrane fuel cell: Measurements of the effective drag coefficient," *Journal of Power Sources*, vol. 101, pp. 117-125, 2001.

[59] J. Fimrite, B. Carnes, H. Struchtrup, and N. Djilali, "Transport phenomena in polymer electrolyte membranes. Part II: Binary friction membrane model," *Journal of the Electrochemical Society, IN PRESS*, 2005.

[60] T. Thampan, S. Malhotra, H. Tang, and R. Datta, "Modeling of Conductive Transport in Proton-Exchange Membranes for Fuel Cells," *Journal of the Electrochemical Society*, vol. 147, pp. 3242-3250, 2000.

[61] S. Slade, S. A. Campbell, T. R. Ralph, and F. C. Walsh, "Ionic conductivity of an extruded 1100 EW series of membranes," *Journal of the Electrochemical Society*, vol. 149, pp. A1556-A1564, 2002.

[62] F. N. Büchi and G. G. Scherer, "Investigation of the Transversal Water Profile in Nafion Membranes in Polymer Electrolyte Fuel Cells," *Journal of the Electrochemical Society*, vol. 148, pp. A183-A188, 2001.

[63] I. Martorell, J. Herrero, and F. X. Grau, "Natural convection from narrow horizontal plates at moderate Rayleigh numbers," *International Journal of Heat and Mass Transfer*, vol. 46, pp. 2389-2402, 2003.

[64] M. F. Mathias, J. Roth, J. Flemming, and W. Lehnert, "Diffusion media materials and characterization," in *Handbook of Fuel Cells*, vol. 3, W. Vielstich, A. Lamm, and H. A. Gasteiger, Eds., 2003, pp. 517-537.

[65] M. W. Chase, *JANAF Thermochemical Tables*, vol. 1-2, 3rd ed: Amer. Chem. Soc. and NIST, 1986.

[66] J. F. Moxley, S. Tulyani, and J. B. Benziger, "Steady-state multiplicity in the autohumidification polymer electrolyte membrane fuel cell," *Chemical Engineering Science*, vol. 58, pp. 4705-4708, 2003.

[67] U. Pasaogullari and C. Y. Wang, "Two-Phase Modeling and Flooding Prediction of Polymer Electrolyte Fuel Cells," *Journal of the Electrochemical Society*, vol. 152, pp. A380-A390, 2005.

[68] N. V. Suryanarayana, *Engineering Heat Transfer*: West Publishing Company, 1995.

[69] D. R. Sena, E. A. Ticianelli, V. A. Paganin, and E. R. Gonzalez, "Effect of water transport in a PEFC at low temperatures operating with dry hydrogen," *Journal of Electroanalytical Chemistry*, vol. 477, pp. 164-170, 1999.

[70] M. V. Williams, H. R. Kunz, and J. M. Fenton, "Operation of Nafion®-based PEM fuel cells with no external humidification: influence of operating conditions and gas diffusion layers," *Journal of Power Sources*, vol. 135, pp. 122-134, 2004.

[71] F. N. Büchi and S. Srinivasan, "Operating proton exchange membrane fuel cells without external humidification of the reactant gases - Fundamental aspects," *Journal of the Electrochemical Society*, vol. 144, pp. 2767-2772, 1997.

[72] Z. G. Qi and A. Kaufman, "Low Pt loading high performance cathodes for PEM fuel cells," *Journal of Power Sources*, vol. 113, pp. 37-43, 2003.

[73] V. A. Paganin, E. A. Ticianelli, and E. R. Gonzalez, "Development and electrochemical studies of gas diffusion electrodes for polymer electrolyte fuel cells," *Journal of Applied Electrochemistry*, vol. 26, 1996.

[74] J. M. Song, S. Y. Cha, and W. M. Lee, "Optimal composition of polymer electrolyte fuel cell electrodes determined by the ac impedance method," *Journal of Power Sources*, vol. 94, pp. 78-84, 2001.

[75] M. M. Mench, C. Y. Wang, and M. Ishikawa, "In situ current distribution measurements in polymer electrolyte fuel cells," *Journal of the Electrochemical Society*, vol. 150, pp. A1052-A1059, 2003.

[76] A. A. Kulikovsky, A. Kucernak, and A. A. Kornyshev, "Feeding PEM fuel cells," *Electrochimica Acta*, vol. 50, pp. 1323-1333, 2005.

Appendix A

Derivation of the catalyst layer model

The problem considered is the distribution of the activation overpotential/electrolyte phase potential in the catalyst layer of a polymer electrolyte membrane fuel cell (PEMFC). The boundary conditions are:

1. At the catalyst layer/GDL interface ($x = 0$), there is zero ionic current.
2. At the catalyst layer/membrane interface ($x = W_{CL}$), the activation overpotential/electrolyte phase potential is fixed.

The derivation begins with Ohm's law:

$$i = \sigma \frac{d\phi}{dx} \tag{A.1}$$

where i is the protonic current, σ is the protonic conductivity of the catalyst layer, and ϕ is the electrolyte phase potential. Herein, the activation overpotential η is defined as:

$$\eta = \phi - \phi_s \tag{A.2}$$

where ϕ_s is the electric phase potential. Because the electric phase potential is considered constant, Eqn. (A.1) becomes:

$$i = \sigma \frac{d\eta}{dx} \tag{A.3}$$

The conservation of current in the catalyst layer is equal to the current source s_i:

$$\frac{di}{dx} = \sigma \frac{d}{dx}\left(\frac{d\eta}{dx}\right) = s_i \tag{A.4}$$

where, for sufficiently large overpotentials, the source is determined by the Tafel equation:

$$\sigma \frac{d}{dx}\left(\frac{d\eta}{dx}\right) = i_o \left(\frac{\bar{c}_{O2}}{c_{O2}^{ref}}\right)^{\gamma} \exp\left(\frac{\alpha F}{RT}\eta\right) \tag{A.5}$$

where i_o^{ref} is the exchange current density at a known reference state, $\bar{c}_{O2}$ is the mean oxygen concentration in the catalyst layer, c_{O2}^{ref} is the reference oxygen concentration, γ is the order of the reaction, α is the transfer coefficient, F is Faraday's constant, R is the universal gas constant, and T is the temperature.

The general form of the equation becomes:

$$\frac{d}{dx}\left(\frac{d\eta}{dx}\right) = A\exp(b\eta) \tag{A.6}$$

where:

$$A = \frac{i_o}{\sigma}\left(\frac{\bar{c}_{O2}}{c_{O2}^{ref}}\right)^{\gamma} \quad \& \quad b = \frac{\alpha F}{RT} \tag{A.7}$$

Multiplying both sides of Eqn. (A.6) by the derivative of the overpotential gives:

$$\frac{d\eta}{dx}d\left(\frac{d\eta}{dx}\right) = A\exp(b\eta)d\eta \tag{A.8}$$

Eqn. (A.8) is then integrated and arranged as:

$$\frac{d\eta}{dx} = \sqrt{\frac{2A}{b}\exp(b\eta) + 2C} \tag{A.9}$$

The zero current boundary condition at $x = 0$ provides the solution to the integration constant.

$$\frac{d\eta}{dx} = \sqrt{\frac{2A}{b}}\sqrt{\exp(b\eta) - \exp(b\eta_o)} \tag{A.10}$$

where η_o is the overpotential at catalyst layer/GDL interface. η_o is not known *a priori,* so this expression results in an implicit solution.

To solve for the overpotential, Eqn. (A.10) is rearranged and integrated:

$$\int \frac{d\eta}{\sqrt{\exp(b\eta)-\exp(b\eta_o)}} = \sqrt{\frac{2A}{b}}x + C \tag{A.11}$$

The solution of the left hand side is found in integration tables and is expressed as:

$$\int \frac{d\eta}{\sqrt{\exp(b\eta)-\exp(b\eta_o)}} = \frac{2}{b}\exp\left(\frac{-b\eta_o}{2}\right)\arctan\left(\frac{\sqrt{\exp(b\eta)-\exp(b\eta_o)}}{\sqrt{\exp(b\eta_o)}}\right) \tag{A.12}$$

Substituting Eqn. (A.12) into Eqn. (A.11) provides:

$$\sqrt{\frac{2A}{b}}x + C = \frac{2}{b}\exp\left(\frac{-b\eta_o}{2}\right)\arctan\left(\frac{\sqrt{\exp(b\eta)-\exp(b\eta_o)}}{\sqrt{\exp(b\eta_o)}}\right) \tag{A.13}$$

The integration constant is solved with the fixed overpotential boundary condition at the catalyst layer/membrane interface ($\eta = \eta_1$ at $x = W_{CL}$).

$$\sqrt{\frac{2A}{b}}(x - W_{CL}) + \frac{2}{b}\exp\left(\frac{-b\eta_o}{2}\right)\arctan\left(\frac{\sqrt{\exp(b\eta_1)-\exp(b\eta_o)}}{\sqrt{\exp(b\eta_o)}}\right) = \ldots$$
$$\frac{2}{b}\exp\left(\frac{-b\eta_o}{2}\right)\arctan\left(\frac{\sqrt{\exp(b\eta)-\exp(b\eta_o)}}{\sqrt{\exp(b\eta_o)}}\right) \tag{A.14}$$

Rearranging Eqn. (A.14) to solve for the overpotential distribution gives the expression:

$$\eta(x)=\frac{1}{b}\ln\left(\tan^2\left(\sqrt{\frac{bA\exp(b\eta_o)}{2}}(x-W_{CL})+\ldots \arctan\left(\frac{\sqrt{\exp(b\eta_1)-\exp(b\eta_o)}}{\sqrt{\exp(b\eta_o)}}\right)\right)+1\right)+\eta_o \quad \text{(A.15)}$$

Eqn. (A.15) is an implicit solution of $\eta(x)$ because it requires knowledge of η_o, which is not known *a priori*. Thus, Eqn. (A.15) can be solved iteratively.

The protonic current at any given location in the catalyst layer can be resolved from Eqn. (A.9) and the solution of Eqn. (A.15):

$$i(x)=\sigma\sqrt{\frac{2A}{b}}\sqrt{\exp\left(b\eta(x)\right)-\exp(b\eta_o)} \quad \text{(A.16)}$$

The total current density of the catalyst layer is the current density at the catalyst/membrane interface:

$$i=\sigma\sqrt{\frac{2A}{b}}\sqrt{\exp(b\eta_1)-\exp(b\eta_o)} \quad \text{(A.17)}$$

Appendix B

Derivation of the microstructured GDL model

The following appendix presents the derivation of the equation modeling gas diffusion within the microstructured fuel cell's gas diffusion layer (GDL). The boundary conditions include a fixed concentration at the top of the cell (z = H) and variable flux along the catalyst layer interface (x = 0). The mass flux ($\dot{N}$) along the depth of the cavity in the z direction, determined from Fick's law for gas diffusion, is expressed as:

$$\dot{N}_z = -W_{GDL}\rho D^{eff}\frac{dy^m}{dz} \tag{B.1}$$

where W_{GDL} is the width of the microstructured GDL, y^m is the mean mass fraction along the depth of the cavity, ρ is the density of the gas mixture, and D^{eff} is the

effective diffusivity. This flux can also be correlated to the local source/sink of a species along the depth of the cavity:

$$\dot{N}_z = -\frac{M}{nF}\int_0^z i(z)\,dz \tag{B.2}$$

where M is the molar mass of the species, n is the number of the electrons transferred per mole of the species consumed (positive) or produced (negative), and $i(z)$ is the local current density. When Eqns. (B.1) and (B.2) are equated, the following relationship is obtained:

$$dy^m = \frac{M}{nFW_{GDL}\rho D^{eff}}\int_0^z i(z)\,dzdz \tag{B.3}$$

After integrating the above equation once, the result is:

$$y^m = \frac{M}{nFW_{GDL}\rho D^{eff}}\int_0^z\int_0^z i(z)\,dzdz + C \tag{B.4}$$

The constant of integration is resolved with the boundary condition at the top of the cavity ($y^m = y^o$ at $z = H$):

$$C = y^o - \frac{M}{nFW_{GDL}\rho D^{eff}}\int_0^H\int_0^z i(z)\,dzdz \tag{B.5}$$

The resulting solution of y^m is then formulated as:

$$y^m = \frac{M}{nFW_{GDL}\rho D^{eff}}\left[\int_0^z\int_0^z i(z)\,dzdz - \int_0^H\int_0^z i(z)\,dzdz\right] + y^o \tag{B.6}$$

To account for the gradient of species concentration in the x-direction, an assumption is made regarding the location of the mean mass fraction y^m along the x-axis inside the cavity. The assumption employed is that the location of the mean mass fraction along the x-axis is $x = W_{GDL}/2$. The boundary conditions along the x-axis are:

$$\frac{dy}{dx} = 0 \text{ at } x = W_{GDL}$$

and

$$y = y^m \text{ at } x = W_{GDL}/2$$

Fick's law for the specific mass flux in the x-direction is expressed as:

$$\dot{n}_z = -\rho D^{eff} \frac{dy^m}{dx} \tag{B.7}$$

In addition, the following linear profile of specific mass flux in the x-direction is assumed:

$$\dot{n}_z = -\frac{M}{nFW_{GDL}} i(z)(W_{GDL} - x) \tag{B.8}$$

Equating Eqns. (B.7) and (B.8) produces the following expression:

$$dy = \frac{M}{nFW_{GDL}\rho D^{eff}} i(z)(W_{GDL} - x)dx \tag{B.9}$$

After integrating, the following expression is obtained:

$$y = \frac{M}{nFW_{GDL}\rho D^{eff}} i(z)\left(W_{GDL}x - \frac{x^2}{2} \right) + C \tag{B.10}$$

By employing the boundary condition $y = y^m$ at $x = W_{GDL}/2$, an expression for the integration constant is obtained:

$$C = y^m - \frac{3Mi(z)W_{GDL}^2}{8nFW_{GDL}\rho D^{eff}} \tag{B.11}$$

The resulting distribution of the mass fraction along the x-axis for a given location along the z-axis is expressed as:

$$y = \frac{M}{nFW_{GDL}\rho D^{eff}} i(z)\left(W_{GDL}x - \frac{x^2}{2} - \frac{3i(z)W_{GDL}^2}{8} \right) + y^m \tag{B.12}$$

A general two-dimensional solution of the mass fraction distribution is obtained by substituting the solution for the mean mass fraction along the z-axis into the above equation:

$$y(x,z) = \frac{M}{nFW_{GDL}\rho D^{eff}} \left[\begin{array}{l} \int_0^z \int_0^z i(z)\,dzdz - \int_0^H \int_0^z i(z)\,dzdz + \ldots \\ \qquad i(z)\left(W_{GDL}x - \frac{x^2}{2} - \frac{3W_{GDL}^2}{8} \right) \end{array} \right] + y^o \tag{B.13}$$